2010/2 vol.7

ACTA GEOTECHNICA SLOVENICA

2010/2

ISSN 1854-0171

ACTA GEOTECHNICA SLOVENICA

ISSN: 1854-0171

Revija redno izhaja dvakrat letno. Članki v reviji so recenzirani s strani priznanih mednarodnih strokovnjakov. Baze podatkov v katerih je revija indeksirana: SCIE - Science Citation Index Expanded, JCR – Journal Citation Reports / Science Edition, ICONDA - The international Construction database, GeoRef. Pri financiranju revije sodeluje Javna agencija za knjigo Republike Slovenije.

naslov uredništva **address**

ACTA GEOTECHNICA SLOVENICA
Univerza v Mariboru, Fakulteta za gradbeništvo
Smetanova ulica 17, 2000 Maribor, Slovenija
Telefon / Telephone: +386 (0)2 22 94 300
Faks / Fax: +386 (0)2 25 24 179
E-pošta / E-mail: ags@uni-mb.si

spletni naslov **web address**

http://www.fg.uni-mb.si/journal-ags/

The journal is published twice a year. Papers are peer reviewed by renowned international experts. Indexation data bases of the journal: SCIE - Science Citation Index Expanded, JCR – Journal Citation Reports / Science Edition, ICONDA - The international Construction database, GeoRef. Financially supported also by Slovenian Book Agency.

VSEBINA

CONTENTS

UVODNIK

Spoštovani bralci, z veseljem vam sporočamo, da smo prenovili spletno stran mednarodne revije Acta Geotechnica Slovenica in jo oblikovali v duhu novejših trendov in tehničnih rešitev - http://www.fg.uni-mb.si/journal-ags/.

Novosti so poleg novega izgleda:

- vsebina zadnje številke je prikazana takoj po izdaji že kar na prvi strani;
- po kliku na posamezen članek se odpre celoten povzetek z možnostjo prenosa članka v PDF formatu;
- dodan je seznam vseh avtorjev po abecednem redu, s povezavami na avtorjeve članke. Seznam je možno razvrščati po priimkih, imenih ali po številu prispevkov (v brskalniku Internet Explorer 6 in 7 to lahko to traja malo dlje - cca 10 sekund);
- vse spletne strani s PDF dokumenti so opremljene z meta podatki (avtorstvo, ključne besede, naslov ...), vendar bo preteklo še nekaj časa, preden bo Google indeksiral te dokumente.

V pričujoči številki revije je objavljenih pet prispevkov:

Avtorji prvega prispevka Noureddine Della, Ahmed Arab, Mostefa Belkhatir, Hanifi Missoum, Claude Bacconnet in Daniel Boissier podajajo ugotovitve, kako začetna struktura meljnih peskov vpliva na rezultate nedreniranih triosnih tlačnih preizkusov v laboratoriju. Ugotovljeno je bilo, da ima začetna struktura tal bistveni vpliv na nedrenirani strižni odziv izražen z maksimalno deviatorično napetostjo, vrhnjo trdnostjo in prirastkom pritiska porne vode.

V članku avtorjev Qun Chen, Li Wan, Changrong He in Zihui Lai je podana študija bočnih zemeljskih pritiskov na steno zidu, razporeditev napetosti ter sil v armaturi grede in pilotov, ki uporablja rezultate terenskih opazovanj in tridimenzionalnih analiz na osnovi končnih elementov. Rezultati simulacij se dobro ujemajo z rezultati terenskih meritev.

Avtorja Izidor Tasič in Franc Runovc v prispevku obravnavata postopek preverjanja zanesljivosti instrumentov za beleženje horizontalno-vertikalnega spektralnega razmerja mikrotremorjev. Razvit je bil postopek, pri katerem se s pomočjo dveh referenčnih seizmoloških sistemov preveri vpliv prenosih funkcij testiranega sistema na krivuljo spektralnega razmerja mikrotremorjev, ne da bi vnaprej poznali prenosne funkcije kateregakoli od sistemov. Postopek je prikazan na seizmometru Lennartz LE-3D/5s in na seizmoloških sistemih TROMINO, kjer sta bila za referenčna seizmometra uporabljena širokopasovna seizmometra STS-2.

Avtroja Borut Macuh in Stanislav Škrabl obravnavata teorem korespondenčnih stanj (Caquot 1934), ki velja le za enostavnejše primere mejnih stanj, kjer so napetostni vektorji pravokotni na robne površine ter kadar se pri transformaciji ohranjajo smeri trajektorij glavnih napetosti (Michalowski 2001). Rezultati opravljenih analiz pasivnih zemeljskih pritiskov kažejo, da je v splošnejših primerih nekritična uporaba teorema korespondenčnih stanj v osnovni obliki nedopustna, ker so dobljeni rezultati lahko pravilni le naključno, odvisno od robnih pogojev.

Članek Tomaža Pliberška in Andreja Umeka obravnava razvoj aproksimativnih funkcij za določevanje pomikov v tolerancah inženirske natančnosti na osnovi eksaktno diskretiziranih komponent Greenove funkcije. Njihova natančnost bi naj bila boljša kot so tolerance intruzivnih merskih podatkov identifikacije mehanskih karakteristik zemljine. Uporaba v članku izpeljanih aproksimativnih izrazov bo zmanjšala matematični napor pri reševanju interakcijskih problemov konstrukcija - zemljina, istočasno pa odprla nove možnosti za neintruzivne identifikacije zemljin.

Ludvik Trauner
Glavni urednik

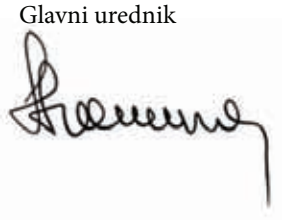

EDITORIAL

Dear Readers

We are pleased to announce that the Acta Geotechnica Slovenica web pages have been renewed and redesigned with a more modern style and with easier navigation: http://www.fg.uni-mb.si/journal-ags/.

As well as the new design, there are some other important innovations:

- The contents of the most recent issue are displayed on the first page.
- After clicking on a certain article the whole abstract opens and it is then possible to download the full article in PDF format.
- An alphabetic list of all the authors is added, and there is a link to an author's articles. You can arrange the list according to surnames, first names or the number of articles (it can take about 10 seconds when using Internet Explorer 6 and 7).
- All the web pages contain metadata (authors, key words, titles, etc.), but it will take some time for Google to index these documents.

There are five articles published in this issue:

The authors of the first contribution – Noureddine Della, Ahmed Arab, Mostefa Belkhatir, Hanifi Missoum, Claude Bacconnet and Daniel Boissier – present their findings about the influence of the initial structure of silty sands on the results of undrained triaxial compression tests in the lab. They established that the initial structure of the soil has a considerable influence on the undrained shear response in terms of the maximal deviatoric stress, the peak strength and the excess pore-water pressure.

In the article by Qun Chen, Li Wan, Changrong He and Zihui Lai a study of the lateral earth pressure on the wall back, the stress distributions and the forces of the reinforcements in the beam and the pile was carried out. The simulation results are in good agreement with the field observation data.

The paper by Izidor Tasič and Franc Runovc studies the procedures for testing the reliability of instruments used in microtremor horizontal-to-vertical spectral ratio measurements. With the help of a two-reference system the influence of the transfer function on the HVSR curve can be evaluated without any a-priori knowledge of the transfer functions of any of the systems. Furthermore, this approach is applied to a Lennartz Le-3D/5s seismometer and to a TROMINO seismological system, where two Streckeisen STS2 seismometers are used as the reference systems.

The authors Borut Macuh and Stanislav Škrabl deal with the corresponding state theorem (Caquot, 1934), which is limited and valid only for simpler limit states, where the stress vectors are perpendicular to the boundary surfaces and when the directions of the stress eigenvalue trajectories in the transformation are preserved (Michalowski, 2001). However, the results of their analyses show that an incautious application of the corresponding state theorem in its basic form and for general cases is inadmissible because the results obtained can be correct only coincidentally, depending on the boundary conditions.

The article of Tomaž Pliberšek and Andrej Umek describes the development of approximate expressions for a displacement determination within the tolerances of engineering accuracy based on exactly discretized components of a Green's function. Their accuracy should be better than the tolerances in the intrusive measurements data for the identification of the mechanical characteristics of soils. Therefore, the application of these approximate expressions is believed to reduce the computational effort in soil-structure interaction problems considerably and open up new possibilities for the nonintrusive identification of soils.

Ludvik Trauner
Editor–in–chief

VPLIV ZAČETNE STRUKTURE NA LASTNOSTI PESKA CHLEF

NOUREDDINE DELLA, AHMED ARAB, MOSTEFA BELKHATIR, HANIFI MISSOUM, CLAUDE BACCONNET IN DANIEL BOISSIER

o avtorjih

Noureddine Della *
Université de Chlef,
Département de Génie Civil,
Route de sendjas BP 151,
Chlef 02000, Alžirija
E-pošta: nour_della@yahoo.fr

Ahmed Arab
Université de Chlef,
Département de Génie Civil,
Route de sendjas BP 151,
Chlef 02000, Alžirija
E-pošta: ah_arab@yahoo.fr

Mostefa Belkhatir
Université de Chlef,
Département de Génie Civil,
Route de sendjas BP 151,
Chlef 02000, Alžirija
E-pošta: abelkhatir@yahoo.com

Hanifi Missoum
Université de Mostaganem,
Département de Génie Civil
Site 1,route de Belahcel BP 300,
Mostaganem 27000, Alžirija
E-pošta: hanifimissoum@yahoo.fr

Claude Bacconnet
Polytech'Clermont,
Ecole d'ingénieurs (CUST),
BP 206-63174 Aubière Cedex, Francija
E-pošta: claude.bacconnet@polytech.univ-bpclermont.fr

Daniel Boissier
Polytech'Clermont,
Ecole d'ingénieurs (CUST)
BP 206-63174 Aubière Cedex, Francija
E-pošta: daniel.boissier@polytech.univ-bpclermont.fr

* vodilni avtor

izvleček

Že vrsto let je znano, da začetna struktura igra pomembno vlogo pri rezultatih laboratorijskega preskušanja naravnih meljnih peskov. V ta namen se je izvedla vrsta nedreniranih triosnih tlačni preskusov na vzorcih, sestavljenih iz peska Chlef z 0,5% vsebnostjo neplastičnega melja z uporabo dveh sedimentacijskih metod in pri različnih začetnih relativnih gostotah (Dr = 29%, 50% in 80%). Vsi vzorci so bili izotropno konsolidirani pri 50 kPa, 100 kPa in 200 kPa. Ugotovljeno je bilo, da ima začetna struktura tal bistveni vpliv na nedrenirani strižni odziv izražen z maksimalno deviatorično napetostjo, vrhnjo trdnostjo in prirastkom pritiska porne vode.

ključne besede

utekočinjenje, pesek, suho odlaganje, mokro odlaganje, gostota, deviatorična napetost, porni tlak

EFFECT OF THE INITIAL STRUCTURE ON THE BEHAVIOR OF CHLEF SAND

NOUREDDINE DELLA, AHMED ARAB, MOSTEFA BELKHATIR, HANIFI MISSOUM, CLAUDE BACCONNET and DANIEL BOISSIER

About the authors

Noureddine Della *
Université de Chlef,
Département de Génie Civil,
Route de sendjas BP 151, Chlef 02000, Algeria
E-mail: nour_della@yahoo.fr

Ahmed Arab
Université de Chlef,
Département de Génie Civil,
Route de sendjas BP 151, Chlef 02000, Algeria
E-mail: ah_arab@yahoo.fri

Mostefa Belkhatir
Université de Chlef,
Département de Génie Civil,
Route de sendjas BP 151, Chlef 02000, Algeria
E-mail: abelkhatir@yahoo.com

Hanifi Missoum
Université de Mostaganem,
Département de Génie Civil
Site 1,route de Belahcel BP 300, Mostaganem 27000, Algeria
E-mail: hanifimissoum@yahoo.fr

Claude Bacconnet
Polytech'Clermont,
Ecole d'ingénieurs (CUST),
BP 206-63174 Aubière Cedex, France
E-mail: claude.bacconnet@polytech.univ-bpclermont.fr

Daniel Boissier
Polytech'Clermont,
Ecole d'ingénieurs (CUST)
BP 206-63174 Aubière Cedex, France
E-mail: daniel.boissier@polytech.univ-bpclermont.fr

* Corresponding author

Abstract

It has been known for many years that initial structure, plays an important part in the results of laboratory testing of natural of silty sands. For this purpose, a series of monotonic undrained triaxial compression tests were carried out on samples composed of Chlef sand with 0.5% non-plastic silt content using two depositional methods (dry funnel pluviation and wet deposition) at different initial relative density (RD= 29%, 50% and 80%). All specimens were subjected to isotropic consolidation of 50 kPa, 100 kPa and 200 kPa. It was found that the initial structure of the soil influences considerably the undrained shear response in terms of maximal deviatoric stress, peak strength and excess pore water pressure.

Keywords

liquefaction, sand, dry funnel pluviation, wet deposition, density, deviatoric stress, pore pressure

1 INTRODUCTION

It is widely recognized that the mechanical behavior of sands very much depends on their initial state in terms of the void ratio (or relative density) and the effective stresses. Polito and Martin [10] asserted that the relative density and skeleton void ratio were factors that seemed to explain the variation in the different experimental results. Many studies concluded that complete static liquefaction (zero effective confining pressure and zero effective stress difference) in laboratory testing is most easily achieved in silty sands at very low pressures (Yamamuro and Lade [14]; Yamamuro and Lade [15]; Yamamuro and Covert [13]). Kramer and Seed [6] also observed that the liquefaction resistance increased with an increasing confining pressure.

Numerous studies have reported that the behavior of sands can be greatly influenced by specimen reconstitution. The effect of the preparation method used for the samples has been subject to many controversial researches, and several studies have reported that the resistance to liquefaction is more elevated for samples prepared by the method of sedimentation than for samples prepared by other methods, such as dry funnel

pluviation and wet deposition (Zlatovic and Ishihara [18]); other studies have found that the specimens reconstituted by the wet deposition method are more resistant than those prepared by the dry funnel pluviation method (Mulilis et al. [9]; Yamamuro and Wood [16]). Other researchers indicated that the tests prepared by dry funnel pluviation are more resistant than those prepared by wet deposition (Benahmed et al. [1]; Canou, [3]). Vaid et al. [11] confirmed this result while showing that wet deposition encourages the initiation of the liquefaction in relation to a setting up by pluviation under water. Yamamuro et al. [17] concluded, after their laboratory investigation, that the method of dry pluviation supports the instability of the samples, in contrast to the method of sedimentation. Wood et al. [12] found that the effect of the method of deposition on the undrained behavior decreases when the density increases. They also found that this influence decreases with the increase of the fines content, particularly with the lower densities. Indeed, two sets of undrained triaxial tests were carried out, using two methods of deposition, such as dry funnel pluviation and wet deposition, in order to define the effect of the method of preparation of the samples on the resistance to liquefaction. Since there were different possible modes of formation for the natural sandy solid masses, the use of the two modes of deposition for the Chlef sand allows us to approach to the reality of the area, the final purpose being the characterization of the behavior of this sand to liquefaction. According to Durville and Méneroud [4] the phenomenon of liquefaction appeared during the last earthquake (10 October 1980) on a vast alluvial valley crossed by the Chlef river and the zone of confluence of this river with the Fodda river, as shown in Fig. 1.

Figure 1. Sand boils due to the liquefaction phenomenon.

2 MATERIAL TESTED

All the tests in the present study were performed on the sand of Chlef (Algeria) containing 0.5% of silt of the river of Chlef that crosses the city of Chlef to the west of Algiers. The granulometric curve of this sand is given in Fig. 2. The sand of Chlef is a medium sand, rounded with a medium diameter D_{50}=0.45mm. The contained silt is non-plastic with a plasticity index of 5.81%. Table 1 gives the physical properties of the used sand. The tests were carried out on specimens collected from the region where the phenomenon of liquefaction was observed during the last earthquake (10 October 1980) near the Chlef river (see Fig. 1) for three relative densities RD =29%, 50% and 80%, respectively, representing the loose, medium dense and dense states, for three initial confining pressures of 50, 100 and 200 kPa.

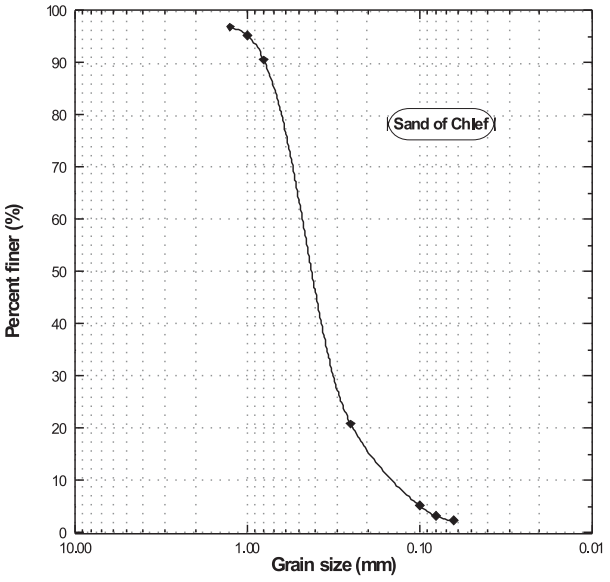

Figure 2. Grain size of the sand.

Table 1. Properties of soil.

Material	e_{min}	e_{max}	γ_{dmin} g/cm^3	γ_{dmax} g/cm^3	γ_s g/cm^3	Cu D_{60}/D_{10}	D_{50} mm	D_{10} mm	Grains shape
O/Chlef	0.54	0.99	1.34	1.73	2.67	3.2	0.45	0.15	Rounded

3 EXPERIMENTAL PROCEDURES

The experimental device is presented in Fig. 3. It contains:

- an autonomous triaxial cell of the Bishop and Wesley type (Bishop and Wesley, 1975),
- three controllers of the pressure/volume type GDS (200cc),
- a void pump joined to a reservoir in order to deaerate the demineralized water,
- a microcomputer equipped with software permitting the piloting of the test and the data acquisition.

3.1 SAMPLE PREPARATION

The samples were prepared with the help of a mold consisting of two semi-cylindrical shells. The two shells can be easily joined or embossed, one from the other, with the help of a hose clamp. In order to maintain the cuff made of latex along the partitions of the mold, four ducts of aspiration were pierced in the conducted shells. Cylindrical soil specimens of 70 mm × 70 mm (H/D= 1.0) (Yamamuro and Wood [16]; Lanier [8]; Hettler and Vardoulakis [5]; Bouvard and Stutz [2]) were created. The mass of sand to be put in place is evaluated according to the required density (the initial volume of the sample is known), the state of density of the sample being defined by the relative density:

$$I_D = (e_{max} - e) / (e_{max} - e_{min}) \qquad (1)$$

3.2 DEPOSITIONAL TECHNIQUES

Two methods were used to reconstitute the specimens of sand: wet deposition and dry funnel pluviation. The first method consists of mixing, in the most homogeneous manner possible, the sand previously dried with a small quantity of water fixed at 3% and the deposition of the humid soil in the mold with the control of the content in the water. The soil is finely placed in successive layers. A constant number of strokes were applied to get a homogeneous and isotropic structure. This method is more convenient for the sand, because it can provide some samples with a large range of void ratios. In the dry

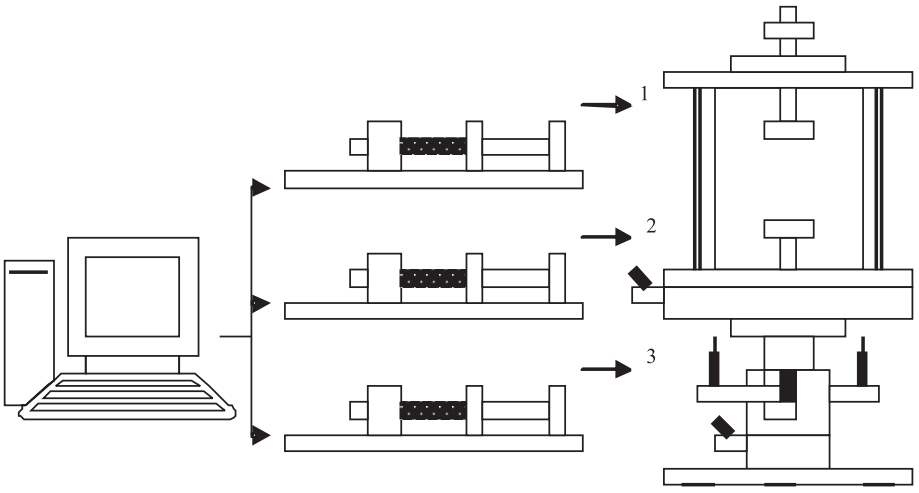

(1) application of the pressure in the cell
(2) control of the interstitial pressure or variation of volume of the sample
(3) control of the deviator

Figure 3. Experimental device used.

funnel pluviation method, the dry soil is deposited in the mold with the help of a funnel for control of the height. This method consists of filling the mold by tipping in rain of the dry sand. In order to have loose samples, it is necessary that the height of fall is quasi-nil.

3.3 SATURATION AND CONSOLIDATION OF THE SAMPLE

The saturation is an important stage in the experimental procedure because the response of the sample under undrained loading depends on its quality. To get a good degree of saturation, the technique of carbon dioxide elaborated by Lade and Duncan [7] was used. This technique consists of making the carbon dioxide circulate through the circuits of drainage and the sample to weak debit during a certain time, in order to occupy all the voids and to chase the air contained in the sample. Then, we make the deaerated and demineralized water circulate to chase the interstitial gas and to occupy its place. In spite of the passage of water, some voids remain occupied by the carbon dioxide. As the solubility of the gas is raised, water can dissolve what remains of the carbon dioxide after its passage, it generally permits us to ensure a good saturation of the sample. In order to consolidate the sample, we apply in the same way, an increase in pressure in the cell (GDS n1) and inside the sample (GDS n2). The application of a back pressure, with the help of the GDS n2, improves the quality of the saturation, while compressing the micro-bubbles of the interstitial gas that can still be present after the phase of saturation. These two pressures (in the cell and inside the sample) were maintained during a whole night to ensure good consolidation.

The quality of the saturation is evaluated with a measure of the coefficient of Skempton (B), according to a classic process: an increment $\Delta\sigma$ of the confining pressure of 100 kPa in an undrained condition was given, the response of the interstitial pressure Δu was measured and the degree of saturation by the formula $B=\Delta u / \Delta\sigma$ was evaluated.

4 RESULTS OF THE TESTS CONDUCTED

4.1 EFFECT OF CONFINING PRESSURE

The effect of the variation of the effective confining pressure on the liquefaction resistance of the sand is shown in Figs. 4 and 5. As the confining pressure is increased, the liquefaction resistance of the sands increased for both the dry funnel pluviation and wet deposition methods. The results in Figs. 4a and 4b with an initial density of 29% (loose state) for specimens reconstituted by the first method at a confining pressure of 50 kPa show a weaker resistance than those shown at confining pressures of 100 kPa and 200 kPa. Its resistance increases at the beginning of the loading up to a value of 20 kPa, corresponding to an axial strain of 0.5%, then it decreases up to an axial distortion strain of 5% to stabilize passing nearly a quasi steady state (QSS); then the sample mobilizes a residual strength, increasing the resistance of the sample in the steady state. The stress path diagram presents a reduction of the effective mean stress until a value of 20 kPa, then a migration toward higher values characterizing a dilating state. The same trends are signalled for the samples at confining pressures of 100 and 200 kPa, with peak deviatoric stresses of 40 kPa and 80 kPa, respectively.

The results of the Figs. 4c, 4d, 4e and 4f, for medium and dense samples, show a more resistant behavior of the sand. A change in the confining pressure from 50 to 200 kPa caused a variation in the peak deviatoric stress from 25 kPa to 115 kPa, associated with a higher residual strength at steady state.

The effective stress paths for undrained triaxial compression tests on Chlef sand for samples prepared by the wet deposition method with initial relative densities of 29%, 50% and 80% are plotted on the p'-q diagrams shown in Figs. 5b, 5d and 5f. As can be seen, complete static liquefaction occurred in the three tests with the lowest confining pressure (50 kPa). Static liquefaction coincided with the formation of large wrinkles in the membranes surrounding the specimens.

Figs. 5b, 5d and 5f also show that when the initial confining pressure is increased beyond 50 kPa, the effective stress paths exhibit behavior that is characterized by increasing stability or increasing resistance to liquefaction. This is demonstrated by examining the stress-strain curves in Figs. 5a, 5c and 5e. The initial confining pressures and densities are shown for each test. The stress-strain curves of the 100 and 200 kPa initial confining pressure tests show that the stress difference does not reach zero, as in the tests indicating complete liquefaction, but decreases to a minimum before increasing to levels well above the initial peak (medium and dense states) or with progressive stabilization around an ultimate stationary value very weak (loose state). This is the condition of temporary liquefaction. The effect of increasing the confining pressure is to increase the dilatant tendencies in the soil.

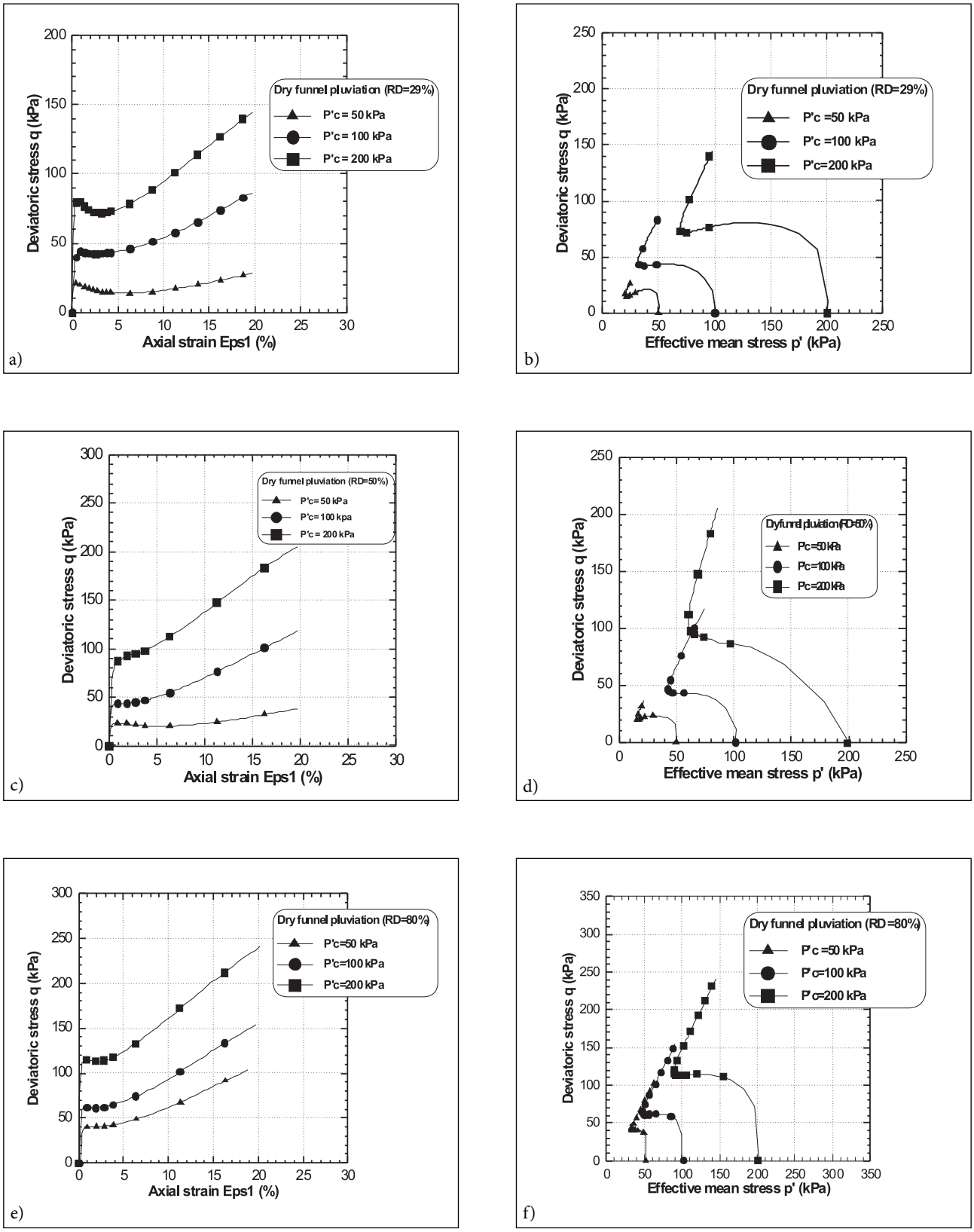

Figure 4. Undrained tests for samples prepared by the dry funnel pluviation method:
(a, c, e) deviatoric stress-strain curve, (b, d, f) stress path.

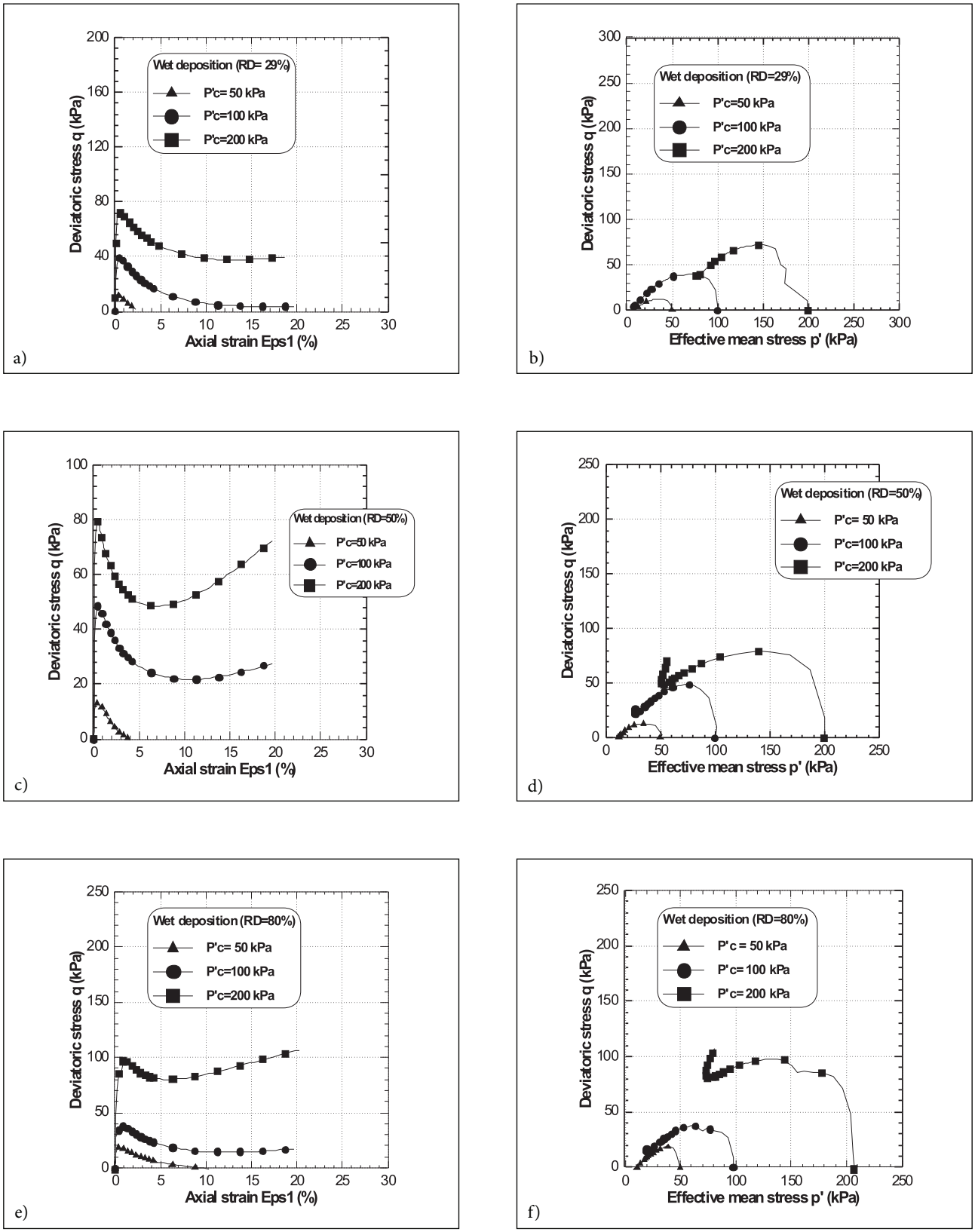

Figure 5. Undrained tests for samples prepared by the wet deposition method:
(a, c, e) deviatoric stress-strain curve, (b, d, f) stress path.

4.2 EFFECT OF INITIAL DENSITY

The effect of increasing the relative density was investigated by performing undrained tests on Chlef sand with initial relative densities of 29, 50 and 80%. The results of these tests are plotted in the p'-q_{max} diagrams shown in Figs. 6a and 6b. We note that the resistance to the liquefaction represented by the maximum deviatoric stress (q_{max}), increases with the density of the soil for both the dry funnel pluviation and wet deposition methods, with a more pronounced increase for the dry funnel pluviation method (Fig. 6a), where the values of the maximum deviator pass from 28.23 kPa for a loose soil and a confining pressure of 50 kPa, to 240.97 kPa for a dense soil and a confining pressure of 200 kPa. This shows that the effect of increasing the relative density is to increase the resistance of the soil to liquefaction by making the soil more dilatant. Fig. 6b shows that static liquefaction still occurred for the specimens reconstituted by the wet deposition method for the three densities at the 50 kPa confining pressure. Fig. 6b also indicates that the evolution of the resistance is less pronounced.

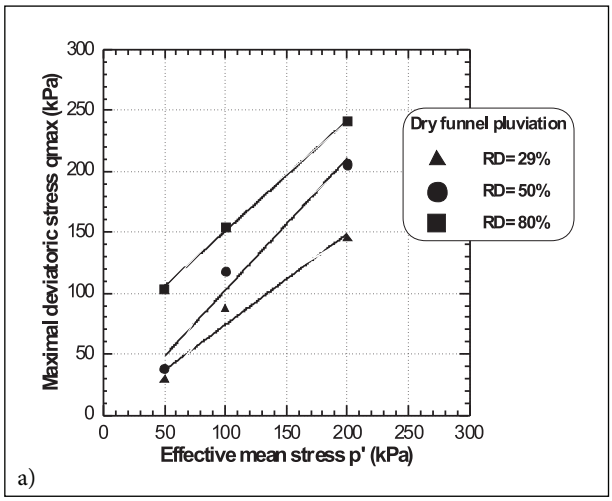

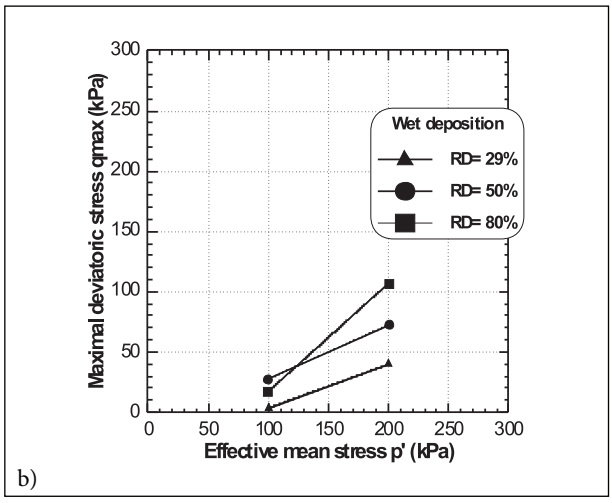

Figure 6. Effect of the relative density on the undrained response of sand: (a) dry funnel pluviation method, (b) wet deposition method.

4.3 INFLUENCE OF SAMPLE RECONSTITUTION METHOD

The effect of the specimens' reconstitution method on the maximum deviatoric stress is shown in Figs. 7a, 7b and 7c. It is clear from the results in these figures that the dry funnel pluviation method (DP) gives more significant values for the maximum deviator; therefore, a much higher resistance to liquefaction, contrary to the wet deposition method (WD) where some weaker values of the maximal deviator for low or medium densities (RD=29% and RD=50%) were noted, with progressive stabilization around a very weak or nil ultimate stationary value meaning the liquefaction of the sample.

The same tendencies are noted for the variations of the values in the peak deviatoric stress given in Figs. 7d, 7e and 7f. It is clear that the samples conceived by the dry funnel pluviation method exhibit a resistance to the monotonic shearing, superior (q_{pic}=240.97 kPa to the dense state and to confining pressure of 200 kPa) to those made by the wet deposition method (q_{pic}=106.73 kPa to the dense state and to a confining pressure of 200 kPa).

The influence of the sample preparation methods on the excess pore pressure is illustrated in Fig. 8. As shown by Figs. 8a, 8b and 8c for the dry funnel pluviation method, the variation of the pore-pressure curves represents two phases: the first shows a very high initial rate of generation, giving an account of the strongly contracting character of the Chlef sand. In the second phase, this rate decreases progressively with the axial strain, indicating the dilating character of the material. The developed excess pore pressure in the samples prepared by the wet deposition method is presented in Figs. 8d, 8e and 8f. It can be seen that the samples exhibit a very high contracting character, with an expansion rate very much elevated from the beginning of the shearing and progressive stabilization towards an ultimate value, to associate with the stabilization of the deviatoric stress.

The results in Figs. 7 and 8 are in perfect concordance with those of Figs. 4 and 5, knowing that the method

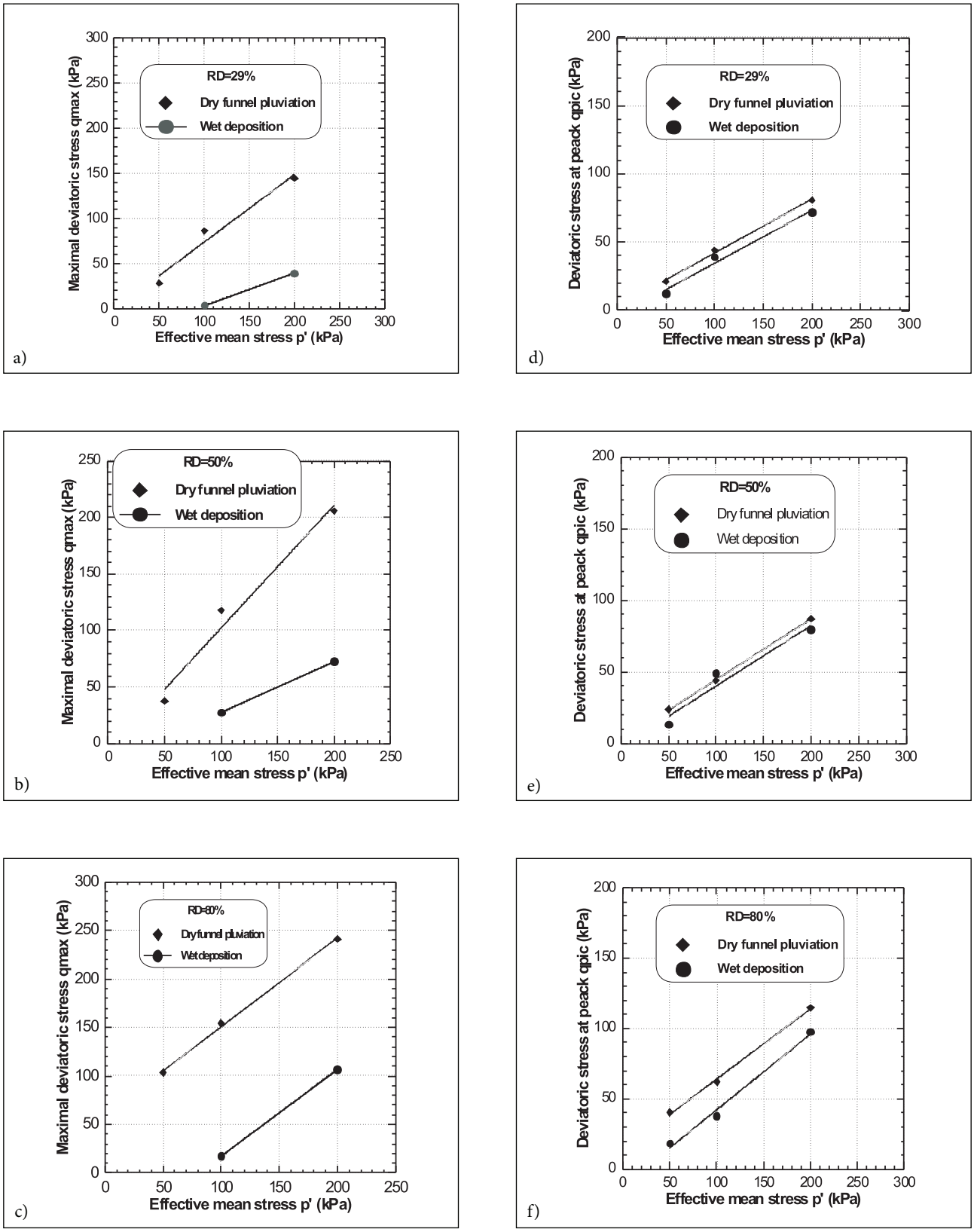

Figure 7. Effect of the depositional method on the maximum deviatoric stress (a, b, c) and the peak deviatoric stress (d, e, f).

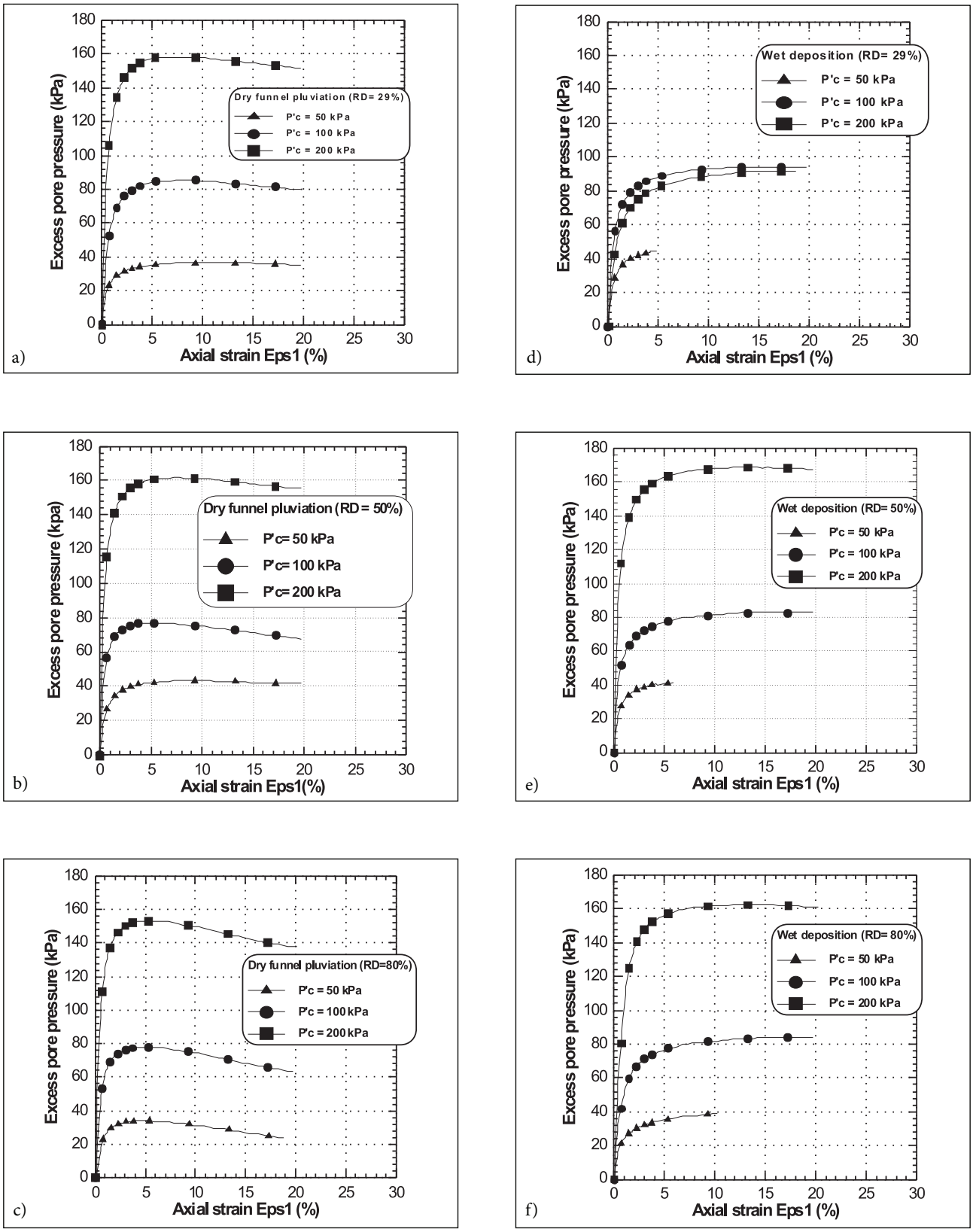

Figure 8. Effect of sample reconstitution methods on the excess pore pressure.

of dry funnel pluviation encourages an increase of the resistance to the monotonic shearing of the samples, in contrast to the wet deposition method, which accelerates the instability of the samples that show a very weak resistance and even provokes the phenomenon of liquefaction of the sand for the weak densities and weak confinements leading to a collapse of the sample. These differences of behavior noted on Chlef sand can be explained by the fact that the molecules of water contained in the structures prepared by the wet deposition method constitute some macropores that are easily compressible at the time of the shearing of the sample and at the same time prevent the grain-grain adhesion from which the faculty of the sample is to contract, in contrast to the structures of the samples prepared by the method of dry funnel pluviation that show a more dilating behavior.

5 CONCLUSION

The effect of the initial structure of a soil was studied in the laboratory. A series of monotonic triaxial tests were performed on chlef silty sand at a range of three relatives densities 29%, 50% and 80% representing loose, medium and dense state, for confining pressure of 50 kPa, 100 kPa and 200 kPa. In the light of evidence, the following conclusion can be drawn:

1. The excess pore water pressure increases for both the two depositional methods (dry funnel pluviation and wet deposition) with a decrease tendency for the first one and a stabilization for the second one.

2. The maximal deviatoric stress and the peak strength increase with the increase of the initial relative density and the initial confining pressure.

3. The initial structure made by the dry funnel pluviation method exhibits dilatant character inducing an important liquefaction resistance of the soil.

REFERENCES

[1] Benahmed, N., Canou, J. and Dupla, J. C. (2004). Structure initiale et propriétés de liquéfaction statique d'un sable. Comptes Rendus Mécanique 332, 887-894.

[2] Bouvard, D. and Stutz, P. (1984). Détermination expérimentale des caractéristiques rhéologiques d'un sable en grandes deformations. CRAS, 299, II, 12.

[3] Canou, J. (1989). Contribution l'étude et à l'évaluation des propriétés de liquéfaction d'un sable. Thèse de Doctorat de l'Ecole Nationale Des Ponts et Chaussées, Paris.

[4] Durville, J. L. and Méneroud, J. P. (1982). Phénomènes géomorphologiques induits par le séisme d'El-Asnam, Algérie. Bull. Liaison Labo. P. et Ch., 120, juillet-août, 13-23.

[5] Hettler, A. and Vardoulakis, I. (1983). Behavior of dry sand tested in large triaxial apparatus. Geotechnique 33.

[6] Kramer, S.L. and Seed, H.B. (1988). Initiation of soil liquefaction under static loading conditions. J. Geotech. Eng 114, 4, 412-430.

[7] Lade, P. V. and Duncan, J. M. (1973). Cubical triaxial tests on cohesionless soil. Journal Soil Mechanics and Foundations Division ASCE 99, SM10, 793-812.

[8] Lanier, J. (1987). Développements récents des essais en laboratoire. Manuel de Rhéologie des Géomatériaux, Presses des Ponts et Chaussées, 15-31.

[9] Mulilis, J. P., Seed, H. B., Chan, C. K., Mitchell, J. K. and Arulanadan, K. (1977). Effects of sample preparation on sand liquefaction. Journal of Geotechnical Engineering Division, ASCE 103, GT2, 91-108.

[10] Polito, C.P. and Martin II J.R. (2003). A reconciliation of the effects of non-plastic fines on the liquefaction resistance of sands reported in the literature. Earthquake Spectra 19, 3, 635-651.

[11] Vaid, Y. P., Sivathayalan, S. and Stedman, D. (1999). Influence of specimen reconstituting method on the undrained response of sand. Geotechnical Testing Journal 22, 3, 187-195.

[12] Wood, F. M., Yamamuro, J. A. and Lade, P. V. (2008). Effect of depositional method on the undrained response of silty sand. Canadian Geotechnical Journal 45, 11, 1525–1537.

[13] Yamamuro, J.A. and Covert, K.M. (2001). Monotonic and cyclic liquefaction of very loose sands with high silt content. J. Geotech. Geoenvironmental Engineering ASCE 127, 4, 314-324.

[14] Yamamuro, J.A. and Lade, P.V. (1997). Static liquefaction of very loose sands. Canadian Geotechnical J. 34, 6, 905-917.

[15] Yamamuro, J.A. and Lade, P.V. (1998). Steady state concepts and static liquefaction of silty sands. J. Geotech. Geoenv. Eng. ASCE 124, 9, 868-877.

[16] Yamamuro, J. A. and Wood, F. M. (2004). Effect of depositional method on the undained behavior and microstructure of sand with silt. Soil Dynamics and Earthquake Engineering 24, 751-760.

[17] Yamamuro, J. A., Wood, F. M. and Lade, P. V. (2008). Effect of depositional method on the microstructure of silty sand. Canadian Geotechnical Journal 45, 11, 1538–1555.
[18] Zlatovic, S. and Ishihara, K. (1997). Normalized behavior of very loose non-plastic soils: effects of fabric. Soils and Foundations 37, 4, 47-56.

PREVERJANJE ZANESLJIVOSTI INSTRUMENTOV ZA BELEŽENJE HORIZONTALNO-VERTIKALNEGA SPEKTRALNEGA RAZMERJA MIKROTREMORJEV

IZIDOR TASIČ IN FRANC RUNOVC

o avtorjih

Izidor Tasič
Agencija Republike Slovenije za okolje
Vojkova cesta 1b, 1000 Ljubljana, Slovenija
E-pošta: izidor.tasic@gov.si

Franc Runovc *
Univerza v Ljubljani,
Naravoslovnotehniška fakulteta
Aškerčeva 12, 1000 Ljubljana, Slovenija
E-pošta: franc.runovc@ntf.uni-lj.si

* vodilni avtor

izvleček

Nepreverjeni seizmološki merilni sistemi lahko povzročijo oporečno karto potresne mikrorajonizacije. Karta potresne mikrorajonizacije, ki je namenjena potresno odpornemu načrtovanju, je lahko zasnovana - poleg nekaterih drugih postopkov - na podlagi analize spektralnega razmerja vodoravnih in navpične komponente mikrotremorjev. Mikrotremorje beležimo z modernimi seizmološkimi sistemi. Spremembe v prenosni funkciji seizmološkega sistema, če le-te niso zabeležene in upoštevane, vplivajo na rezultat in s tem tudi na interpretacijo meritve ter tako posledično na zanesljivost celotnega postopka priprave karte potresne mikrorajonizacije. Zato je potrebno seizmološke sisteme primerno verificirati. Razvili smo postopek, kjer s pomočjo dveh referenčnih seizmoloških sistemov preverimo vpliv prenosih funkcij testiranega sistema na krivuljo spektralnega razmerja mikrotremorjev, ne da bi vnaprej poznali prenosne funkcije kateregakoli od sistemov. Postopek smo prikazali na seizmometru Lennartz LE-3D/5s in na seizmoloških sistemu TROMINO, kjer smo za referenčna seizmometra uporabili širokopasovna seizmometra STS-2.

ključne besede

potresna mikrorajonizacija, spektralno razmerje med vodoravnima in navpično komponento, vibracije tal, mikrotremor, prenosna funkcija seizmološkega sistema, kalibracija in zanesljivost seizmološkega sistema

HOW TO TEST THE RELIABILITY OF INSTRUMENTS USED IN MICROTREMOR HORIZONTAL-TO-VERTICAL SPECTRAL RATIO MEASUREMENTS

IZIDOR TASIČ and FRANC RUNOVC

About the authors

Izidor Tasič
Environmental Agency of the Republic of Slovenia,
Vojkova cesta 1b, 1000 Ljubljana, Slovenia
E-mail: izidor.tasic@gov.si

Franc Runovc *
University of Ljubljana,
Faculty of Natural Sciences and Engineering
Aškerčeva cesta 12, 1000 Ljubljana, Slovenia
E-mail: franc.runovc@ntf.uni-lj.si

* Corresponding author

Abstract

The reliability of a horizontal-to-vertical spectral ratio (HVSR) curve depends on the results obtained by a verified seismological system. Seismic microzonation provides the basis for a site-specific risk analysis and it can be evaluated using the microtremor HVSR method, where the data are recorded using modern seismological systems. Changes in the transfer function of seismological systems affect the HVSR curve and, consequently, also its interpretation, if these changes are not detected and taken into consideration while performing the microtremor spectral calculations. The reliability of the seismic microzonation performed by such a procedure becomes questionable. An algorithm is developed with a two references system, where the influence of the transfer function on the HVSR curve by the tested system can be evaluated without any a-priori knowledge regarding the transfer functions of any of the systems. This approach is applied to a Lennartz Le-3D/5s seismometer and to a TROMINO seismological system, where two Streckeisen STS2 seismometers are used as the reference systems.

Keywords

seismic microzonation, horizontal-to-vertical spectral ratio method, ambient vibrations, microtremor, seismic system transfer function, reliability and calibration of seismic systems

1 INTRODUCTION

Seismic microzonation is the process of estimating the response of soil layers under earthquake excitations and thus the variation of the earthquake characteristics on the ground surface [1]. Microzonation provides the basis for a site-specific risk analysis, which can assist in the mitigation of earthquake damage [2]. The dynamic characteristics of a site, such as the predominant period, the amplification factor, the shear-wave velocity and the standard penetration test values can be used for seismic microzonation purposes. The shear-wave velocity measurement and the standard penetration test are generally considered to be expensive and are not feasible for a large number of sites for the purpose of microzonation. The microtremor measurement has become a popular method for determining the dynamic characteristics of a site and is being extensively used for microzonation. Microtremors are short-period vibrations resulting from coastal effects, atmospheric loading, the wind's interaction with structures and vegetation, and cultural sources. The microtremor horizontal-to-vertical spectral ratio (HVSR) method, initially proposed by Nogoshi and Igarashi [3] and later popularized by Nakamura [4], is widely used for microzonation projects in order to identify possible site effects [5], [6], or to identify the main frequencies of buildings and their vulnerability to earthquakes [7]. The main advantages of the HVSR method are the simple and low-cost measurements that can be performed at any time and at any location without any specific knowledge regarding the geological structure of what is beneath the ground. This method produces an estimate of the site's geological conditions by providing the peak period of amplification from the HVSR. The amplification occurs where the ratio of amplitudes is greater than one [8]. However, the HVSR technique is not sufficient to characterize the complexity of site effects, in particular the absolute values of the seismic amplification [5].

In HVSR measurements, three seismic sensors that are perpendicular to each other, simultaneously measure

the ground movements in two horizontal and one vertical direction. A simple, vague recipe for the instruments in HVSR measurements that most people are applying is [7]: "Take whatever instrument you think is able to measure very weak ground motion, let it work on the site of your choice for the time you want, at the sample rate you prefer. Whatever A/D converter you use is fine. Aim for stationarity during quiet periods at night-time or, if you prefer, record heavy road traffic. Taper or not, filter or not, base-line correct or not, then perform an FFT, or some other time-domain/frequency-domain transform on separate components, then add averaging, to your taste. Before or after this last operation, take the ratio of the horizontal to vertical spectra, select the average of all the ratios (or the average plus the standard deviation) et voilà, site amplification is ready".
This simple recipe should not be acceptable without hesitation, because a seismic instrument can have an influence on the HVSR calculation and finally on the result and interpretation. Seismic sensors are mostly based on the inertial principle, where the ground motion is measured relative to the inertial reference mass [9]. Modern seismic sensors convert ground motion into electric signals. In a conventional, inertial, short-period seismometer, the ground acceleration is first converted into a relative displacement between the seismic mass and the frame, and then this displacement or its velocity is converted into an electrical signal. Experience has shown that their eigenperiod and the attenuation may change with time up to several tens of percent, especially when these instruments are repeatedly deployed in temporary installations [9]. Changes of this order can cause imperfections in the HVSR measurements. When the ratio of the transfer functions is not 1, it can bias the H/V curve and consequently also its interpretation. Figure 1 shows the ratio between the horizontal and vertical transfer functions for a 4.5-Hz geophone, in the case when the eigen frequency, the damping coefficient and the transduction constant between the vertical and horizontal sensors differ by only 5%. For the same reason "Guidelines for the implementation of the H/V spectral ratio technique on ambient vibrations" [5] do not recommend the use of sensors that have their natural frequency above the lowest frequency of interest. Broadband seismometers use the negative force feedback to keep the motion of the mass small. Using this principle, the mechanical imperfections of the sensor are mostly avoided [10]. The feedback principle of a broadband seismometer also means that at some predefined frequency the sensors have a flat response and it also means that the transfer properties of the sensors in this frequency band are stable. Because of this, the producer of a seismometer guarantees the long-term stability of the seismometer's transfer function and they do not specify any corrections in the time period in their calibration certificates (e.g., [11]). These seismometers are not easy to use in the field for short-term experiments because of their relatively long stabilization time, as well as their sensitivity to temperature and pressure variations.

When using broadband or short-period seismometers, it appears necessary to check or validate the instruments in the studied frequency band for an optimal analysis of the HVSR curve. The two following situations need to be checked:

- Does the ratio of the transfer functions affect the HVSR curve?
- Can the self-noise of an instrument affect the HVSR curve?

The instruments can be checked with a reference seismological system using the ground noise, where both the reference and the tested system are placed next to each other - this is the most popular way [12], [13]. This technique was also used in extensive research work [14], where the influence of the instruments on the HVSR curve for ambient vibrations was investigated. These authors compared the differences between the HVSR curves of reference and tested systems for 18 sensors.

The main disadvantage of using the difference between a tested and a reference seismometer to define the quality of the tested system is that the seismic signal is not canceled out: the difference is a function of the transfer functions and of the seismic signals. If the ratio of the HVSR curves between the tested and the reference system is used instead of the difference itself, the seismic signal is canceled out. But in this case we need to be careful how to interpret the results. Reference systems are usually broadband seismometers, with a similar or better quality level than tested systems. But the comparison with this type of reference systems is often wrongly equated with a calibration. In a calibration procedure, the reference system needs to be periodically (at least annually, unless otherwise justified or required) calibrated by a higher-level standard or by an external reference, and all the procedures and changes of the reference instrument need to be traceable. The traceability is defined, in this case, as an unbroken chain of comparisons to national or international standards with stated uncertainties at each step.

Broadband seismometers usually come with a so-called "certificate of calibration" provided by producers. But after that, these seismometers are very rarely, if it at all, compared or calibrated using higher-level standards.

The reason for this is very simple. A high-quality broadband seismometer, such as the STS-2 from Streckeisen, the Trillium 240 from Nanometrics or the CMG-3T from Guralp, which can reach the price of a mid-level car, are usually permanently and precisely installed at a seismic station, with the main purpose being to detect seismic signals. Because of the known long-term stability of seismometer's transfer function (e.g., [11]), a periodic de-installation, transportation to an institution where the calibration is performed, and once again installation at the seismic station, may cause more problems than are solved by a regular calibration: it is difficult to place the seismometer exactly as it was before; the out-of-operation time of the seismic station can be prolonged; after the reinstallation, the seismometer needs days to be stabilized again [15]; and there is always a risk that the instrument will be damaged during the transport. These types of seismometers are usually just periodically controlled with test (or calibration) signals, which are built in acquisition units. (Using test signals from acquisition units is often wrongly equated with calibration. The test signal sources are also not periodically calibrated by higher-level standards or by an external reference.) Only in cases when the response of a seismometer to the test signals is unusual is the seismometer returned back to the manufacturer for verification. Situations where broadband seismometers are used as reference units are very rare and are more or less coincidental. Because of this we need to be aware that when using a broadband seismometer as a reference unit, the parameters of the tested systems are only defined or estimated relative to this particular, non-calibrated reference unit.

By using two broadband seismometers - of higher quality than those of the tested system - at the same time as the reference units, the uncertainty of the measurement results can be minimized. The purpose of this paper is to present a simple test to check the reliability of the instruments used in the HVRS method by using two reference systems without any a-priori knowledge of the transfer function of any of the systems. This approach will be applied to a Lennartz Le-3D/5s [16] and to a TROMINO seismological system [17] where two Streckeisen STS-2 seismometers [15] are going to be used as the reference systems.

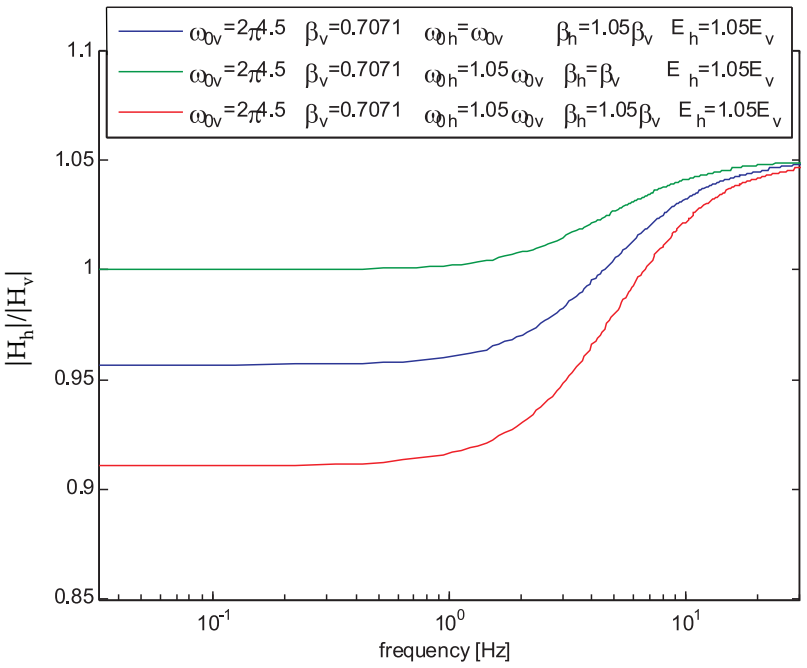

Figure 1. An electrodynamic seismometer, also called a geophone, converts the motion of a mass into an electrical signal using an electromagnetic velocity transducer. The frequency-dependent complex response functions depend on the eigen frequency ω_0, the damping factor β and the transduction constant E [18]. The plot depicts the ratio of the transfer functions for a 4.5-Hz geophone in two-dimensional space (vertical and horizontal), when the difference between the eigen frequencies, the damping coefficients and the transduction constants of the vertical and horizontal sensor is only 5%.

2 MATHEMATICAL MODEL

We present the model in two-dimensional space, using the horizontal and the vertical directions. The measurement is performed by seismological systems with two similar sensors with a linear transfer function, being orthogonal to each other and set up one in the vertical and the other in the horizontal direction. First, we will assume that both the vertical and horizontal sensors detect the same (seismic) signal x. The output y_h of the horizontal sensor can be written as the convolution of the input signal x with the sensor's transfer function h_h:

$$y_{\mathrm{h}} = h_{\mathrm{h}} \otimes x\,, \qquad (1)$$

Here, the symbol $\otimes$ denotes the convolution. Similarly, the output y_v of the vertical sensor is the convolution of the input signal x with the sensor's transfer function h_v:

$$y_{\mathrm{v}} = h_{\mathrm{v}} \otimes x \qquad (2)$$

We assume here, that there is no internal noise. These equations translate into the frequency domain as:

$$Y_{\mathrm{h}} = H_{\mathrm{h}} X\,, \qquad (3)$$
$$Y_{\mathrm{v}} = H_{\mathrm{v}} X\,, \qquad (4)$$

where Y_h, Y_v, X, H_h and H_v represent the Fourier transforms of y_h, y_v, x, h_h and h_v. Assuming that both systems are linear and noise-free, the output power spectral density (PSD) can be expressed by:

$$\mathrm{P}_{\mathrm{hh}} = H_{\mathrm{h}} H_{\mathrm{h}}^{*} \mathrm{P}_{xx}\,, \qquad (5)$$
$$\mathrm{P}_{\mathrm{vv}} = H_{\mathrm{v}} H_{\mathrm{v}}^{*} \mathrm{P}_{xx}\,, \qquad (6)$$

The symbol * denotes the complex conjugation, and $\mathrm{P}_{\mathrm{xx}} = XX^{*}$ is assumed to be the coherent ground-motion power spectral density. The horizontal-to-vertical spectral ratio HVSR is defined as

$$\mathrm{HVSR} = \sqrt{\frac{\mathrm{P}_{\mathrm{hh}}}{\mathrm{P}_{\mathrm{vv}}}}\,. \qquad (7)$$

When the same seismic signal x is detected by both systems, the HVSR ratio is affected only by differences in the transfer functions of the used sensors. The ratio of the square magnitude of the transfer functions of the tested seismological system reduces in this particular case to:

$$\frac{H_{\mathrm{h}} H_{\mathrm{h}}^{*}}{H_{\mathrm{v}} H_{\mathrm{v}}^{*}} = \mathrm{HVSR}^{2} = \frac{\mathrm{P}_{\mathrm{hh}}}{\mathrm{P}_{\mathrm{vv}}}\,. \qquad (8)$$

The instruments where this ratio is 1 are trustworthy and can be used in the HVSR measurements.

Under real circumstances, the signals of the horizontal and the vertical components are very rarely equal. A more realistic case is that we have different seismic signals in the horizontal and the vertical directions. Equations (5) and (6) are now rewritten:

$$\mathrm{P}_{\mathrm{hh}} = \mathrm{H}_{\mathrm{h}} \mathrm{H}_{\mathrm{h}}^{*} \mathrm{P}_{x_h x_h} \qquad (9)$$
$$\mathrm{P}_{\mathrm{vv}} = \mathrm{H}_{\mathrm{v}} \mathrm{H}_{\mathrm{v}}^{*} \mathrm{P}_{x_v x_v} \qquad (10)$$

The expression $\mathrm{P}_{x_h x_h} = X_h X_h^{*}$ is assumed to be the coherent ground-motion power spectral density in the horizontal direction and $\mathrm{P}_{x_v x_v} = X_v X_v^{*}$ the coherent ground-motion power spectral density in the vertical direction.

A simple procedure to check the reliability of the HVSR of particular instruments involves putting it close to a reference seismological system with an equal or better quality class. The output PSD of the reference instrument can be expressed by using the index 'r':

$$\mathrm{P}_{\mathrm{h_r h_r}} = \mathrm{H}_{\mathrm{h_r}} \mathrm{H}_{\mathrm{h_r}}^{*} \mathrm{P}_{x_h x_h} \qquad (11)$$
$$\mathrm{P}_{\mathrm{v_r v_r}} = \mathrm{H}_{\mathrm{v_r}} \mathrm{H}_{\mathrm{v_r}}^{*} \mathrm{P}_{x_v x_v} \qquad (12)$$

where $\mathrm{H}_{\mathrm{h_r}}$ and $\mathrm{H}_{\mathrm{v_r}}$ represent the Fourier transforms of the references sensors' transfer functions $h_{\mathrm{h_r}}$ and $h_{\mathrm{v_r}}$. Let us presume that the reference system is not calibrated, as written and defined in the previous section. In this case, the ratio of transfer functions of the reference systems $\left|\mathrm{H}_{\mathrm{h_r}}\right| / \left|\mathrm{H}_{\mathrm{v_r}}\right|$ is unknown. If, for testing purposes, we use the difference of the HVSR curves of a tested and of a reference system, a function of both transfer functions and also of a seismic signal is obtained:

$$\Delta = \mathrm{HVSR} - \mathrm{HVSR}_{\mathrm{r}} = \sqrt{\frac{\mathrm{P}_{x_h x_h}}{\mathrm{P}_{x_v x_v}}} \left(\sqrt{\frac{\mathrm{H}_{\mathrm{h}} \mathrm{H}_{\mathrm{h}}^{*}}{\mathrm{H}_{\mathrm{v}} \mathrm{H}_{\mathrm{v}}^{*}}} - \sqrt{\frac{\mathrm{H}_{\mathrm{h_r}} \mathrm{H}_{\mathrm{h_r}}^{*}}{\mathrm{H}_{\mathrm{v_r}} \mathrm{H}_{\mathrm{v_r}}^{*}}} \right) =$$
$$= f\left(X_h, X_v, \mathrm{H}_{\mathrm{h}}, \mathrm{H}_{\mathrm{v}}, \mathrm{H}_{\mathrm{h_r}}, \mathrm{H}_{\mathrm{v_r}}\right), \qquad (13)$$

where the index r represents the reference system. Because this expression still includes the unknown seismic signal, equation (13) cannot be applied to uniformly evaluate the influence of the transfer function of the system under test on the calculated HVSR ratio. The ratio of HVSR between the tested and reference system caused the seismic signal to be canceled out. If the reference system is ideal, meaning $h_{\mathrm{h_r}} = h_{\mathrm{v_r}}$, the information about the transfer function can be evaluated:

$$\sqrt{\frac{\mathrm{H}_{\mathrm{h}} \mathrm{H}_{\mathrm{h}}^{*}}{\mathrm{H}_{\mathrm{v}} \mathrm{H}_{\mathrm{v}}^{*}}} = \sqrt{\frac{\mathrm{P}_{\mathrm{hh}}}{\mathrm{P}_{\mathrm{vv}}}} \frac{1}{\mathrm{HVSR}_{r}}\,. \qquad (14)$$

Using a non-calibrated reference system, the ratio of HVSR between the tested and the reference is still an unknown function:

$$\sqrt{\frac{H_h H_h^* H_{v_r} H_{v_r}^*}{H_v H_v^* H_{h_r} H_{h_r}^*}} = \sqrt{\frac{P_{hh}}{P_{vv}}} \frac{1}{HVSR_r}. \qquad (15)$$

In the case where only one non-calibrated reference system is used, there is no information about in which frequency band or if at all, the calculation is trustworthy. A more promising procedure to check the reliability of the HVSR of particular instruments is by putting it close to two reference seismological systems, where both references system have much better characteristics than the tested one. We will assume that these two seismological systems are composed of two high-quality broad-band seismometers, which have the manufacturer's "certificate of calibration", but were never calibrated again after that.

The first step is to define the frequency interval where the two systems can be used as a reference.

The frequency interval where the two systems can be used as reference units is defined by:

$$\frac{HVSR_{r_1}}{HVSR_{r_2}} = 1, \qquad (16)$$

where the indices r_1 and r_2 refer to the first and second reference systems. In reality, this is almost never true. While seismometer manufacturers certainly attempt to build their instruments with equal characteristics, in practice there will almost always be some difference, at least in the mechanical alignment of the two systems and in small deviations in the transfer functions and generator constants. Considering this, equation (16) needs to be adjusted by:

$$\left| \frac{HVSR_{r_1}}{HVSR_{r_2}} - 1 \right| \leq \delta; \ \delta \ll 1. \qquad (17)$$

The value δ represents an acceptable error. In the HVSR calculations, this ratio is represented by smoothed PSD estimates [5]. The PSD estimates of seismic signals can be noisy themselves, and the smoothing would make them much cleaner [12]. At the same time, the smoothing of the PSD makes it possible to use reference systems with different sampling rates than off the tested system. The value δ depends on a smoothing procedure, and in our cases it was 0.02. The frequency interval where the reference system can be used is defined by the range where δ is continuously below this value.

Although we have two reference systems, we still do not know which of them is better. The next step is to use both reference systems to evaluate the ratio of the transfer functions of the tested system. The easiest way is just to employ the average value using both reference systems from equation (14):

$$\widehat{\frac{|H_h|}{|H_v|}} = \sqrt{\frac{P_{hh}}{P_{vv}}} \left(\frac{HVSR_{r_1} + HVSR_{r_2}}{2HVSR_{r_1} HVSR_{r_2}} \right). \qquad (18)$$

Another possibility is to calculate the average value for the square ratio of the transfer functions first, and then to take a square root of the complete expression:

$$\widehat{\frac{|H_h|}{|H_v|}} = \sqrt{\frac{P_{hh}}{P_{vv}} \left(\frac{HVSR_{r_1}^2 + HVSR_{r_2}^2}{2HVSR_{r_1}^2 HVSR_{r_2}^2} \right)}. \qquad (19)$$

The third possibility is to estimate the ratio of the transfer functions by using a simple mathematical manipulation. First, equation (13) is rewritten in a different form:

$$\left(\frac{H_h H_h^*}{H_v H_v^*} - \frac{H_{h_\eta} H_{h_\eta}^*}{H_{v_\eta} H_{v_\eta}^*} \right) \frac{P_{x_h x_h}}{P_{x_v x_v}} = \frac{P_{hh}}{P_{vv}} - HVRS_{r_1}^2. \qquad (20)$$

At this point we will assume that both reference systems are ideal and the ratio of the transfer functions of the reference systems are equal: $H_{hr_i} H_{hr_i}^* = H_{vr_i} H_{vr_i}^*$ for i=1, 2. The left-hand side of equation (20) reduces to:

$$\left(\frac{H_h H_h^*}{H_v H_v^*} - 1 \right) HVRS_{r_1}^2 = \frac{P_{hh}}{P_{vv}} - HVRS_{r_1}^2. \qquad (21)$$

Using equation (16), the right-hand side of equation (21) can be rewritten using the second reference system ($HVRS_{r_1}^2 = HVRS_{r_2}^2$):

$$\left(\frac{H_h H_h^*}{H_v H_v^*} - 1 \right) HVRS_{r_1}^2 = \frac{P_{hh}}{P_{vv}} - HVRS_{r_2}^2. \qquad (22)$$

Using equation (22), the square ratio of the transfer functions is:

$$\frac{H_h H_h^*}{H_v H_v^*} = \frac{\frac{P_{hh}}{P_{vv}} - HVRS_{r_2}^2 + HVRS_{r_1}^2}{HVRS_{r_1}^2}. \qquad (23)$$

The right-hand side of equation (23) can be written as an average value of both combinations of reference systems:

$$\overline{\frac{H_h H_h^*}{H_v H_v^*}} = \frac{1}{2} \left(\frac{\frac{P_{hh}}{P_{vv}} - HVRS_{r_2}^2 + HVRS_{r_1}^2}{HVRS_{r_1}^2} + \frac{\frac{P_{hh}}{P_{vv}} - HVRS_{r_1}^2 + HVRS_{r_2}^2}{HVRS_{r_2}^2} \right) \qquad (24)$$

Equation (24) can be rewritten as:

$$\widetilde{\frac{|H_h|}{|H_v|}} = \sqrt{\frac{\frac{P_{hh}}{P_{vv}} \left(HVRS_{r_2}^2 + HVRS_{r_1}^2 \right) - \left(HVRS_{r_2}^2 - HVRS_{r_1}^2 \right)^2}{2HVRS_{r_1}^2 HVRS_{r_2}^2}}. \qquad (25)$$

If both reference systems are ideal ($HVRS^2_{r_2} = HVRS^2_{r_1}$), then equation (25) is transformed into equation (14). If the square part of the right-hand side of equation (25) is neglected ($\left(HVRS^2_{r_2} - HVRS^2_{r_1}\right)^2 \approx 0$), then this equation reduces to equation (19). Equation (25) is only valid in the frequency interval where both reference systems are almost equal, and considering this equation (25) can be expanded using the Taylor series:

$$\frac{\widetilde{|H_h|}}{|H_v|} = \sqrt{\frac{\frac{P_{hh}}{P_{vv}}\left(HVRS^2_{r_2} + HVRS^2_{r_1}\right)}{2HVRS^2_{r_1}HVRS^2_{r_2}}}\left(1 - \frac{1}{2}\frac{\left(HVRS^2_{r_2} - HVRS^2_{r_1}\right)^2}{\frac{P_{hh}}{P_{vv}}\left(HVRS^2_{r_2} + HVRS^2_{r_1}\right)}\right). \quad (26)$$

This is the next relation for the "estimation" of the ratio of the transfer functions of the tested system. Using equation (26) another condition must be fulfilled for the frequency interval where two reference systems can be used:

$$\frac{\left(HVRS^2_{r_2} - HVRS^2_{r_1}\right)^2}{\frac{P_{hh}}{P_{vv}}\left(HVRS^2_{r_2} + HVRS^2_{r_1}\right)} \le \delta_t;\ \delta_t \ll 1. \quad (27)$$

The value δ_t depends on the smoothing procedure and in our case it was 0.0002. In the frequency interval where both reference systems are almost equal, the differences between equations (18), (19) and (26) are practically insignificant, and any of the three equations can be used.

The benefit of using two reference systems instead of one is that we have a defined frequency interval where the test can be performed. Also, no information regarding the transfer functions of the reference systems are needed to evaluate the influence of the tested system on the HVSR calculation. Again (as in equation (8)) the tested instruments, where this ratio is 1, are trustworthy and can be used in the HVSR measurements. But when using a non-ideal reference system, a small deviation δ_h from the value 1 can be allowed:

$$\left|\frac{\widetilde{|H_h|}}{|H_v|} - 1\right| \le \delta_h;\ \ \delta_h \ll 1. \quad (28)$$

The value δ_h depends on a smoothing procedure and in our cases it was 0.05.

In a similar way and with the same assumptions, the estimation of the square magnitude of the transfer function of an unknown system can be evaluated using equation (19):

$$\widetilde{H_k H_k^*} = \left(\frac{P_{kk}\left(P_{kr_1kr_1} + P_{kr_2kr_2}\right)}{2P_{kr_1kr_1}P_{kr_2kr_2}}\right);\ \text{k=h,v}, \quad (29)$$

or using equation (25):

$$\widetilde{H_k H_k^*} = \frac{P_{kk}\left(P_{kr_1kr_1} + P_{kr_2kr_2}\right)}{2P_{kr_1kr_1}P_{kr_2kr_2}}\left(1 - \frac{\left(P_{kr_1kr_1} - P_{kr_2kr_2}\right)^2}{P_{kk}\left(P_{kr_1kr_1} + P_{kr_2kr_2}\right)}\right); \quad (30)$$

k=h,v .

Here, the index 'k' represents the horizontal (h) and the index 'v' the vertical (v) component, respectively. In this case, the transfer function of the reference system needs to be flat in the frequency interval of the observation or the power spectra of the reference systems need to be corrected using the instrumental correction.

3 INFLUENCE OF THE INSTRUMENTAL NOISE

All the previous equations are based on an assumption that the self-noise of all the instruments involved is negligibly small (e.g., much smaller than the seismic signal). This requirement is also applied to instruments used in the measurements of the HVSR calculations of ambient vibrations. The self-noise can affect the calculation because it appears to increase the seismic signal. The error is the result of self-noise, and it can be represented by:

$$\sqrt{X_k X_k^* + N_k N_k^*} = \sqrt{X_k X_k^*}(1 + er_k)\ ;\ \text{k=h,v}. \quad (31)$$

The symbol N_k represents the Fourier transform of the instrumental noise n_k (k = h, v) and the symbol er_k represents an error. We assume that the instrumental noise and the seismic signal are uncorrelated. The last equation can be rewritten:

$$\sqrt{1 + \frac{N_k N_k^*}{X_k X_k^*}} = (1 + er_k)\ ;\ \text{k=h,v}. \quad (32)$$

The ratio between $X_k X_k^*$ and $N_k N_k^*$ is:

$$\frac{X_k X_k^*}{N_k N_k^*} = \frac{1}{(1 + er_k)^2 - 1}\ ;\ \text{k=h,v}. \quad (33)$$

The seismic noise spectra are usually represented by the PSD plots and reported in dB relative to 1 $(m/s^2)^2/Hz$ or to 1 $(m/s)^2/Hz$. The acceptable difference between the seismic signal and the instrumental noise (in dB) is calculated with the predefined value of er_k:

$$\Delta_{dB} = 10\log_{10}\left(\frac{X_k X_k^*}{N_k N_k^*}\right) = 10\log_{10}\left(\frac{1}{\left(1 + er_k\right)^2 - 1}\right). \quad (34)$$

If an error of 1% is acceptable, then the seismic signal X_k needs to be larger than the self-noise N_k by at least 17 dB.

In the case of a 5% acceptable error the difference needs to be at least 10 dB. If the difference is lower than these values, the self-noise starts to affect the calculations. It is preferable that the self-noise of a particular instrument should be evaluated before its first use in the HVSR calculations. The self-noise can be obtained using "Three-channel Correlation Analysis Techniques" [19]. Before any analysis of an HVRS calculation, the difference between the PSD of a seismic signal and the PSD of the instrumental noise needs to be estimated and defined, because the self-noise can have an influence on the measurements.

4 CASE STUDIES

Side-by-side measurements using different seismic instruments were performed at the same time in September 2008 at the Golovec Observatory, Ljubljana (LJU). Two STS-2 seismometers [15] were used as the reference systems. The first STS-2 seismometer was connected to the Quanterra Q730 [20] acquisition unit and the second one was connected to the EarthData PR6 [21] acquisition unit. The data were sampled at 200 sps. The input in our experiment was a one-hour, finite-length time seismic data segment. The power spectral density (PSD) estimations for both reference systems are depicted in Figure 2. The Welch method for the power spectral density estimation was applied using a Matlab® built-in function. The frequency response of the STS-2 seismometers lies in the frequency interval between 0.008 Hz and 50 Hz. Figure 3 shows the curves that were calculated using equations (17) and (27). Because the HVSR of the tested signal is also included in equation (27), the HVSR of LE-3D/5s was used for the calculation. From Figure 3 it is possible to estimate the frequency interval where two reference system systems can be used in this experiment to be between 0.1Hz and 9 Hz.

4.1 LENNARTZ LE-3D/5S SEISMOMETER (S/N 059)

The Lennartz LE-3D/5s [16] seismometer is widely used for microtremor measurements. Theoretically, it has a flat response to the velocity from 0.2 Hz. The Lennartz LE-3D/5s seismometer (s/n 059, manufactured in 1992) was connected to an Earth Data PR6 acquisition unit [21], and the signal was sampled at 200 samples per second. The HVSR curve of the LE-3D/5s system differs slightly for both STS-2 systems only at low frequencies (Figure 4).The evaluated ratio for the LE-3D/5s seismometer s/n 059 shows us that this seismometer can be used for reliable HVSR measurements beyond 0.25 Hz without any problems (Figure 5). Because of this the value of δ_h can be defined as 0.05. In the frequency range between 0.11 Hz and 0.25 Hz the instrumental correction for all the components is needed for this seismometer. Below 0.11 Hz the self-noise of the LE-3D/5s instrument critically affects this particular measurement. As

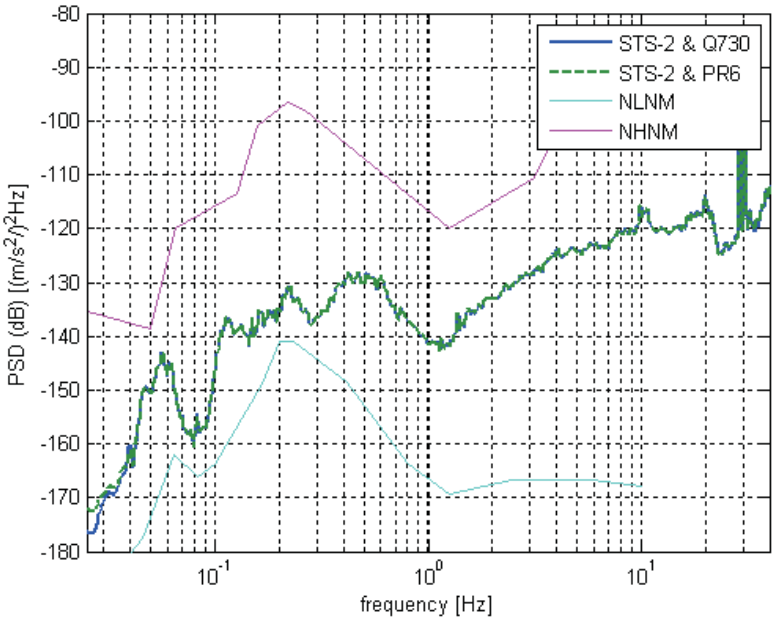

Figure 2. Power spectral density curves for the vertical component for both reference systems, compared to the standard seismic noise models of the Earth [22].

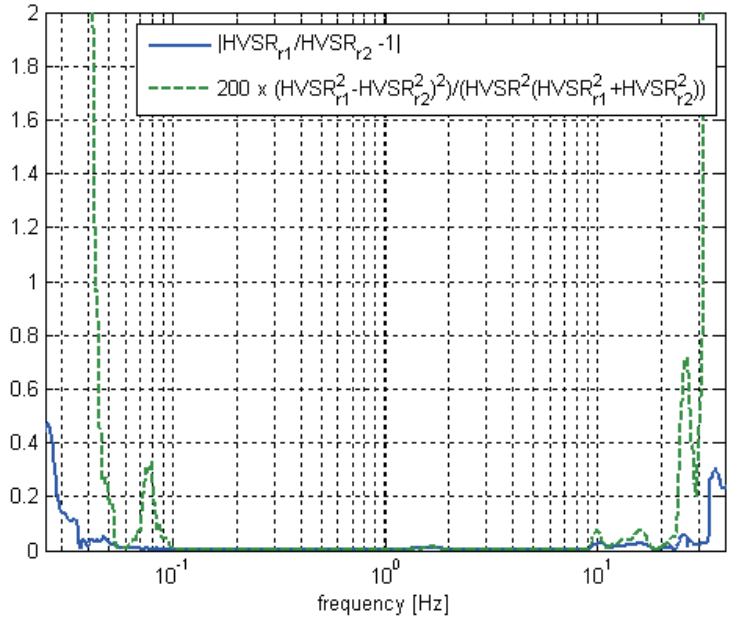

Figure 3. The frequency interval where two references seismological systems can be used in this experiment was defined by equation (17) (blue line) and by equation (27) (green line). In equation (27) the HVSR of LE-3D/5s is also used and for a clearer presentation the curve is multiplied by a factor of 200. In the frequency interval between 0.1 Hz and 9 Hz two seismological systems with STS-2 seismometers can be used as reference systems. Equation (27) gives more sharp boundaries and looks more useful, but we recommended using both equations.

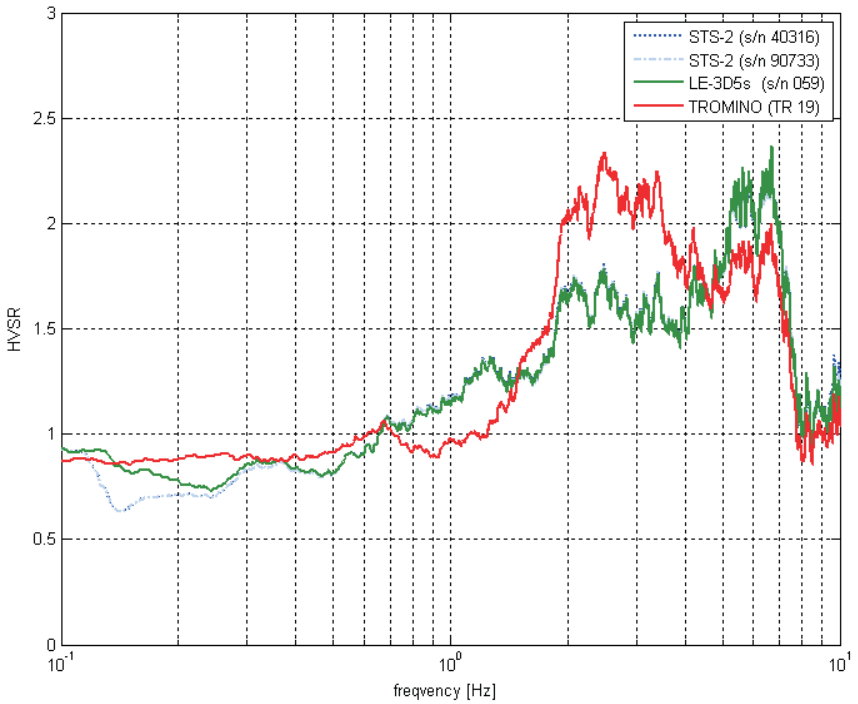

Figure 4. The HVSR for 4 seismological systems, two STS-2 seismometers (STS-2 s/n 40316, connected to the Q730, STS-2 s/n 90733 connected to the PR6 acquisition unit), the LE-3D/5s seismometer (s/n 59 connected to the PR6 acquisition unit) and the TROMINO instrument (TR-00019). The HVSR of the TROMINO instruments noticeably differs in the frequency interval from 0.8Hz to 8 Hz compared to the HVSR of systems with STS-2 seismometers, while the HVSR of LE-3D/5s system only differs slightly at lower frequencies.

is clear from Figure 5, the ratio of the transfer functions drastically changes its slope at 0.11Hz. This situation can be explained by the influence of the instrumental noise. Using figure 6 one can define an acceptable difference between the PSD of the estimated self-noise curve and the PSD of the recorded seismic signal for the LE-3D/5s seismometer to be approximately 15 dB.

4.2 TROMINO (TR-0019)

TROMINO systems [17] are mostly used for microtremor measurements. They are composed of three orthogonal electrodynamic velocity sensors, a GPS receiver, a digitizer and a recording unit with a flash-memory card. All the parts are integrated into a common case. The Tromino under the test (TR-19) was manufactured in 2005 and was in service in January 2008. This Tromino belongs to the first generation of these instruments. The Trominos released in the following years were completely redesigned and should have better characteristics. In our test, the TROMINO instrument data were sampled at 256 sps. The HVSR curves for the TROMINO instrument noticeably differ from the HVSR curves of systems with STS-2 seismometers (Figure 4). When the self-noise of the system is estimated and using a boundary of the allowed 15 dB difference between the seismic noise PSD and the instrument self-noise PSD (Figure 6), which is defined on the basis of the Lennartz Le-3D/5s seismometer, then in this particular case the self-noise of the instrument affects the HVSR calculation below 3Hz. Because of this, the ratio of the transfer functions - as depicted in Figure 7 - for the TROMINO system (TR- 19) cannot be correctly evaluated in this particular case below 3 Hz. The self-noise of the TROMINO system (TR-19) is high: it is much higher than the NLNM (New Low Noise Model, [22], [23]). This instrument cannot be used without any instrumental correction for all the components in the frequency interval between 3 Hz and 8 Hz. Above 8 Hz, just the transduction constants of all components need to be redefined. In this particular case, we cannot say anything about the ratio of the transfer functions below 3 Hz, because of the relatively high instrumental noise with respect to the seismic noise.

5 CONCLUSIONS

The document "Guidelines for the implementation of the H/V spectral ratio technique on ambient vibrations" [5] states that “The first requirement, before any extraction

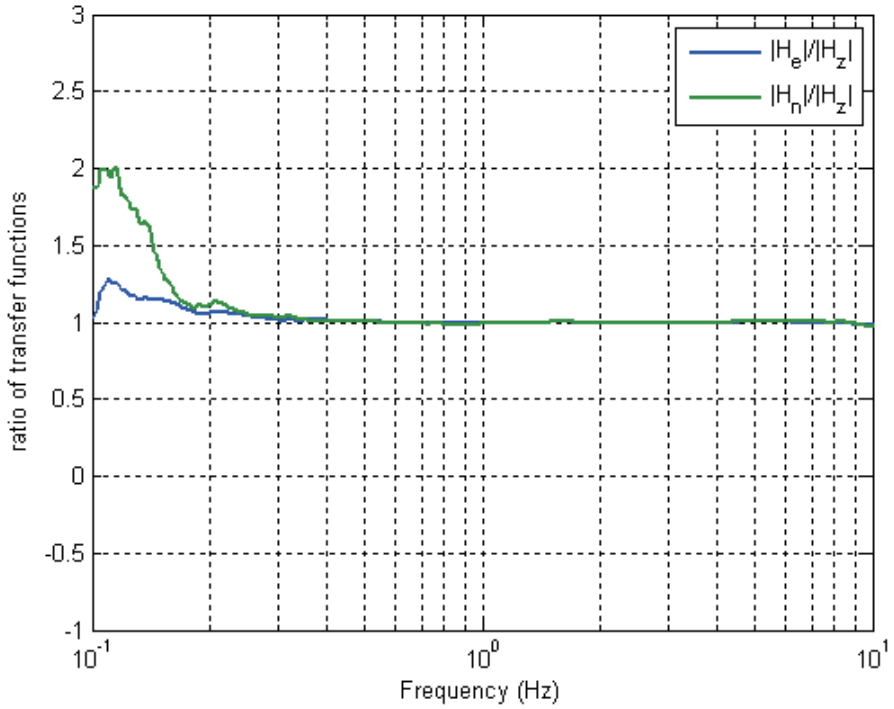

Figure 5. The ratio of transfer functions for an LE-3D/5s seismological system computed using equation (26), the ratio of the transfer functions of the E-W and the vertical component (blue line), the ratio of the transfer function of the N-S component and the vertical component (green line). The ratio of the transfer functions drastically changes its slope at 0.11Hz and can be explained by the influence of the instrumental noise.

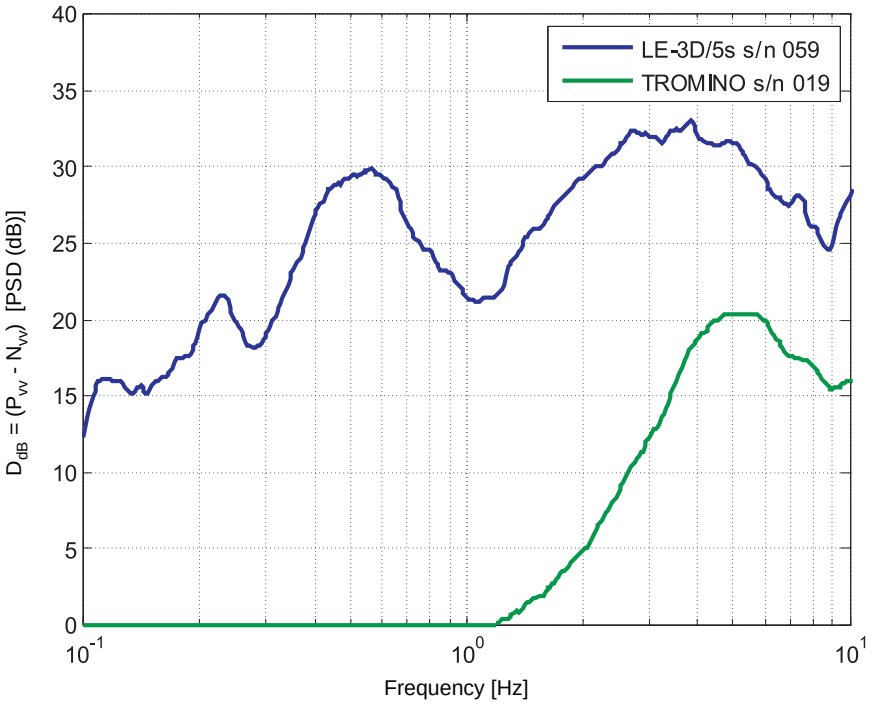

Figure 6. The difference between the PSD of the estimated self-noise curve (N_{vv}) estimated by "Three-channel Correlation Analysis Techniques" [19] and the PSD of the recorded seismic signal (P_{vv}) for the LE-3D/5s seismometer (s/n 59) and TROMINO (TR 19), for the vertical component. The self-noise of the TROMINO instrument is considerably higher.

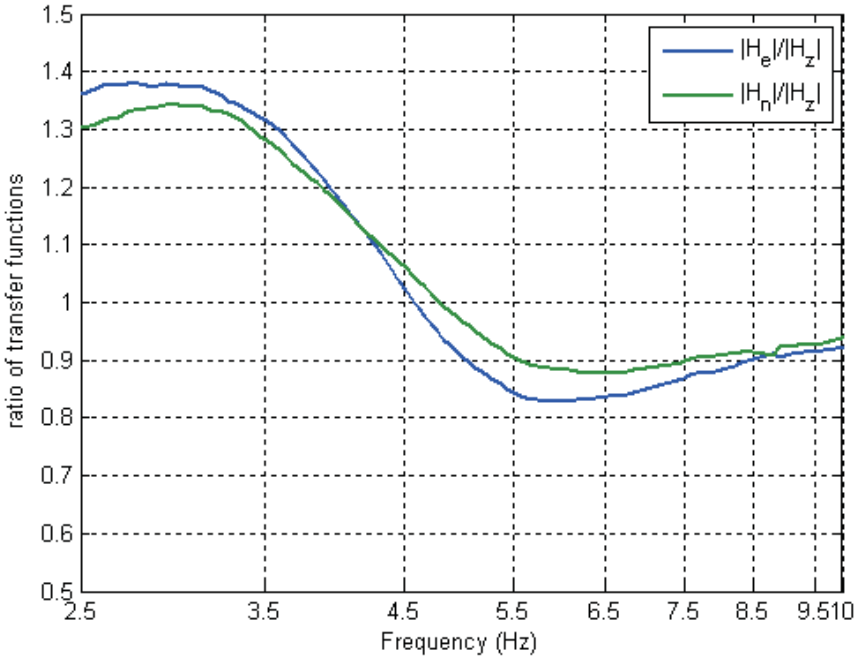

Figure 7. The ratio of the transfer functions of the TROMINO TR-19 seismological system computed using equation (26): the ratio of the transfer function of the E-W component and the vertical component (blue line) and the ratio of transfer function of the N-S component and the vertical component (green line). Below 3 Hz, the self-noise of the Tromino TR-19 affects the calculation and below this frequency, the ratio of the transfer functions cannot be calculated in this particular case.

of information and any interpretation, concerns the reliability of the HVSR curve." The basic presumption is that the HVSR curves obtained using different seismological systems at the same time and at a same place, need to be equal or at least very similar. In this study we presented two important sources in seismological systems that can cause insurrections in the HVSR curves and therefore an incorrect interpretation. The first source of error is the self-noise of an instrument that needs to be negligibly small. The second source of error is the use of non-calibrated instruments or if the transfer function is not considered in the HVSR calculations. In our paper a simple algorithm is presented that enables the reliability of the instruments used in the HVSR measurements using two broadband seismometers with better quality than tested systems as references units.

In order to maintain the integrity of the recorded data, the seismograph systems need to be periodically verified. This verification is important to ensure that the instrument is performing as it was designed to, and that it measures accurately the true ground vibration [24]. Although the seismographs are designed for use in a rugged environment, they are still sophisticated electronic monitoring devices. Therefore, preventative maintenance becomes an important part of the annual verification process [25]. A simple case to confirm these findings are instruments used in our test.

Using a non-calibrated instrument in measurements - without a correction for its transfer function - can cause unreliability in the estimated dynamic characteristics of a site and consequently of evaluated seismic microzonation.

Because of this, we have developed a straightforward method - using two reference seismometers – to evaluate the influence of the instrument's transfer function on the validity of the HVRS procedure, without any a-priori knowledge in terms of the transfer function of any of the systems.

REFERENCES

[1] Finn, W.D.L. (1991) Geotechnical Engineering Aspects of Microzonation, Proceedings of the Fourth International Conference on Seismic Zonation, 199-259., August 26-29, 1991.

[2] Tuladhar, R., Yamazaki, F., Warnitchai, P., Saita, J. (2004). Seismic Microzonation of the Greater Bangkok area using Microtremor Observations, Earthquake Engineering and Structural Dynamics 33, 211-225.

[3] Nogoshi, M., Igarashi, T. (1971). On the amplitude characteristics of microtremor (Part 2). Journal of the Seismological Society of Japan, 24, 26-40.

[4] Nakamura, Y. (1989). A method for dynamic characteristics estimation of subsurface using microtremor on the ground surface. Quarterly Reports of the Railway Technical Research Institute 30, 25-33.

[5] SESAME, (2004). Guidelines for the implementation of the H/V spectral ratio technique on ambient vibrations: measurements, processing and interpretation. http://sesame-fp5.obs.ujf-grenoble.fr/Papers/HV_User_Guidelines.pdf (last accessed 2010-09-14)

[6] Gosar, A. (2007). Microtremor HVSR study for assessing site effects in the Bovec basin (NW Slovenia) related to 1998 Mw5.6 and 2004 Mw5.2 earthquakes. Engineering Geology 91, 178–193.

[7] Mucciarelli, M., Gallipoli, M. (2001). A critical review of 10 years of microtremor HVSR technique. *Bollettino di Geofisica Teorica et Applicata* 42, 255-266.

[8] Molnar S., Cassidy J.F., Monahan P.A., Onur T., Ventura C., Rosenberger A. (2007). Earthquake Site Response Studies Using Microtremor Measurements in Southwestern British Columbia, Ninth Canadian Conference on Earthquake Engineering, *Proceedings of the 9th Canadian Conference on Earthquake Engineering*, 410-418., 26-29 June 2007.

[9] Bormann, P. Ed. (2002). *New Manual of Seismological Observatory Practice*. GFZ Potsdam, Germany.

[10] Wielandt E. (2004). Design Considerations for Broadband Seismometers. IRIS Advanced Broadband Seismometer Workshop, 24–26 March 2004 http://www.iris.edu/stations/seisWorkshop04/PDF/Wielandt-Design3.pdf (last accessed 2010-09-14)

[11] Güralp Systems Ltd. United Kingdom: www.guralp.com

[12] Holcomb, G. L. (1989). A direct method for calculating instrument noise levels in side-by-side seismometer evaluations. Open-file Report 89-214, U. S. Geological Survey.

[13] Pavlis G. L., Vernon F. L., (1994). Calibration of seismometers using ground noise. Bull. Seism. Soc Am. 84, 1243-1255.

[14] Guillier B., Atakan K., Chatelain J. L., Havskov J., Ohrnberger M., Cara F., Duval AM., Zacharopoulos S., Teves-Costa P. (2007). Influence of instruments on the H/V spectral ratios of ambient vibrations. Bulletin of Earthquake Engineering 6, 3-31.

[15] G. Streckeisen A.G, Switzerland

[16] Lennartz Electronic GmbH, Germany: http://www.lennartz-electronic.de/MamboV4.5.2/index.php (last accessed 2010-09-14).
[17] Micromed s.p.a, Italy: http://www.tromino.it (last accessed 2010-09-14).
[18] Lane D., Ragland W., Williams R., Penumadu D. (2008). Use of MASW for Geotechnical Site Characterization using Corrected Triaxial Geophones, EEGS' Annual Meeting Philadelphia, Pennsylvania. Proceedings of 21st Annual Symposium on the Application of Geophysics to Engineering and Environmental Problems, 1308-1315., April 6-10, 2008.
[19] Sleeman, R., van Wettum, A., Trampert J. (2006). Three-channel correlation analysis: A new technique to measure instrumental noise of digitizers and seismic sensors. Bull. Seism. Soc Am. 96, 258-271.
[20] http://sismic.iec.cat/orfeus/instrumentation/daqs_info_sheets/quanterra_q730.pdf (last accessed 2010-09-14).
[21] Earth Data, UK: http://www.earthdata.co.uk/pr6-24.html (last accessed 2010-09-14).
[22] Peterson, J. (1993). Observations and modelling of background seismic noise. Open-file report 93-322, U. S. Geological Survey, Albuquerque, New Mexico.
[23] http://www.TROMINO.it/noisecurves.htm, (last accessed 2010-09-14).
[24] Turnbull B., (2004). Seismograph calibration—what you should know, Pit & Quarry, Feb, 2004, http://www.pitandquarry.com/aggregate-equipment/drilling-blasting/seismograph-calibration-%E2%80%93-what-you-should-know (last accessed 2010-09-14).
[25] Rodgers, P. W. (1992). Frequency limits for seismometers as determined from signal-to-noise ratios. Part 2. The feedback seismometer. Bull. Seism. Soc Am. 82, 1099-1123.

PILOTIRANI TEŽNOSTNI PODPORNI ZID: DEFORMACIJSKO-NAPETOSTNA ANALIZA

QUN CHEN, LI WAN, CHANGRONG HE IN ZIHUI LAI

o avtorjih

Qun Chen *
Sichuan University,
College of Hydraulic and Hydropower Engineering,
State Key Laboratory of Hydraulics and Mountain River Engineering
Chengdu 610065, Kitajska
E-pošta: chenqun@scu.edu.cn

Li Wan
Sichuan University,
College of Hydraulic and Hydropower Engineering,
State Key Laboratory of Hydraulics and Mountain River Engineering
Chengdu 610065, Kitajska
E-pošta: wanali0266@tom.com

Changrong He
Sichuan University,
College of Hydraulic and Hydropower Engineering,
State Key Laboratory of Hydraulics and Mountain River Engineering
Chengdu 610065, Kitajska
E-pošta: hechr@126.com

Zihui Lai
China Railway Eryuan Engineering Group Co. Ltd.,
Chengdu 610031, Kitajska
E-pošta: TEYLJ1@creegc.com

* vodilni avtor

izvleček

Pilotirani podporni zid predstavlja nov tip podpornih konstrukcij na železnicah na Kitajskem. V sedanji praksi projektiranja so podporni zid, greda in piloti obravnavani kot neodvisne komponente. Tako ni obravnavano vzajemno delovanje podpornega zidu, pilotov in grede ter ni popolnoma obravnavan vpliv zemljine ali hribine na konstrukcijo, kar predstavlja določene omejitve v veljavni metodi projektiranja. V članku je podana študija bočnih zemeljskih pritiskov na steno zidu, razporeditev napetosti ter sil v armaturi grede in pilotov, ki uporablja rezultate terenskih opazovanj in tridimenzionalnih analiz na osnovi končnih elementov. Rezultati simulacij se dobro ujemajo z rezultati terenskih meritev. Ti rezultati so pokazali, da so bile natezne napetosti zelo majhne in, da so bile napetosti v večina conah v gredi in pilotih natezne. Prav tako smo ugotovili, da so natezne napetosti ali sile v gredi in pilotu v tej študiji bile veliko manjše od nateznih napetosti dobljenih z veljavno metodo projektiranja. Razjasnili smo, da je veljavna metoda projektiranja za dimenzioniranje grede in pilotov zelo konzervativna in, da jo je potrebno optimizirati z obravnavanjem vpliva temelja na celotno konstrukcijo ter upoštevanjem interakcije vseh komponent, ki sestavljajo sistem.

ključne besede

pilotirani težnostni podporni zid, terenske meritve, metoda končnih elementov, napetost, mehanizem prenosa obtežbe

LOAD TRANSFER AND STRESS IN A PILED GRAVITY RETAINING WALL

QUN CHEN, LI WAN, CHANGRONG HE and ZIHUI LAI

About the authors

Qun Chen *
Sichuan University,
College of Hydraulic and Hydropower Engineering,
State Key Laboratory of Hydraulics and Mountain River Engineering
Chengdu 610065, China
E-mail: chenqun@scu.edu.cn

Li Wan
Sichuan University,
College of Hydraulic and Hydropower Engineering,
State Key Laboratory of Hydraulics and Mountain River Engineering
Chengdu 610065, China
E-mail: wanali0266@tom.com

Changrong He
Sichuan University,
College of Hydraulic and Hydropower Engineering,
State Key Laboratory of Hydraulics and Mountain River Engineering
Chengdu 610065, China
E-mail: hechr@126.com

Zihui Lai
China Railway Eryuan Engineering Group Co. Ltd.,
Chengdu 610031, China
E-mail: TEYLJ1@creegc.com

* Corresponding author

Abstract

The piled retaining wall is a new type of railway retaining structure in China. In the current design, the retaining wall, the beam and the piles are assumed to be independent components. Both the mutual action of the retaining wall, the piles and beam, and the influence of the soil or rock foundation on the structure are not fully considered, so that there are some limitations in the current design method. In this paper, using field observations and a three-dimensional finite-element analysis, the lateral earth pressure on the wall back, the stress distributions and the forces of the reinforcements in the beam and the pile were studied. The simulation results were in good agreement with the field observation data. These results revealed that the tensile stresses were very small and that these stresses were positive in most zones in the beam and the pile. It can also be observed that the tensile stresses or forces in the beam and pile obtained in this study were much smaller than those obtained using the current design method. This clarified the fact that the current design method used for the beam and the pile was very conservative and that it should be optimized to consider the effect of the foundation on the whole structure and the interactions among the different components.

Keywords

piled gravity retaining wall, field observation, finite-element analysis, stress, load transfer mechanism

1 INTRODUCTION

Assuming that the bearing capacity of the foundation is insufficient, the pile foundation can be used to reduce the impact of the construction of a new railway on the already-existing railway and to guarantee the stability of the foundation. For this reason the piled retaining wall has been widely used in railway sub-grade engineering in recent years in China. However, a simple structural mechanics method is used in the design of the retaining structures. The retaining wall, the beam and the piles are considered as independent components, and both the mutual effect of the retaining wall, the piles and the beam, and the influence of the soil or rock foundation on the structure are not fully considered in the current design method, which is not in accordance with the facts. With the widespread use of this new type of retaining structure, it is necessary to systematically study the stress, deformation and load-transfer mechanism of all the components of the piled retaining wall to provide a theoretical basis for the design.

Usually, the piled retaining wall is composed of a retaining wall, a capping beam and some piles. The capping beam is a load-transfer component between the wall and the piles. This structure can be divided into two types: the piled gravity and the piled weighing retaining wall, according to the type of retaining wall. The former is the

common gravity wall, while the latter has a weighing platform at the back of the wall. Generally, the retaining wall is made of concrete, and the beam and the pile are made of reinforced concrete (RC).

The piled retaining wall has not been reported in countries other than China. In recent years, some researchers in China have studied the load transfer and the design method of the piled retaining wall. The mechanical characteristics and load-transfer mechanism of the piled weighing retaining wall were studied using a numerical method [1]. The mechanical principle of the piled weighing retaining wall was also investigated through a physical model test [2]. A modified design method for the piled retaining wall was proposed, based on research on a load applied to the structure [3].

The research results mentioned above have touched upon the interaction among the piles, the beam and the retaining wall, and the load-transfer mechanism of the structure. They also introduced some simplified calculation methods, which can be used for the design as references. However, most of them just focused on the piled weighing retaining wall. The mechanical characteristics of the piled gravity retaining wall were seldom reported. Moreover, so far, there is no report about a field study that can be used to verify the results obtained by a numerical simulation or a physical model test. In this paper, field observations and a three-dimensional finite element analysis were used to study the lateral earth pressure on the wall back, the stress distributions and the forces of the reinforcements in the beam and the pile. The results obtained in this work were also compared with those using the current design method. Some valuable advice is presented to support the design of piled retaining walls in the future.

2 PROJECT CONDITIONS AND INSTRUMENTATION

The piled gravity retaining wall studied in this paper is located at the station DK242+113 to DK242+155 on the double line railway, with a speed of 200 km/h, from Dazhou to Chengdu city in the Sichuan Province of China. The wall is 42 m long and its maximum height is 10 m. The surface layer of the foundation is silty clay, 1 m to 10 m thick, under which there are soft mudstones with a little sandstone. The ground surface is inclined and the foundation would not be stable if a common gravity retaining wall was used; therefore, a piled gravity retaining wall was used to ensure the stability of the foundation of the railway.

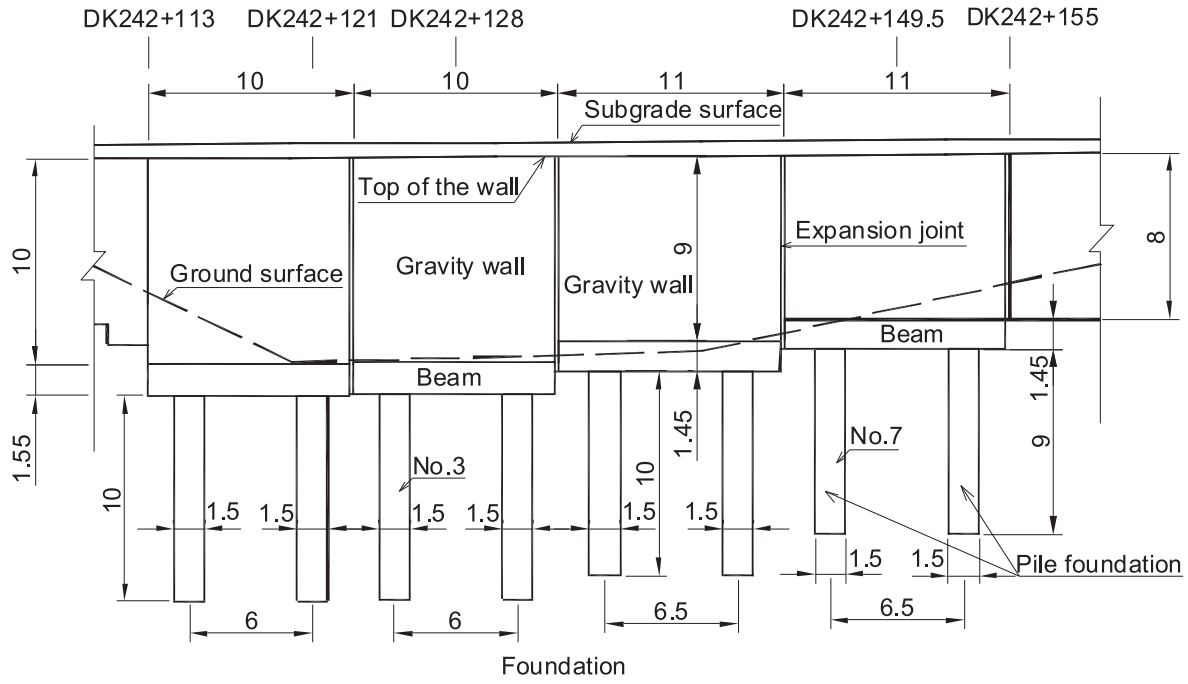

Figure 1. Front view of the piled gravity retaining wall (all units in meters).

The piled gravity retaining wall consists of four wall segments. They are two segments that are 10 m high and 10 m long, one segment that is 9 m high and 11 m long, and one segment that is 8 m high and 11 m long. The dimensions of the beam of the wall segment that is 10 m high are 10 m, 4.6 m and 1.55 m for length, width and thickness, respectively. Accordingly, they are 11 m, 4.0 m and 1.45 m for both wall segments that are 9 m and 8 m high. The dimensions of the piles of the 10 m and 9 m high wall segments are 10×2.25×1.5 m (length×width×thickness) and those of the 8 m high wall segment are 9×2.0×1.5 m. The front view and the cross-sectional geometry at the station DK242+121 of the wall are shown in Fig. 1 and Fig. 2, respectively. The backfill soil is compacted silty clay with some mudrock debris.

In order to study the stresses or forces on the structure, the lateral pressures on the back of the retaining wall and the stresses at the interface between the wall and the beam, two typical wall segments were chosen for the instrumentation. One is the wall segment that is 10 m high and the other is the wall segment that is 8 m high. The central cross-sections (station DK242+128 and station DK242+149.5 shown in Fig. 1) are chosen to install the earth pressure cells. The piles No. 3 and No. 7 (in Fig. 1) are chosen to install the reinforcement gauges. Due to space restrictions, only the results of the former wall segment (10 m high) will be presented and discussed.

Ten vibrating-wire earth pressure cells with a vertical spacing of 1 m were mounted on the wall back to measure the lateral earth pressure (shown in Fig. 3). The upmost earth pressure cell was located 0.5 m away from the top of the wall.

In order to monitor the stress distribution at the interface between the wall and the beam, ten rosettes of vibrating-wire strain gauges were installed at the interface. There were four strain gauges in each strain rosette to measure the strains along the directions of 0˚, 45˚, 90˚ and 135˚ at the same point. The strains in one half of the beam were measured because of their symmetrical distribution to the span center line in the beam. The arrangement and the orientation of the strain gauges in each strain rosette are shown in Fig. 4.

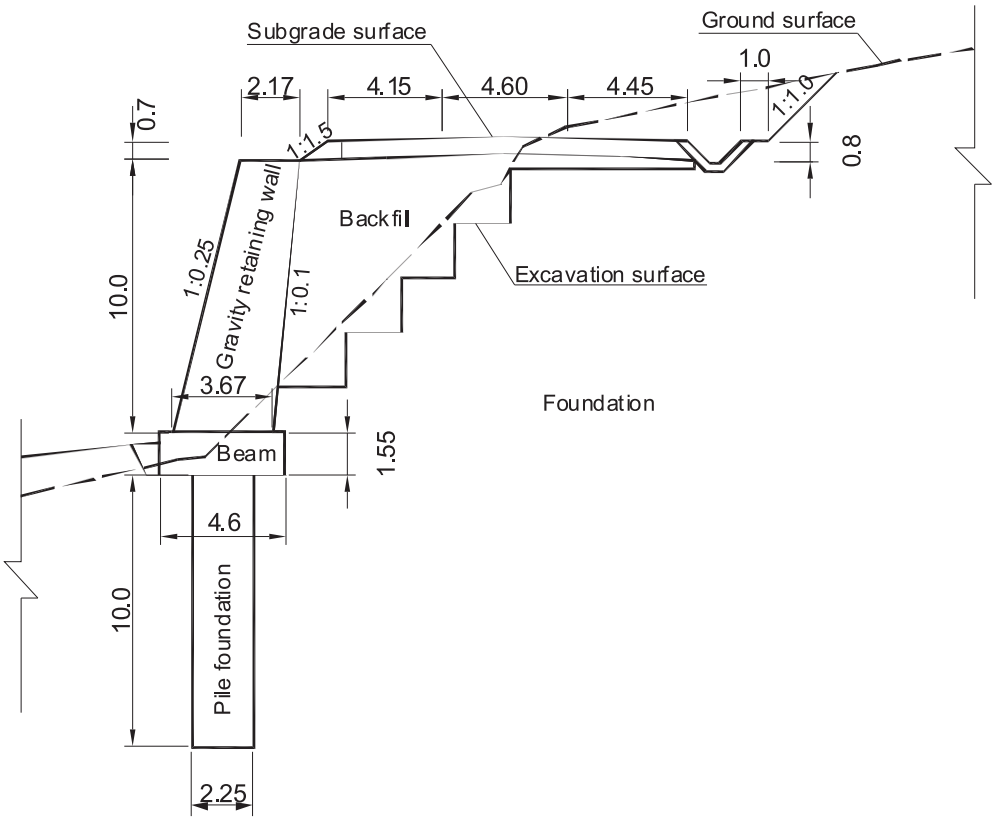

Figure 2. Cross-sectional geometry of the piled gravity retaining wall at station DK242+121 (all units in meters).

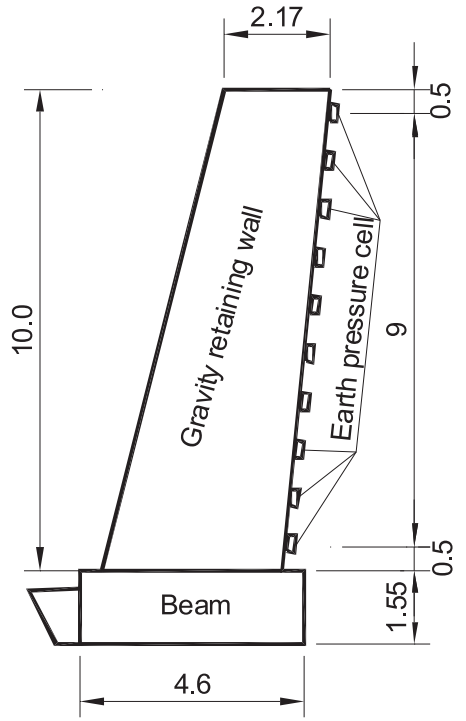

Figure 3. Arrangement of the earth pressure cells on the wall back (all units in meters).

The beam can be considered as a plane strain member, so that its longitudinal (x axis) strain can be ignored. When the strain direction of 0° aligns with that of the y axis, the normal strains in the four degree directions and the strain components in Cartesian coordinates have the following relations [4]:

$$\begin{aligned} &\varepsilon_y = \varepsilon_0 \\ &\varepsilon_z = \varepsilon_{90} \\ &\gamma_{yz} = \varepsilon_0 + \varepsilon_{90} - 2\varepsilon_{45} \quad or \quad \gamma_{yz} = 2\varepsilon_{135} - (\varepsilon_0 + \varepsilon_{90}) \end{aligned} \tag{1}$$

where ε_0, ε_{45}, ε_{90} and ε_{135} are the measured normal strains in four degree directions in one strain rosette, as shown in Fig. 4(b); ε_y and ε_z are the normal strains in the y and z directions respectively; and γ_{yz} is the shear strain in the z direction on the Y plane. According to the generalized Hooke's law [4], the horizontal and vertical normal stresses and the shear stress can be calculated by:

$$\begin{cases} \sigma_y = \dfrac{E[(1-\mu)\varepsilon_0 + \mu\varepsilon_{90}]}{(1+\mu)(1-2\mu)} \\ \sigma_z = \dfrac{E[(1-\mu)\varepsilon_{90} + \mu\varepsilon_0]}{(1+\mu)(1-2\mu)} \\ \tau_{yz} = \dfrac{E(\varepsilon_0 + \varepsilon_{90} - 2\varepsilon_{45})}{2(1+\mu)} \text{ or } \tau_{yz} = \dfrac{E(2\varepsilon_{135} - \varepsilon_0 - \varepsilon_{90})}{2(1+\mu)} \end{cases} \tag{2}$$

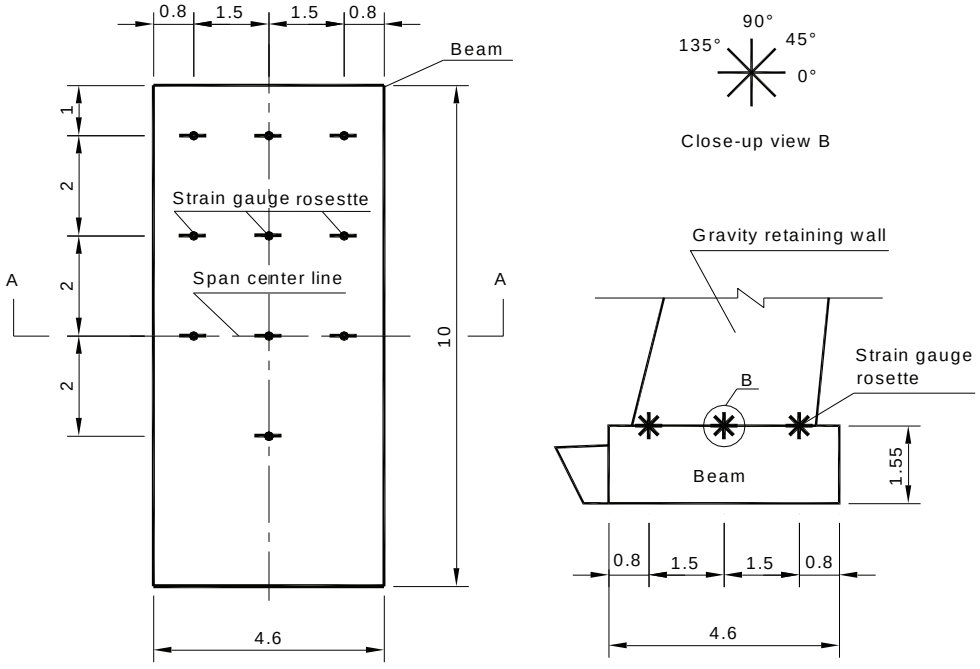

a) Horizontal section b) Section A-A

Figure 4. Arrangement of the strain gauges at the interface between the wall and the beam (all length units in meters).

where E and μ are the elastic modulus and the Poisson's ratio of the material, respectively; σ_y and σ_z are the normal stresses in the y and z directions respectively; and τ_{yz} is the shear stress in the z direction on the Y plane. For the commonly used 45° strain rosette, the 0°, 45° and 90° strains are required to deduce the normal stresses and the shear stress. The 135° strain gauge is normally used for the proof measurement.

In order to investigate the forces of the reinforcements in the beam and the pile, many reinforcement gauges were welded to the reinforcement at the selected location. On the top of the beam, fifteen reinforcement gauges were welded to three reinforcements. Five reinforcement gauges with a spacing of 1.1 m were arranged in each reinforcement bar. The quantity and the arrangement of the reinforcement gauges at the bottom were the same as that on the top of the beam, as shown in Fig 5(a). In total, sixteen reinforcement gauges were welded to two reinforcements in the vertical center section of the pile: half were at the front side and the other half were at the back side, as shown in Fig 5(b).

Prior to the in-situ installation, all the earth pressure cells, strain gauges and reinforcement gauges were calibrated indoors and their original readings were recorded. The pressure, strain and the force can be computed using the calibrating coefficient and the frequency reading.

3 THREE-DIMENSIONAL FINITE-ELEMENT ANALYSIS

The three-dimensional finite-element software ADINA 8.4 [5] was used in this study to simulate the construction of the piled gravity retaining wall. ADINA is popular finite-element software and has been under development for more than thirty years. The use of ADINA for soil-structure interaction problems was described by Sumino et al. [6] and Chen & Krauthammer [7]. The software has also been used for an analysis of the axial pile capacity [8] and the stress transfer between the pile and the soil [9].

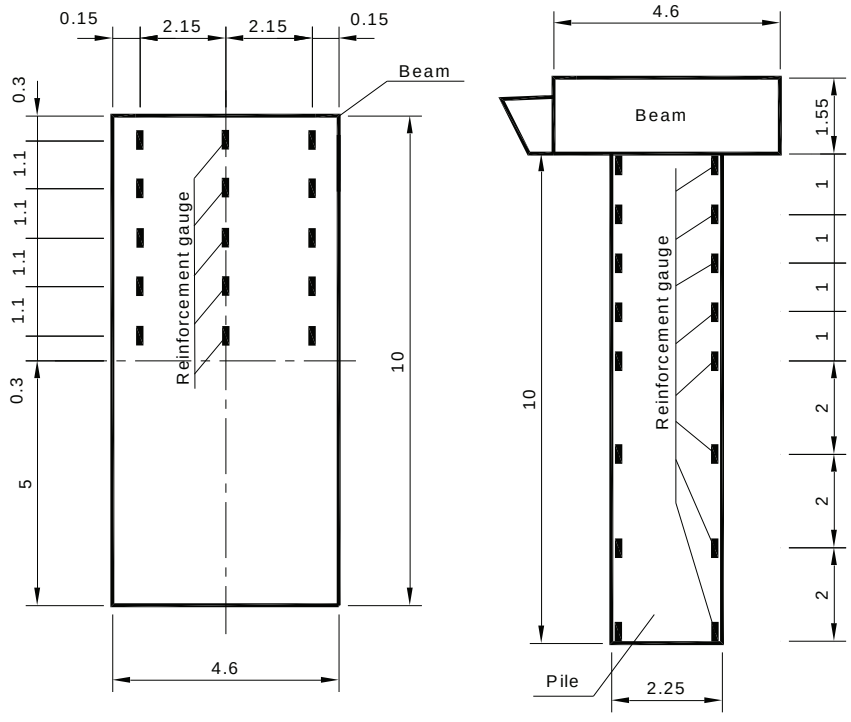

a) Horizontal section of the top or the bottom of the beam

b) Vertical center section of the pile

Figure 5. Arrangement of the reinforcement gauges on the top and at the bottom of the beam and the vertical center section of the pile (all units in meters).

To compare the results of the field observation, the wall segment that is 10 m high and 10 m long was analyzed in this paper.

3.1 SIMPLIFICATION AND DISCRETION OF THE FINITE-ELEMENT MODEL

The simulation domain was 10 m long (wall segment length), 46 m wide and 37.7 m high, as shown in Fig. 6. The origin of the coordinate was at the center, on the top of the beam. The longitudinal direction is defined as the *x* axis; the widthwise direction is defined as the *y* axis and the positive direction points to the wall; the altitudinal direction is defined as the *z* axis, and the upward is positive.

The concrete wall, the RC beam and piles, the backfill soil, the foundation soil and the rock were simulated using solid elements. Interface elements were assigned to the interface between the wall back and the soils. The thin layer elements were assigned between the wall and the beam because there was a construction interface.

The whole simulation domain was meshed to 62856 elements with 39241 nodes using 8-node hexahedron and 4-node tetrahedron elements. Smaller elements were used for the backfill soil. The surface mesh of the simulation domain is shown in Fig. 6. The mesh of the gravity retaining wall, the beam and the piles is shown in Fig. 7. The whole foundation was composed of two parts: the upper (above the bottom of the beam) and the lower parts. They were silty clay and mudrock, respectively.

The longitudinal end vertical boundaries were fixed to prevent movements to the boundaries' normal direction (fixed in the *x* direction). The left-hand and right-hand vertical boundaries were fixed in the *x* and *y* directions. The base was pinned, to prevent any movements in all directions (as shown in Fig. 6).

3.2 MATERIAL PROPERTIES

The backfill soil, foundation soil and mudrock were modeled using the Mohr-Coulomb elastic-plastic model which is capable of accounting for the dilation of soils.

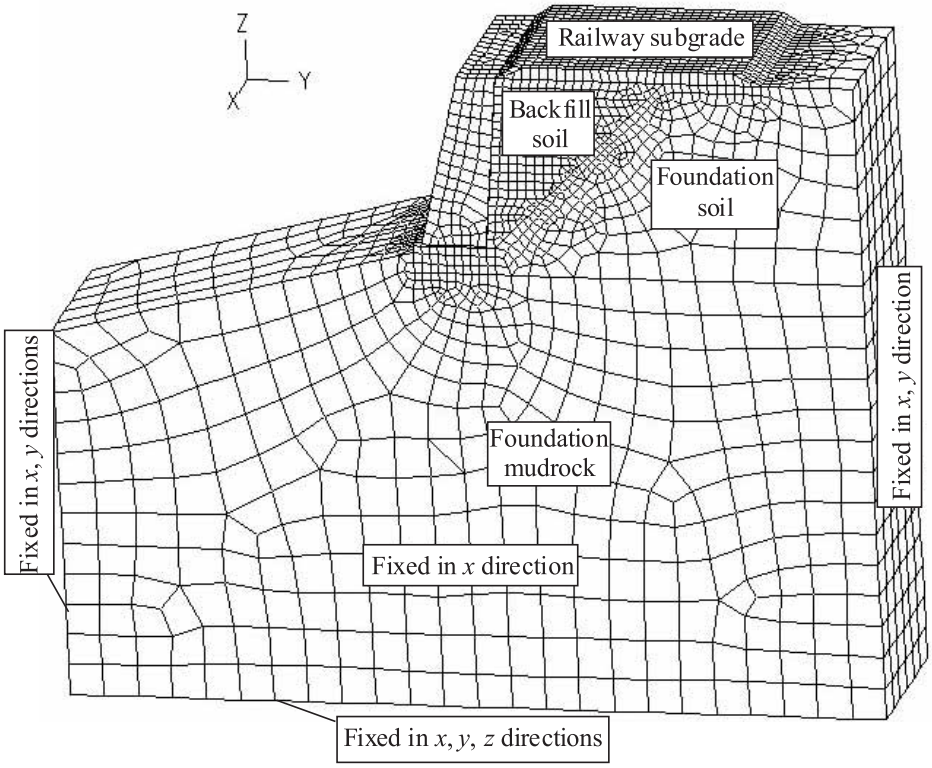

Figure 6. Surface mesh and boundary conditions of the simulation domain.

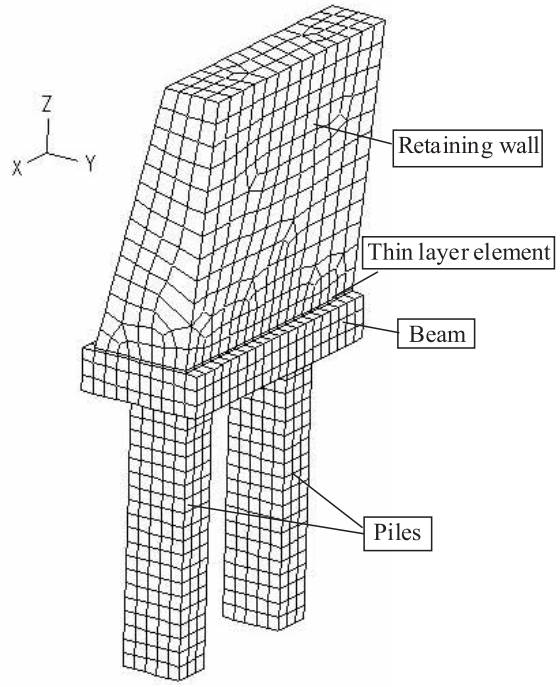

Figure 7. Surface meshes of the retaining wall, the beam and the piles.

The thin layer elements between the wall and the beam were also simulated using the Mohr-Coulomb model. Considering that the concrete wall and the RC beam and pile are much more rigid than the foundation and the backfill soil, all the structure components were assumed to be elastic material.

The property parameters of the RC and the concrete for the finite-element analysis were adopted according to the code GB50010-2002 [10]. The elastic constants of the thin layer element between the wall and the beam were the same as the concrete. Its strength parameters were referred to the shear strength parameters of the interface between the concrete layers in Table D3 in the design specification DL5108-1999 [11]. The constitutive model parameters of the soils and mudrock were obtained using a triaxial test. Their moduli and Poisson's ratios were obtained with a confined compression test and a uniaxial compression test. The frictional angle between the wall back and the soil was assumed to be half of the internal frictional angle of the backfill soil. All the material parameters used in the finite-element analysis are listed in Table 1.

3.3 MODELING OF THE CONSTRUCTION PROCEDURE

The construction procedure of the beam, the retaining wall and the embankment of the backfill soil were simulated using a finite-element analysis. The piles were considered as an already-existing structure for the foundation soil and rock because they were the bored cast-in-place piles and their construction had little impact on the stress and deformation of the foundation. Both the beam and the retaining wall were simulated as a single construction step. The filling of 1 m of backfill soil was modeled as a single placement step and the upper 0.7 m subgrade was modeled as a separate placement step.

As the groundwater table was lower than the base of the simulation domain and the backfill soil was compacted with lower water content than its optimal value, it was assumed that the pore-water pressures throughout the placement of the soil were zero at any stage. The initial vertical stresses in the backfill soil were computed by the gravity of the soil and the linear analysis. The horizontal stresses were calculated by the coefficient of the earth pressure at rest, which can be calculated using Poisson's ratio.

Table 1. Material parameters used in finite element analysis.

Parameters	Density	Modulus	Poisson's ratio	Cohesion	Internal friction angle	Dilation angle
Symbol	ρ	E	μ	c	φ	ψ
Unit	g/cm^3	MPa	-	kPa	°	°
Reinforcement concrete	2.4	3.1×10^4	0.2			
Concrete	2.3	2.2×10^4	0.2			
Thin layer element	2.3	2.2×10^4	0.2	500	26.6	0
Foundation mudrock	2.2	500	0.22	1200	24	10
Foundation soil	2.0	60	0.32	35	30	5
Backfill soil	1.9	40	0.35	35	28	3

4 RESULT ANALYSES AND DISCUSSION

The sign regulation of the ADINA is in accord with ordinary elastic mechanics. The tensile stress is positive and the compressive stress is negative. To facilitate the comparison of the numerical analysis results and the field observation data, the same coordinates were assigned to the field observation and analysis results.

4.1 PRESSURE ON THE WALL BACK

Fig. 8 shows the measured and computed pressures on the wall back. The pressures on the wall back increase with the progressive filling of the backfill soil and the pressure distributions along the height of the wall almost maintain the same mode during backfilling. The computed pressure distributions along the height of the wall are similar to the measured ones, although the pressure values obtained with the finite-element analysis are larger than the measured results. Both the measured and computed pressures increase gradually from upside to downside and decrease at the bottom of the wall back.

It is reasonable that the computed horizontal earth pressures are smaller than those of the dry-stone retaining wall obtained by Harkness et al. [12] because the cohesion of the backfill soil was considered in this analysis. The measured earth pressures are smaller than the computed ones; however, in the meanwhile, the measured stress changes at the base of the wall contributed by the placement of the backfill are a little larger than the computed ones. All of these indicate that the earth pressures are under-measured. The reason may be due to a system error of the pressure cells. It is also possible that the pressure cells are not closely contacted with the compacted backfill as the backfill near the wall back cannot be compacted by the machine effectively, the result of which is that it is relatively loose.

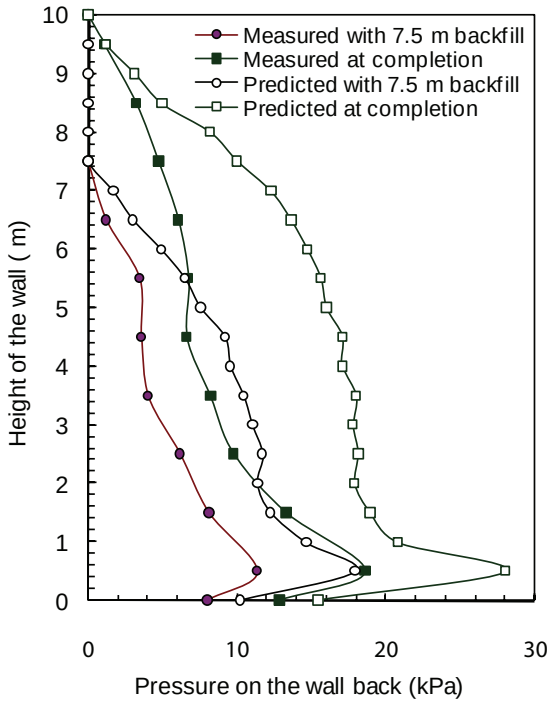

Figure 8. Measured and computed pressures on the wall back.

4.2 SHEAR STRESS BETWEEN THE WALL AND THE BEAM

The shear stress in the y direction at the interface between the wall and the beam can reflect the transfer of the lateral earth pressure on the wall back to the beam. The measured and computed shear stress distributions along the width direction of the beam at the interface between the wall and the beam at different construction stages are given in Fig. 9. A negative shear stress means the direction of the stress is towards the front of the wall. Both the measured and computed shear stresses are negative and they have similar distributions along the width direction of the beam, although the computed values are smaller than the measured ones. In different cross-sections, the shear-stress distributions represent a similar regulation. At the center of the width ($y = 0$), the magnitudes of the shear stresses are smaller than that at both sides of the beam. In the span center section ($x = 0$, Fig. 9(a)), the measured shear stresses and computed ones are a little larger at the front side than those at the back side. In the other sections (Fig. 9(b) and (c)), both the measured and computed shear stresses are smaller at the front side than those at the back side. They increase with the increasing height of the backfill soil. This is because the horizontal pressures on the back of the wall increase with the increase in the backfilling.

4.3 STRESSES OR FORCES IN THE BEAM

There is no strain gauge to measure the normal stress in the x direction in the beam, but the reinforcement gauge can measure the axial force of the reinforcement along the x direction. Fig. 10 illustrates the measured axial force distributions along the reinforcement and computed normal stress distributions in the x direction along the length direction on the top of the beam at different construction stages. Except for the computed

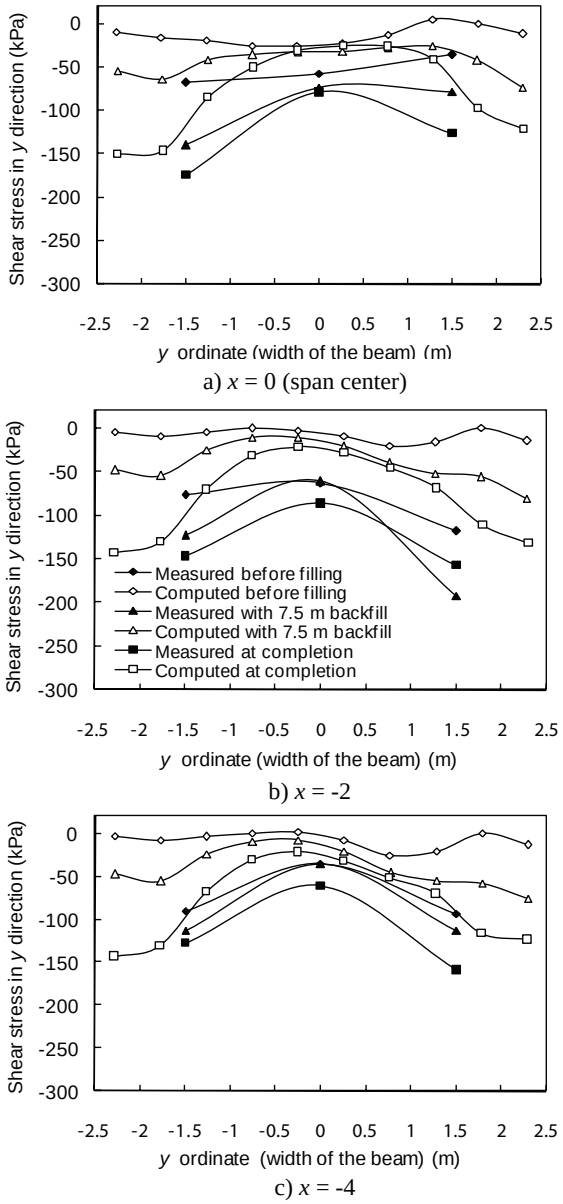

Figure 9. Measured and computed shear stresses in the *y* direction at the interface between the wall and the beam.

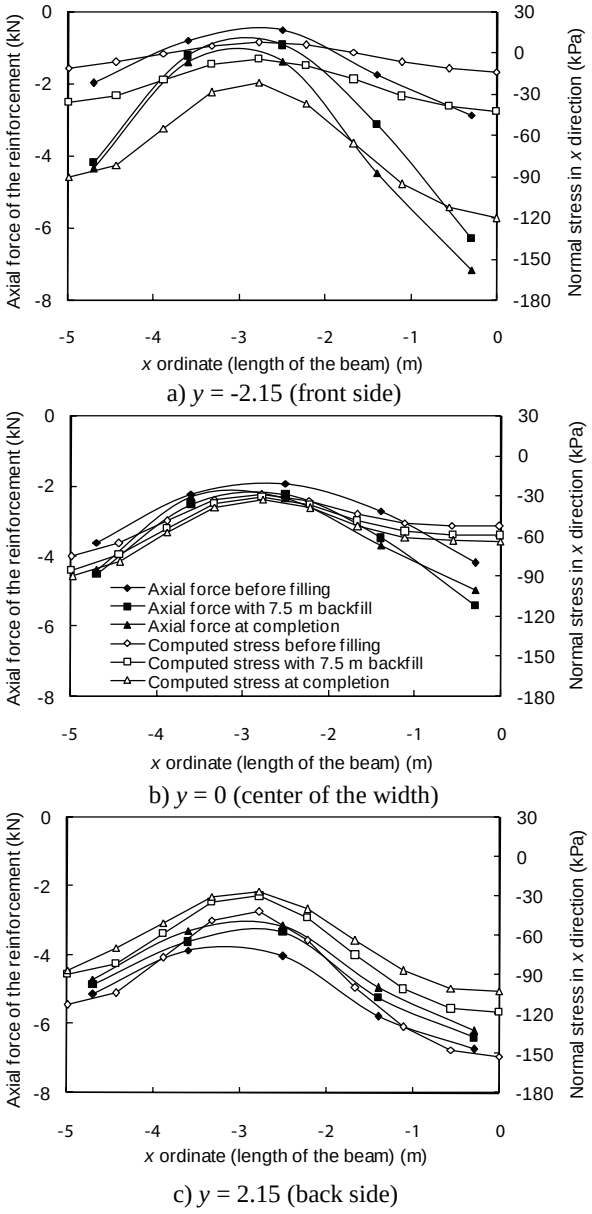

Figure 10. Measured axial forces of the reinforcements and computed normal stresses in the *x* direction on the top of the beam

stresses at the corresponding location of the pile top before filling, the forces and the stresses are both negative at different construction stages. This indicates that there is no tensile stress in the *x* direction as the top of the beam is compressed. Therefore, there is no need to use reinforcement for bearing the tensile forces. In the different longitudinal sections the stresses and the forces are similarly distributed along the length of the beam. They are the smallest at the corresponding location of the top center of the pile and become larger at the span center and the end of the beam, which is due to the underpinning effect of the pile on the beam. Although the underpinning effect results in tensile stresses in the beam, the top of the beam is still compressive due to the counter effect of the foundation mudrock, which weakens the moment effect.

Both the measured forces and the computed stresses increase with the increase in the height of the backfill soil at the front side and the center of the beam. However, they decrease with progressive backfilling at the back side of the beam. This is because the lateral earth pressure on

the wall back increases with the increase in the height of the backfill soil and makes the vertical compressive concentration zone, induced by the underpinning of the pile on the top of the beam, move from the back to the front side gradually with the construction process.

Fig. 11 shows the measured and computed normal stress distributions in the *y* direction along the width direction on the top of the beam at different stages of construction. The computed and measured stresses have similar distributions on the top of the beam, although the computed stresses are a little smaller than the measured ones at most locations. The stresses are negative in most zones and their distributions are similar in the different cross-sections. The stresses increase at the front and decrease at the back of the beam during the backfilling. Before placing the soil, the stresses are smaller in the front than those at the back. After filling the subgrade (at the completion), the stresses become larger in the front than those at the back. This is due to the increase in the lateral earth pressure, resulting in an increase of the normal stresses in the *y* direction in the beam.

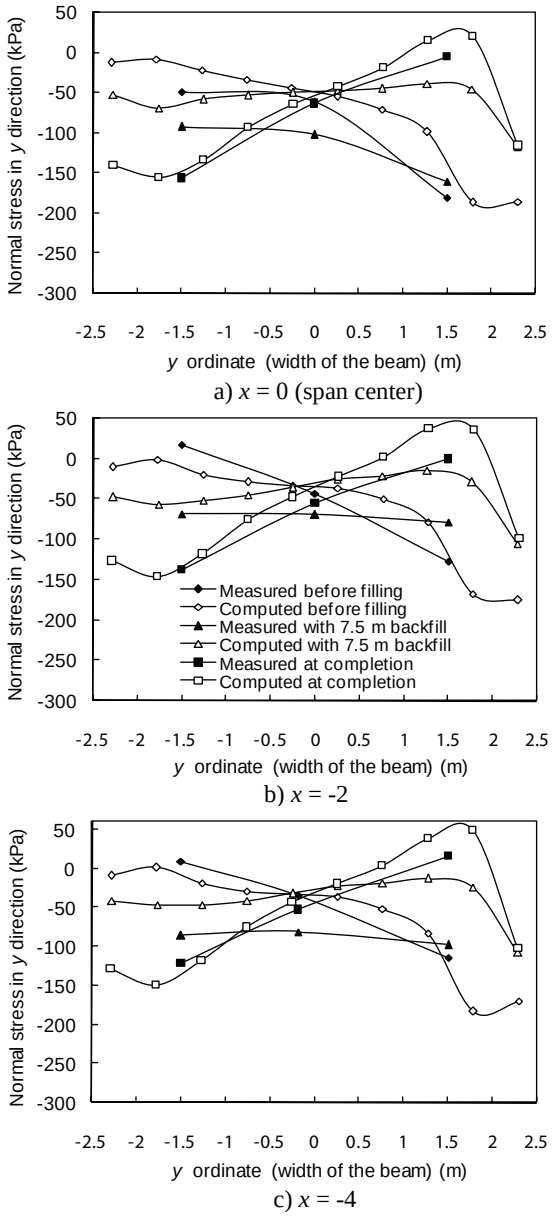

a) x = 0 (span center)

b) x = -2

c) x = -4

Figure 11. Measured and computed normal stresses in the *y* direction on the top of the beam.

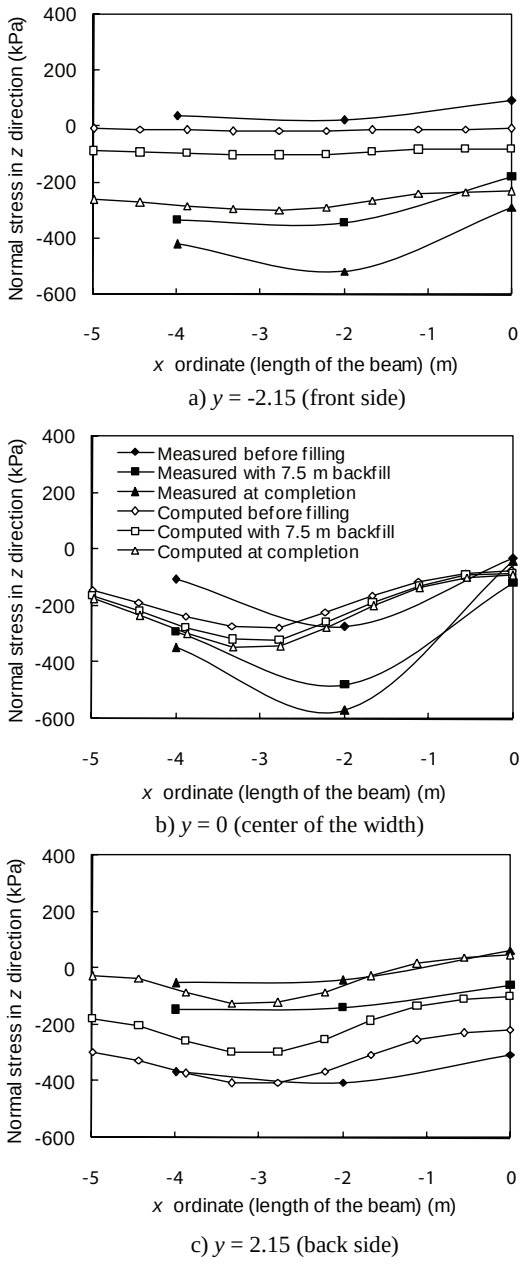

a) y = -2.15 (front side)

b) y = 0 (center of the width)

c) y = 2.15 (back side)

Figure 12. Measured and computed normal stresses in the *z* direction on the top of the beam.

The measured and computed normal stress distributions in the *z* direction along the length direction on the top of the beam at different construction stages are shown in Fig. 12. Although the computed and the measured stresses have a slight discrepancy, they show some common regulations. They are both negative in most zones and the beam is mostly compressed in the *z* direction. Except for the front side of the beam, the stresses are the maximum at the corresponding location of the top of the pile and then decrease to both sides. At the front side and the center of the beam (Fig. 12(a) and (b)), the stresses increase with the placement of the soil, while at the back side (Fig. 12(c)), the stresses decrease with the backfilling. This is because the increase in the lateral earth pressure with the backfilling makes the compressive concentration zone move from the back side to the front side on the top of the beam during backfilling.

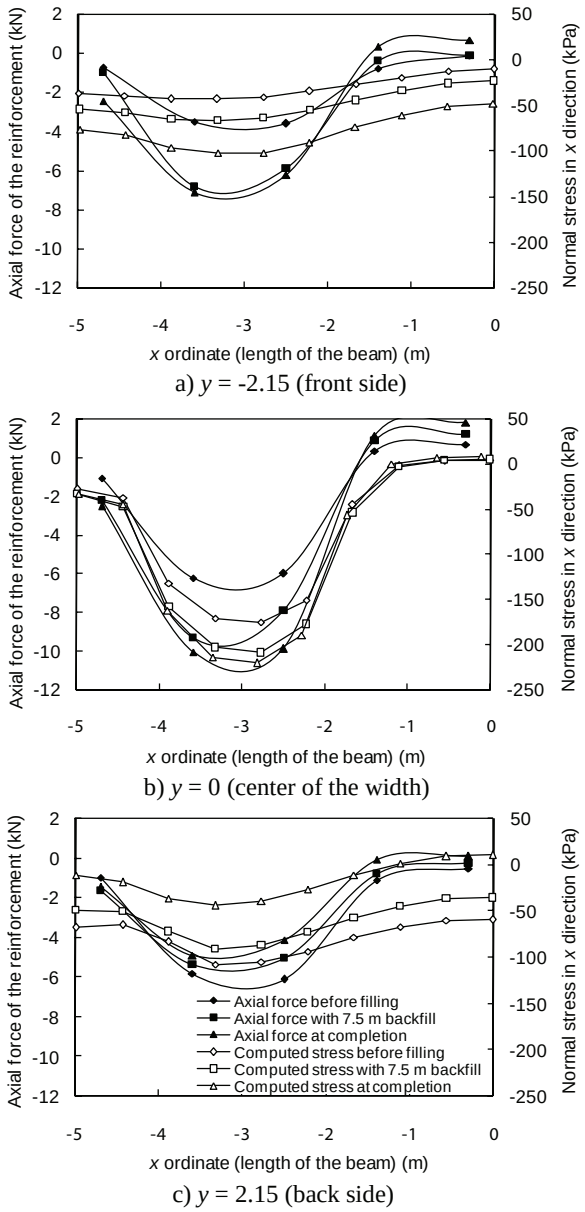

Figure 13. Measured axial forces of the reinforcements and the computed normal stresses in the *x* direction at the bottom of the beam.

Fig. 13 shows the measured axial force distributions along the reinforcements and the computed normal stress distributions in the *x* direction along the length direction at the bottom of the beam for different construction stages. Except for a small zone near the span center (x=0), the measured axial forces and the computed stresses are both negative in most zones. This indicates that most zones of the bottom of the beam are compressed. It is clear that because of the bearing effect of the foundation, the tensile stress caused by the moment at the span center is not large enough to counteract the compressive stress transferred from the top of the beam. The forces and the stresses have almost the same distribution regulations. They are the maximum at the corresponding location of the top center of the pile and decrease to both sides. At the front side and the center of the beam (Fig. 13(a) and (b)), the forces and stresses increase with the placement of the soil, while at the back side (Fig. 13(c)) they decrease with the backfilling.

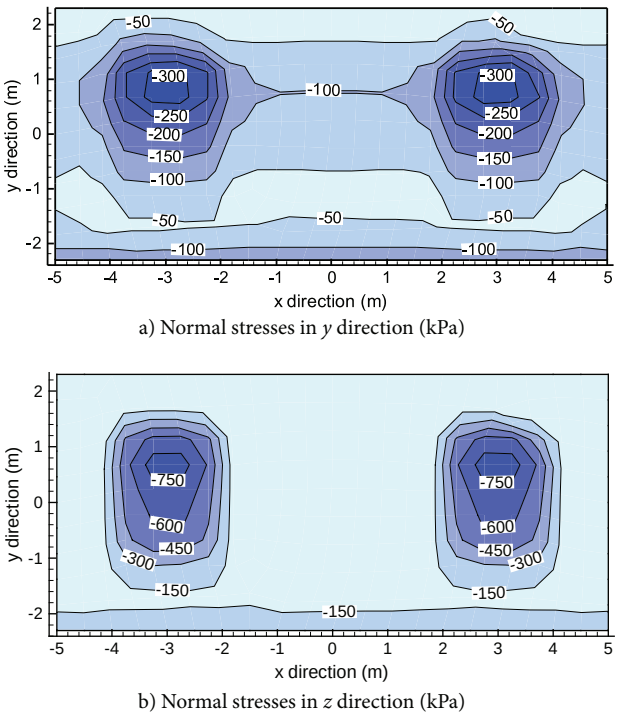

Figure 14. Contours of the normal stresses in the *y* and *z* directions at the bottom of the beam at the completion obtained with the finite-element analysis.

Due to there being no measured data available, the normal stresses in the *y* and *z* directions at the bottom of the beam are only represented by finite-element analysis results. Fig. 14 shows the contours of the normal stresses in the *y* and *z* directions at the completion. The stresses are all negative, which indicates that the bottom of the beam is compressed in both the *y* and *z* directions. There is a stress concentration zone at the location on the top of the pile, because the rigidity of the pile is higher than that of the mudrock foundation.

4.4 STRESSES OR FORCES IN THE PILE

The measured axial forces of the reinforcement and computed normal stresses in the *z* direction on the vertical center line at the front and the back sides of the pile are shown in Fig. 15. The forces and the stresses have similar distributions along the pile length. At the front side, the measured forces increase from the top to one-third of the pile length and decrease a little downwards to the end of the pile. The computed stresses increase from the top to the middle of the pile and then there is almost no change from the middle to the bottom. At the back side, the change of the forces along the pile length is small. The computed stresses have a small decrease from the top to the bottom of the pile. Because the weight of the backfill acts on the top of the beam and the foundation behind the wall, the back side of the beam has a settlement downwards; this results in an upward trend at the front side of the beam and tensile stress at the front side of the upper portion of the pile. Therefore, the compressive stresses or forces at the front side of the upper portion of the pile are smaller.

The horizontal load induced by the lateral earth pressure is transferred from the wall to the beam, and then to the top of the pile. The moment and the tensile stress will be induced in the pile if it is a member fixed at its bottom end and there is no restriction from the foundation. In contrast, the horizontal load is counteracted by the rock pressure on the side of the pile, because both sides of the pile are restricted by the foundation mudrock. So the pile is mainly compressed and has almost no tensile stress along its length.

With the placement of the backfill, both the measured forces and the computed stresses increase at the front side; nevertheless, the measured forces decrease at the

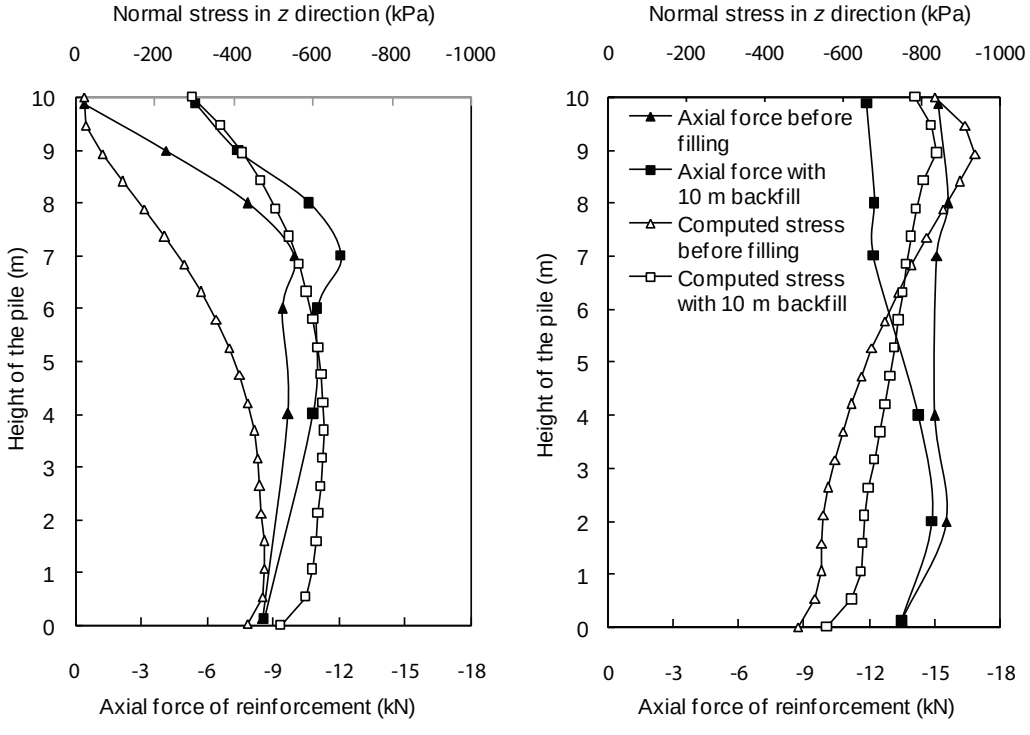

a) front side b) back side

Figure 15. Measured axial forces of the reinforcements and computed normal stresses in the *z* direction along the vertical center line of the front and back sides of the pile.

back side, and the computed forces decrease in the upper 3.2 m of the pile length and increase in the lower portion. This illustrates that the back side of the pile is unloaded and the front side of the pile is loaded because the increase of the lateral earth pressure with backfilling makes the pressure concentration zone on the top of the beam move from the back to the front side.

5 COMPARISON WITH THE DESIGN RESULTS

For the design of the beam and the pile of the piled retaining wall, the tensile stress is the control factor for the quantity of reinforcement. In the current design method, the structural and material mechanics method is used to calculate the internal forces and stresses in the beam and the pile. A beam with two piles is considered as a frame-beam structure and the piles are assumed to be elastic foundation beams. The restriction of the rock foundation is simplified as the spring and the effect of the soil foundation are ignored. The load acting on the beam is from the weight of the wall and the lateral earth pressure, which together with the weight of the beam is considered as the loads acting on the top of the pile. Therefore, the wall, the beam and the pile are considered as individual components to calculate their internal forces and stresses.

The total lateral earth pressure on the wall back, the maximum tensile stresses in the beam and the pile in the directions of their length obtained by design calculation (according to the design report [13]) and finite-element analysis are listed in Table 2. The total lateral earth pressure on the wall back obtained by the design calculation is larger than that obtained by the finite-element analysis. This is mainly because the cohesion of the soil is not considered in the design calculation for safety. The maximum tensile stresses in the beam and the pile obtained by the finite-element analysis are much smaller than those obtained by the design calculation. Ignoring the interaction among the structure components causes the stresses in the beam and the pile to be overestimated in the design. In fact, there is little tensile stress in the beam and the pile, so the reinforcements do not take effect of bearing tensile forces. The reinforcement quantity is too much according to the tensile stresses obtained by the design calculation. This indicates the current design method is too conservative and should be updated.

6 CONCLUSION

Field observations and the three-dimensional finite-element method are used to study the stresses or forces and the load-transfer mechanism during the construction of the piled retaining wall. The simultaneous representation and comparison of the measured and finite-element-computed results verify that the three-dimensional finite-element method can acurately estimate the stresses of the beam and the pile. The results obtained by the finite-element analysis are in good agreement with the measured results.

The pressures on the wall back increase with the filling of the backfill soil and the pressure distributions along the height of the wall almost maintain the same mode during backfilling. The lateral earth pressures obtained by the design calculation are larger than that obtained by a finite-element analysis and field measurement.

The shear stresses in the y direction at the interface between the wall and the beam are towards the front of the wall, which indicates in the horizontal earth pressure being transferred from the wall back to the beam. Along the length of the beam, the shear stresses are smaller in the center and larger at both sides along the width of the beam. The normal stresses in the three directions on the top of the beam are all compressive in most zones and the tensile stresses only represent in a small range and their magnitude is very small. Because of the underpinning of the pile, the normal stresses in the x direction on the top of the beam are smaller and the normal stresses in the z direction are larger at the corresponding location of the top of the pile. During the placement of

Table 2. Comparison of finite-element analysis and design-calculation results.

Obtained method	Total lateral earth pressure (kN/m)	Maximum tensile stress on the top of the beam (kPa)	Maximum tensile stress at the bottom of the beam (kPa)	Maximum tensile stress in the pile (kPa)
Finite element analysis	207.52	73.13	11.83	None
Design calculation	273.00	1180.29	602.63	1829.14

the soil, except for a small area near the span center, the normal stresses in three directions at the bottom of the beam are all compressive.

The horizontal load transferring from the beam to the pile was counteracted by rock pressure on the front side of the pile. Thus the pile is mainly compressed and has almost no tensile stress along its length.

The comparison of the results of the finite-element analysis and the design calculation shows that the design calculation overestimates the tensile stresses in the beam and the pile, which causes a large waste of the reinforcement. According to the field observation and the finite-element analysis results, there are small tensile stresses in the beam and the pile. Therefore, the current design method should be revised so as to consider the interaction among all the structure components and consider the foundation effect on the structure reasonably.

ACKNOWLEDGMENTS

This research is substantially supported by a grant from the National Science Youth Foundation of China (Approved No. 50709022) and by the Support Program for New Century Excellent Talent in China (Approved No. NCET-07-0569). The authors would also like to thank Mr. He Guomin for his assistance with the field instrumentation.

REFERENCES

[1] Qiao, C. L. (2004). Study on Action Mechanism of Piled Retaining Wall, Master Thesis, Sichuan University, Chengdu, China. (in Chinese).

[2] Gao, Z. H. (2005). Experimental Study and Numerical Analysis of Mechanical Behavior of Piled Retaining Wall Structure, Master Thesis, Sichuan University, Chengdu, China. (in Chinese).

[3] Zhang, M. (2007). Study on Designing Theory and Engineering Application of Piled Retaining Wall Structure, Master Thesis, Xinan Jiaotong University, Chengdu, China. (in Chinese).

[4] Muvdi, B. B., McNabb, J. W. (1980). Engineering Mechanics of Materials, Macmillan Publishing Co., New York, USA.

[5] ADINA R&D, Inc. (2006). ADINA User Interface Command Reference Manual Volume I: ADINA Solids & Structures Model Definition, Watertown, MA 02472, USA.

[6] Sumino, K., Noguchi, H., Hyodo, K., Sekimoto, H. (1985). Application of ADINA in analysis of a soil structure, Comput. Struct., Vol. 21 (1-2), 51-61.

[7] Chen, Y., Krauthammer, T. (1989). Combined ADINA-finite difference approach with substructuring for solving seismically induced nonlinear soil-structure interaction problems, Comput. Struct., Vol. 32 (3-4), 779-785.

[8] Lai, P., McVay, M., Bloomquist, D., Badri, D. (2008). Axial pile capacity of large diameter cylinder piles, From Research to Practice in Geotechnical Engineering, GSP 180, ASCE, 366-383.

[9] Nie, R-S., Leng, W-M., Yang, Q., Wei, W. (2009). Discussion on shear stress transfer between pile and soil, Rock and Soil Mechanics, Vol. 30 (3), 799-804. (in Chinese).

[10] The Construction Ministry of People's Republic of China. (2002). GB50010-2002 Code for Design of Concrete Structures, China Architecture and Building Press, China. (in Chinese).

[11] The China East Survey and Design Institute of State Electric Power Company. (1999). DL5108-1999 Design Specification for Concrete Gravity Dams, China Electric Power Press, China. (in Chinese).

[12] Harkness, R. M., Powrie, W., Zhang, X., Brady, K. C., O'Reilly, M. P. (2000). Numerical modelling of full-scale tests on drystone masonry retaining walls, Geotechnique, Vol. 50 (2), 165–179.

[13] China Railway Eryuan Engineering Group Co. Ltd. (2007). Design Report of the Double Line Railway with a Speed of 200 km/h from Dazhou to Chengdu City. (in Chinese).

UPORABA TEOREMA KORESPONDENČNIH STANJ PRI IZRAČUNU ZGORNJIH VREDNOSTI PASIVNIH ZEMELJSKIH TLAKOV

BORUT MACUH IN STANISLAV ŠKRABL

o avtorjih

Borut Macuh
Univerza v Mariboru,
Fakulteta za gradbeništvo
Smetanova ulica 17, 2000 Maribor, Slovenija
E-pošta: borut.macuh@uni-mb.si

Stanislav Škrabl
Univerza v Mariboru,
Fakulteta za gradbeništvo
Smetanova ulica 17, 2000 Maribor, Slovenija
E-pošta: stanislav.skrabl@uni-mb.si

izvleček

Rešitve nekaterih mejnih stanj (nosilnost temeljnih tal, aktivnih in pasivnih zemeljskih pritiskov itd.) za čiste-trenjske zemljine so za večji del praktičnih primerov enostavnejše v primerjavi z rešitvami enakih primerov za kohezijsko-trenjske zemljine. Teorem of Corresponding States nam v nekaterih primerih omogoča doseganje rešitev pripadajočih mejnih stanj za kohezijsko trenjske materiale s transformacijo že poznanih rešitev robnih elasto-plastičnih rešitev mejnih stanj za trenjske nekohezijske zemljine. Veljavnost oz. uporabnost osnovnega transformacijskega teorema (Caquot 1934) je omejena in velja le za enostavnejše primere mejnih stanj, kjer so napetostni vektorji pravokotni na robne površine ter kadar se pri transformaciji ohranjajo smeri trajektorij glavnih napetosti (Michalowski 2001). Pri aplikaciji kinematičnega pristopa mejne analize na osnovi teorema zgornje vrednosti je za primer določanja pasivnih zemeljskih pritiskov dokazano, da je za izbrani kinematični model tudi v splošnih primerih robnih napetosti dopustna posredna uporaba teorema korespondenčnih stanj v spremenjeni obliki. Rezultati opravljenih analiz pasivnih zemeljskih pritiskov kažejo, da je v splošnejših primerih nekritična uporaba teorema korespondenčnih stanj v osnovni obliki nedopustna, ker so dobljeni rezultati lahko pravilni le naključno ter v odvisnosti od robnih pogojev lahko pomenijo precenjene ali podcenjene vrednosti pasivnih zemeljskih pritiskov v geotehnični praksi.

ključne besede

korespondenčno stanje, zemeljski tlak, pasivni tlak, mejna analiza, zgornja vrednost

PASSIVE EARTH PRESSURE DETERMINATION: APPLICATION OF THE CORRESPONDING STATE THEOREM FOR CALCULATING UPPER-BOUND VALUES

BORUT MACUH and STANISLAV ŠKRABL

About the authors

Borut Macuh
Univerza v Mariboru,
Fakulteta za gradbeništvo
Smetanova ulica 17, 2000 Maribor, Slovenija
E-mail: borut.macuh@uni-mb.si

Stanislav Škrabl
Univerza v Mariboru,
Fakulteta za gradbeništvo
Smetanova ulica 17, 2000 Maribor, Slovenija
E-mail: stanislav.skrabl@uni-mb.si

Abstract

The validity of some limit state solutions, when strictly applied to the basic corresponding state theorem (Caquot, 1934), is limited and valid only for simpler limit states, where stress vectors are either perpendicular to the boundary surfaces or when the direction of stress eigenvalue trajectories in transformation are preserved (Michalowski, 2001). The theorem of corresponding states allows us, in some cases, to attain solutions belonging to the limit states for cohesive-friction materials with the transformation of the known boundary of elasto-plastic solutions of limit states for pure friction materials. We demonstrated that for the selected kinematically admissible model, in general cases of boundary stresses, the indirect application of the corresponding states theorem in modified form is permitted. To determine this, we applied the kinematic approach of limit state analysis and used the upper-bound theorem for determining passive earth pressures. The results of our analyses show that incautious application of the corresponding state theorem in its basic form and for general cases is inadmissible because the results obtained can be correct only coincidentally, depending on the boundary conditions.

Keywords

corresponding state, earth pressure, passive pressure, limit analysis, upper-bound

1 INTRODUCTION

The corresponding state theorem (Caquot, 1934) is based on the fact that for a considered boundary problem the stress state of cohesive-friction soils in a limit state is similar to the sum of the stress states of the same boundary problem for non-cohesive soils and hydrostatic pressure $p = c/\tan \phi$. The solutions of equal elasto-plastic boundary problems at limit states of cohesive-frictional and pure frictional material are undeniably similar. However, for more general and more complex boundary problems it is necessary to apply more exacting transformation relations to obtain solutions of limit states for cohesive-frictional materials, such as an inclined back fill or boundary conditions that require the transformation of limit state solutions for non-cohesive soils. The solutions of these limit states (bearing capacity of foundation ground, active and passive pressures, etc.) for pure friction soils are simpler for most practical examples compared with solutions of the same examples for cohesive-friction soils.

With the advancement of mathematical knowledge and numerical methods the practical significance of the corresponding state theorem has been reduced. However, it can frequently be found useful in the field of limit states, in investigating active and passive earth pressures and ground bearing capacities. Many authors, including Caquot (1934), Michalowski (2001) and Silvestri (2006), have suggested that there are limitations to applying the theorem in its basic form. In the past the corresponding state theorem was typically applied uncritically or unacceptably: Caquot and Kérisel (1948), Soubra and Regenass (2000), Škrabl and Macuh (2005), Vrecl-Kojc and Škrabl (2007) and many other authors.

The most practical use of the corresponding state theorem in limit state analysis using the upper-bound theorem most frequently occurs in three-dimensional cases where the transformation of known solutions compensate extensive integrations along individual discontinuity surfaces of deformation velocities. In the analyses of two-dimensional cases of limit-state analysis,

it is most successfully applied to control the results of mathematical analyses.

This article describes the procedure of determining the limit values of passive earth pressures for two-dimensional cases using the kinematic model of limit states with the upper-bound theorem. A comparison of several results of passive earth pressure coefficients, determined using the procedure of Kérisel and Absi (1990), shows that applying the corresponding state theorem, in its original form, to more general situations is not admissible.

2 KINEMATIC FAILURE MECHANISM

Figure 1 describes a general two-dimensional example of a rigid inclined wall having inclination α, height h with inclined backfill β. The kinematical failure mechanism comprises n triangular rigid blocks. As presented in Figure 1b, the kinematically admissible deformation velocities of individual blocks act in directions that enclose angle ϕ with individual discontinuity lines d_i (i=1,2,…n). The velocities of individual rigid blocks are uniformly defined by the condition that relative velocity directions between individual rigid blocks should enclose angle ϕ with lateral contact surfaces l_i (i=1,2,…n). The hodograph of individual rigid blocks is shown in Figure 1c.

The velocities of the whole failure mechanism can be uniformly determined from the chosen value of the deformation velocity of the first rigid block:

$$\dot{V}_1 = 1 \quad \dot{V}_{i+1} = \dot{V}_i \frac{\sin(\beta_{i,i+1} + \alpha_i)}{\sin(\beta_{i,i+1} + \alpha_{i+1})} \quad ,$$
$$\dot{V}_{i,i+1} = \dot{V}_i \frac{\sin(\alpha_{i+1} - \alpha_i)}{\sin(\beta_{i,i+1} + \alpha_{i+1})} \qquad (1)$$

The resultant value of passive earth pressures (P_p) is defined by equation two:

$$P_p = K_{p\gamma}\gamma\frac{h^2}{2} + K_{pc}ch + K_{pq}qh \qquad (2)$$

where $K_{p\gamma}$ denotes the coefficient of passive earth pressures due to soil self-weight, γ denotes the soil unit weight, K_{pc} denotes the coefficient of passive earth pressures due to cohesion (c) and K_{pq} is the coefficient of passive earth pressures due to the surcharge q. The passive pressure distribution along a wall height for a part that belongs to soil self-weight is triangular, while the part that belongs to cohesion and surcharge is rectangular or constant along the wall height.

This paper assumes that the backfill soil fulfills the Mohr-Coulomb yield criterion with the associative plastic flow rule (normality principle). The change of energy dissipation per volume unit of backfill soil can be evaluated by (Michalowski, 2001):

$$\dot{D} = -\dot{\varepsilon}_v c\cos\phi = -(\dot{\varepsilon}_1 + \dot{\varepsilon}_3)c\cot\phi \qquad (3)$$

where $\dot{\varepsilon}_1$ and $\dot{\varepsilon}_3$ denote major and minor eigenvalues of strain rate; $\dot{\varepsilon}_v$ rate of volumetric strain deformation, and c and ϕ represent the cohesion and angle of inner friction of backfill soil.

3 WORKING EQUATION

For soils that follow the associative flow rule, the change of inner energy dissipation is never lower than the change of work of outer forces for an arbitrary kinematically admissible failure mechanism (Fig. 1):

$$\int_V \dot{D}(\dot{\varepsilon}_{ij})dV = \frac{c}{\tan\phi}\left[\sin(\alpha_n - \beta)\frac{l}{\cos\beta}\dot{V}_n - \cos(\alpha + \alpha_1)\frac{h}{\cos\alpha}\dot{V}_1\right] \geq \gamma\frac{h^2}{2}K_{p\gamma}\left[\cos\delta\cos(\alpha_1 + \alpha) - \sin\delta\sin(\alpha_1 + \alpha)\right]\dot{V}_1 + chK_{pc}\left[\cos\delta\cos(\alpha_1 + \alpha) - \sin\delta\sin(\alpha_1 + \alpha)\right]\dot{V}_1 + qhK_{pq}\left[\cos\delta\cos(\alpha_1 + \alpha) - \sin\delta\sin(\alpha_1 + \alpha)\right]\dot{V}_1 - \sum_{i=1}^{n} G_i \sin\alpha_i \dot{V}_i - q\frac{l}{\cos\beta}\sin\alpha_n \dot{V}_n \qquad (4)$$

where V denotes the total volume of the failure mechanism. Provided that deformation velocity $\dot{V}_1 = 1$ and the generalized wall height h^* = 1 equation 4 leads to:

$$\frac{c^*}{\tan\phi}\left[\sin(\alpha_n - \beta)\frac{l^*}{\cos\beta}\dot{V}_n - \cos(\alpha + \alpha_1)\frac{1}{\cos\alpha}\right] \geq \frac{K_{p\gamma}}{2}\cos(\delta + \alpha_1 + \alpha) + c^* K_{pc}\cos(\delta + \alpha_1 + \alpha) + q^* K_{pq}\cos(\delta + \alpha_1 + \alpha) - \sum_{i=1}^{n} G_i^* \sin\alpha_i \dot{V}_i - q^*\frac{l^*}{\cos\beta}\sin\alpha_n \dot{V}_n \qquad (5)$$

where $c^* = \frac{c}{\gamma h}$ and $q^* = \frac{q}{\gamma h}$ denote normalized cohesion and normalized surcharge; $G_i^* = \frac{G_i}{\gamma h^2} = \gamma^* V_i^*$ and $l^* = \frac{l}{h}$ normalized weight of the individual triangular block of

backfill soil and the normalized length of the failure line (surface); $\gamma^* = 1$, $h^* = 1$ and V_i^* denote the generalized unit weight and unit height of the wall and the appurtenant volume of individual soil blocks.

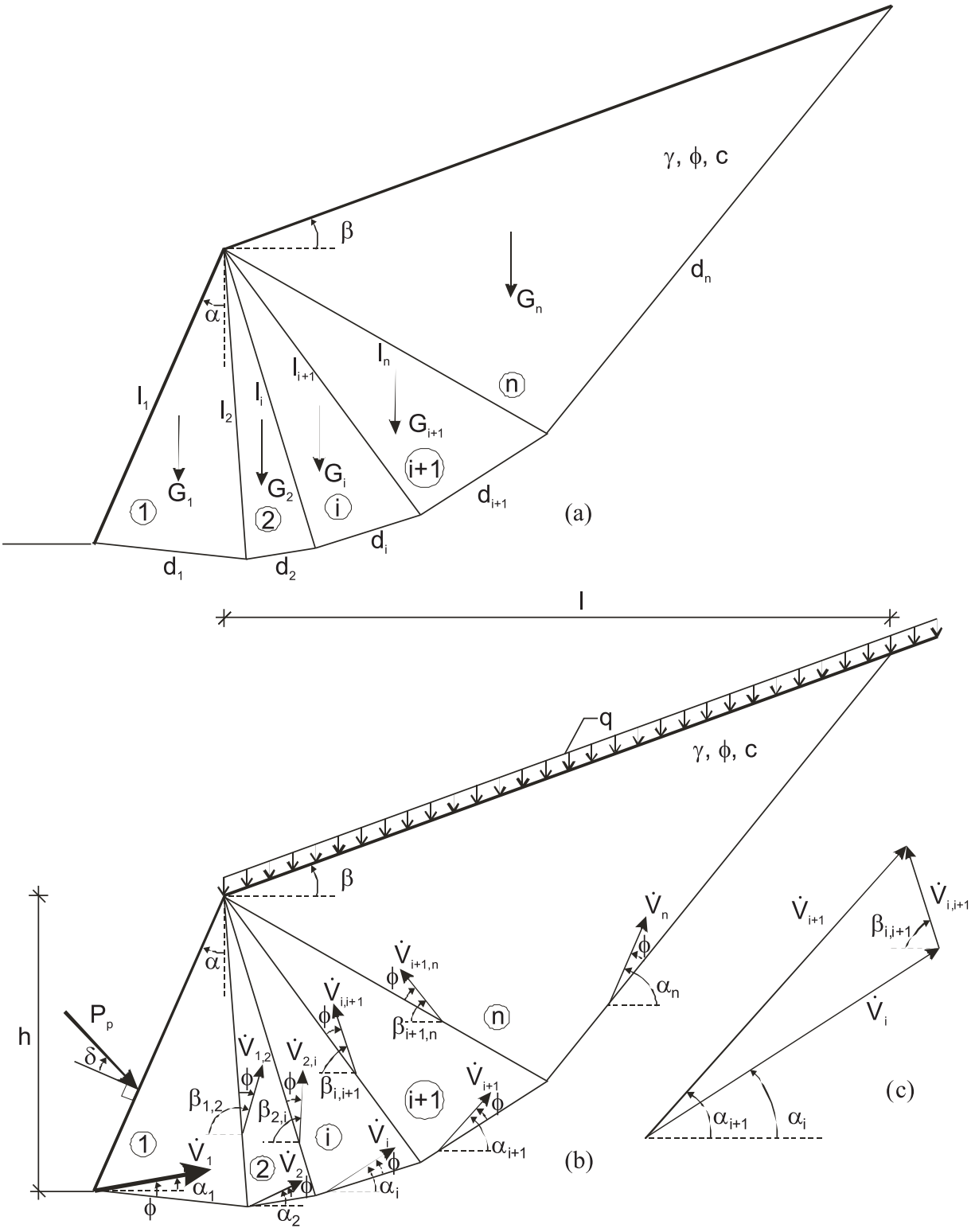

Figure 1. Translational failure mechanism; (a) geometry, (b) absolute and relative velocities of individual rigid blocks and (c) hodograph.

4 NUMERICAL ANALYSES AND RESULTS

The original failure mechanism is completely defined by n coordinates that define the individual blocks (Fig. 1). They have to be selected in a way that ensures that the original failure mechanism is kinematically admissible. In numerical analyses using the process of mathematical optimization, the critical kinematical admissible failure mechanism is obtained by minimizing equation 6:

$$f = \frac{K_{p\gamma}}{2} + c^* K_{pc} + q^* K_{pq} = \sum_{i=1}^{n} \frac{G_i^* \sin\alpha_i}{\cos(\delta + \alpha_1 + \alpha)} \dot{V}_i + \\ + q^* \frac{l^*}{\cos\beta \cos(\delta + \alpha_1 + \alpha)} \sin\alpha_n \dot{V}_n + \\ \frac{c^*}{\tan\phi} \left[\sin(\alpha_n - \beta) \frac{l^*}{\cos\beta \cos(\delta + \alpha_1 + \alpha)} \dot{V}_n - \right. \\ \left. \cos(\alpha + \alpha_1) \frac{1}{\cos\alpha \cos(\delta + \alpha_1 + \alpha)} \right] \tag{6}$$

Where f represents the objective function of the optimization problem. The coefficients of passive earth pressures are defined by equations 7, 8 and 9.

$$K_{p\gamma} = \frac{2}{\cos(\delta + \alpha_1 + \alpha)} \sum_{i=1}^{n} G_i^* \sin\alpha_i \dot{V}_i \tag{7}$$

$$K_{pq} = \frac{l^*}{\cos\beta \cos(\delta + \alpha_1 + \alpha)} \sin\alpha_n \dot{V}_n \tag{8}$$

$$K_{pc} = \frac{1}{\tan\phi \cos(\delta + \alpha_1 + \alpha)} \left[\sin(\alpha_n - \beta) \frac{l^*}{\cos\beta} \dot{V}_n - \right. \\ \left. \cos(\alpha + \alpha_1) \frac{1}{\cos\alpha} \right] \tag{9}$$

Using equation 8, the coefficient of passive earth pressures, due to cohesion, can be given in the following form:

$$K_{pc} = \frac{1}{\tan\phi} \left\{ K_{pq} \left(\cos\beta - \frac{\sin\beta}{\tan\alpha_n} \right) - \right. \\ \left. \frac{1}{\cos\alpha \left[\cos\delta - \tan(\alpha_1 + \alpha) \sin\delta \right]} \right\} \tag{10}$$

Equation 10 represents the transformation rule for determining the coefficient of passive earth pressures for cohesive-frictional soils K_{pc} from the known and, as a rule, easier solutions for pure friction soils K_{pq}. We can establish that equation 10 is valid only for the selected failure mechanism and differs from the original transformation theorem (Caquot, 1934) that is used for passive pressure states given in equation 11.

$$K_{pc} = \frac{1}{\tan\phi} \left[K_{pq} - \frac{1}{\cos\delta} \right] \tag{11}$$

A comparison of equations 10 and 11 shows that the original transformation of equation 11 is applicable only for the simplest cases of passive earth pressure on vertical walls. Such cases do not consider the friction between the wall, backfill soil and horizontal backfill.

We numerically analyzed the kinematical admissible failure mechanisms using n = 30 triangular soil blocks (Fig. 1).

Equation 6 shows that for different ratios of generalized unit weights of soil blocks γ^*, the surcharge intensities q^* and soil cohesions c^*, we were able to obtain different geometries of the critical failure mechanism through the process of mathematical optimization. This enabled us to determine the lowest total value of passive pressures P_p.

Table 1 represents a comparison of passive earth pressure with coefficients K_{pc} calculated using equations 9 and 10 with the original transformation in equation 11. This was done in accordance with the procedure of Kérisel and Absi (1990). In the procedure of mathematical optimization, we first analyzed the equal conditions $\gamma^* = c^* = 0$ and $q^* > 0$ that were considered in the method used by Kérisel and Absi (1990). For backfill soil analysis, we considered the inner friction angle $\phi = 35°$, $\delta = \phi/2$, $\alpha = 0$, and $\beta =$ 30° to 35° in increments of 5°.

Furthermore, we used the same set of coefficients of passive earth pressures and applied them to the cohesion for three different combinations of influences on soil unit weight, cohesion and surcharge (Table 1).

The calculations of coefficient K_{pc} using equations 9 and 10 give exactly the same results for all kinematical admissible failure mechanisms.

5 CONCLUSIONS

The results of our numerical analyses show that it is not admissible to determine the coefficient of passive earth pressures K_{pc} to cases of friction between wall and soil and inclined backfills when applying the original transformations according to the corresponding state theorem (Caquot, 1934). The results of the original transformations usage can indicate overestimated or underestimated values of passive earth pressures in geotechnical practice.

Table 1. Comparison of passive pressure coefficients K_{pq} and K_{pc} obtained with the results of calculations using the method of Kérisel and Absi (1990) for $\phi = 35°$, $\delta = \phi/2$ and $\alpha = 0$.

Backfill inclination	Kinematical model n=30			Kérisel and Absi		Kinematical model n=30		
	$\gamma^* = c^*$=0 and $q^* > 0$					γ^*=q^*=0 and c^*>0	c^*=q^*=0 and γ^*>0	c^*=q^*=0.2 and γ^*=1
β (°)	K_{pq} (8)	K_{pc} (11)	K_{pc} (9)	K_{pq}	K_{pc} (11)	K_{pc} (9)	K_{pc} (9)	K_{pc} (9)
-30	1.610	0.803	3.532	1.505	0.652	2.301	3.532	2.604
-25	2.153	1.577	3.376	2.092	1.490	2.764	3.371	2.975
-20	2.757	2.439	3.690	2.739	2.415	3.332	3.687	3.479
-15	3.474	3.464	4.255	3.448	3.427	4.038	4.222	4.125
-10	4.282	4.617	4.979	4.264	4.541	4.841	4.915	4.877
-5	5.179	5.898	5.824	5.155	5.864	5.747	5.786	5.760
0	6.167	7.310	6.824	6.116	7.237	6.769	6.839	6.791
5	7.246	8.851	7.985	7.220	8.814	7.920	8.203	7.986
10	8.412	10.516	9.338	8.368	10.454	9.221	9.630	9.375
15	9.657	12.294	10.923	9.615	12.235	10.688	11.413	10.986
20	10.962	14.158	12.801	10.929	14.112	12.346	13.605	12.853
25	12.298	16.067	15.068	12.270	16.025	14.215	16.277	15.053
30	13.620	17.956	17.955	13.605	17.933	16.331	19.736	17.594
35	14.823	19.673	21.829	14.706	19.505	18.718	23.489	20.556

We estimate that similar deviations and miscalculations will also appear in analyzing the limit states of ground bearing capacities for horizontally loaded shallow foundations, foundations near slopes and foundations with an inclined foundation base.

The largest deviations appeared in the limit states of passive earth pressures for inclined backfills, where the negative inclination approached the value of the soil's inner angle of friction. In such cases the coefficients of passive earth pressures, obtained from equation 11, are essentially lower from the actual deviations, which can reach up to 300% of the lowest values. The overestimated values of coefficient K_{pc} using the transformation expression (equation 11) also appear for horizontal backfills and backfills with a moderate inclination. The values come to 12% of the lowest value, determined according to the limit state method using the upper-bound theorem.

It is therefore false and unacceptable to calculate passive pressures for cohesive-friction material from solutions of pure friction material using the known procedure for calculating passive pressures described in Kérisel and Absi (1990). Slopes with decreasing inclinations are very frequent in geotechnical practice. They are characteristic of embedded regions of embedded retaining structures on slopes (pile walls, sheet pile walls etc.). Such situations require detailed and systematic approaches of passive earth pressure. The results of our analyses also show that different geometries of the failure mechanism are critical for determining the different influences of soil self-weight, cohesion and surcharge (Table 1). We obtained the lowest expected values of coefficients K_{pc} when analyzing $\gamma^* = q^* = 0$ and $c^* > 0$. In our opinion, these values are generally applicable because the passive pressure coefficients, in practice, are a bit higher due to the cohesion that occurs in practice.

The transformation expression (equation 11), first proposed by Caquot (1934) and uncritically used in the procedure of Kérisel and Absi (1990), is not generally applicable. It should be replaced with the expression defined by equation 10 for determining passive pressures with the limit state method using the upper-bound theorem. This procedure is also applicable to three-dimensional limit state analyses where similar failure mechanisms are in accordance with the upper-bound theorem.

REFERENCES

[1] Caquot A. (1934). Equilibre des massifs au frottement interne. Stabilite des terres pulverulents et coherents. *Gauthier-Villars*, Paris.

[2] Caquot A. and Kérisel J. (1948). Tables de poussée et de butée. *Gauthier-Villars*, Paris.

[3] Kérisel, J., and Absi, E. (1990). Tables for the calculation of passive pressure, active pressure and bearing capacity of foundations. *Gauthier-Villars*, Paris, France.

[4] Michalowski, R. L. (2001). Upper-bound load estimates on square and rectangular footings. *Géotechnique*, The Institution of Civil Engineering, London, England, 51(9), 787-798.

[5] Silvestri, V. (2006). Limitations of the theorem of corresponding states in active pressure problems. *Canadian Geotechnical Journal*, 43, 704-713.

[6] Škrabl, S., and Macuh, B. (2005). Upper-bound solutions of three-dimensional passive earth pressures. *Canadian Geotechnical Journal*, Ottawa, 42, 1449-1460.

[7] Soubra, A. H., and Regenass, P. (2000). Three-dimensional passive earth pressure by kinematical approach. *Journal of Geotechnical and Geoenvironmental Engineering Division*, ASCE, 126(11), 969-978.

[8] Vrecl-Kojc, H., and Škrabl, S. (2007). Determination of passive earth pressure using three-dimensional failure mechanism. *Acta Geotechnica Slovenica*, 4(1), 10-23.

APROKSIMATIVNI IZRAZI GREEN-OVE FUNKCIJE POLNESKONČNEGA ELASTIČNEGA MEDIJA

TOMAŽ PLIBERŠEK IN ANDREJ UMEK

o avtorjih

Tomaž Pliberšek
Univerza v Mariboru,
Fakulteta za gradbeništvo
Smetanova 17, 2000 Maribor, Slovenija
E-pošta: tomaz.plibersek@uni-mb.si

Andrej Umek
Univerza v Mariboru,
Fakulteta za gradbeništvo
Smetanova 17, 2000 Maribor, Slovenija
E-pošta: umek@uni-mb.si

izvleček

Greenova funkcija homogenega in slojevitega pol-prostora na površini obremenjenega s harmonično, koncentrirano silo poljubne smeri je v splošnem podana z integralno predstavitvijo. Izvrednotenje te predstavitve v diskretnih točkah je matematično zahtevno in zahteva veliko računalniškega časa. Avtorja sta v svojih predhodnih člankih izvrednotenje Greenove funkcije poenostavila tako, da sta iz pol-neskončnega Hankelovega integrala izdvojila singularni del, del ki je vezan na površinske valove in preostali del pretvorila v integral preko končnega integracijskega območja, ki je manj zahteven za izvrednotenje. Inženirska praksa preračuna dinamičnih lastnosti in neintruzivne identifikacije temeljnih tal nakazujeta potrebo po nadaljnji poenostavitvi izrazov za Greenovo funkcijo.

Članek obravnava razvoj aproksimativnih funkcij za določevanje pomikov v tolerancah inženirske natančnosti na osnovi eksaktno diskretiziranih komponent Greenove funkcije. Njihova natančnost bi naj bila boljša kot so tolerance intruzivnih merskih podatkov identifikacije mehanskih karakteristik zemljine. Verjamemo, da bo uporaba v članku izpeljanih aproksimativnih izrazov zmanjšala matematični napor pri reševanju interakcijskih problemov konstrukcija - zemljina istočasno pa odprla nove možnosti za neintruzivne identifikacije zemljin.

ključne besede

elasto-dinamika, pol-prostor, Greenova funkcija, aproksimativne rešitve

APPROXIMATE EXPRESSIONS FOR THE GREEN'S FUNCTIONS OF A SEMI-INFINITE, ELASTIC MEDIUM

TOMAŽ PLIBERŠEK and ANDREJ UMEK

About the authors

Tomaž Pliberšek
University of Maribor,
Faculty of Civil Engineering
Smetanova 17, 2000 Maribor, Slovenia
E-mail: tomaz.plibersek@uni-mb.si

Andrej Umek
University of Maribor,
Faculty of Civil Engineering
Smetanova 17, 2000 Maribor, Slovenia
E-mail: umek@uni-mb.si

Abstract

On the basis of an exact, discretized presentation of the Green's function components, their closed-form approximations are developed. Their accuracy is considered to be better than the tolerances in the intrusive measurements data for the identification of the mechanical characteristics of soils. The use of these approximate expressions is believed to considerably reduce the computational effort in soil-structure interaction problems and open up new possibilities for the non-intrusive identification of soils.

Keywords

elastodynamics, half-space, Green's function, approximate solutions

1 INTRODUCTION

The Green's function of a semi-infinite medium yields the best description of the dynamic properties of soil in many problems in soil-structure interaction, earthquake engineering and seismology. Many authors have dealt with the problem of how to determine the Green's function for a semi-infinite elastic medium and have limited their attention to homogeneous and layered half-spaces. The latter appear to be the most general case of structured half-spaces for which an analytical expression can be derived. We further limit our attention to the surface displacements Green's function due to a unit, harmonic point force. It has been shown that these displacements can be expressed through semi-infinite integrals, e.g., Lamb [1], Ewing et al. [2], Wolf [3] etc., of the form:

$$u_{i,j}(a) = \int_0^\infty f_{i,j}(\eta) \cdot J_n(a \cdot \eta) d\eta \qquad (1)$$

where $u_{i,j}$ is one of the displacement components and i describes its coordinate direction. In the most commonly used cylindrical coordinate system, therefore, i stands for r, ϑ and z, respectively. j describes the direction of the unit, harmonic force acting on the surface of the semi-infinite medium. $f_{i,j}$ is the characteristic function of the problem. Its poles and branch cuts are associated with the surface and body waves of the particular problem, respectively. J_n is a Bessel function of the first kind and nth order. In the treated problem n can take the values 0, 1 and 2. And, finally, a is the dimensionless distance from the source point given by:

$$a = \frac{r \cdot \omega}{v_s} \qquad (2)$$

where r is the physical distance from the source point, ω is the angular velocity of the harmonic excitation and v_s is the shear wave velocity in the uppermost layer of the layered half-space and in the homogeneous half-space, respectively.

The integrals (1) cannot be evaluated analytically, not even in the simplest case of a homogeneous half-space. Their numerical evaluation is highly demanding and time-consuming for two reasons. We have, due to the presence of the Bessel function J_n, to cope with an oscillating integrand and for the components of the Green's function, which are singular at its origin, the portions of the integration paths near and at infinity contribute significantly to the value of the integrals. Furthermore, the latter ones determine the type of the singularity at the point of the origin of the Green's function. Many authors have explored the possibilities of how to perform the numerical integration. Their attempts ran

in two different directions. The first group, e.g., Kobori et al. [4], Stade and Layton [5], Zhielkin and Kukarkin [6], Lemoin [7], Secada [8], Lucas and Stone [9], Wang et al. [10], Martinez-Castro and Gallego [11], etc., kept the original integration path along the positive real axis of the integration variable from 0 to ∞ and used a special integration algorithm known as the Fast Fourier-Bessel transform (FFBT). The procedure proposed by the above-mentioned authors differs slightly from one to the other, but they have several factors in common. With the use of the FFBT algorithm they avoided the problems with an oscillating integrand. However, some of the problems remained, which can be clearly seen from the basic concept of this algorithm. Its principal idea is to introduce the integral representation of the Bessel function J_n into the Eq. (1) and then exchange the orders of the integration. This yields the following:

$$u_i(a) = \frac{i^n}{2\pi} \int_{-\pi}^{\pi} e^{in\alpha}\, d\alpha \int_0^{\infty} f_{i,j}(\eta) e^{-ia\eta\cos\alpha}\, d\eta \qquad (3)$$

The inner integral can be viewed as a Fourier transform of the function $f_{i,j}$ in the transform variable $a\cos\alpha$, if we consider it as:

$$f_{i,j}(\eta) = \begin{cases} f_{i,j}(\eta), & \eta \geq 0 \\ 0, & \eta < 0 \end{cases} \qquad (4)$$

Therefore, the inner integral of Eq. (3) can be, in principle, efficiently numerically evaluated by a Fast Fourier Transform (FFT) algorithm, leading to an easy numerical integration over a finite range. However, using the FFBT algorithm we are still faced with two significant problems. A more detailed analysis of the functions $f_{i,j}$ shows that for the components of the Green's function, which are singular at the origin, gilts:

$$\lim_{\eta\to\infty} f_{i,j}(\eta) \neq 0 \qquad (5)$$

Therefore, the conditions for the existence of the Fourier Transform, as e.g., given by Sneddon [12], are not satisfied and therefore the Fast Fourier Transform (FFT) of this part of the integrand is of questionable validity, as noted by Pliberšek and Umek [13]. Some of the authors were apparently aware of this fact, e.g., Vostroukhov et al. [14]. They avoided this problem by replacing the point force through a statically equivalent loading distributed over a small area and obtained by the Saint-Venant principle the Green's function with satisfying accuracy except at, and close to, its origin. The others split the Green's function components into their regular and singular parts, respectively. The right-hand side of equation (1) thus becomes:

$$u_i(a) = \frac{\lim\limits_{\eta\to\infty} f_{i,j}(\eta)}{a} \left(1 + \frac{a}{\lim\limits_{\eta\to\infty} f_{i,j}(\eta)} \int_0^{\infty} g_{i,j}(\eta) J_n(a\eta)\, d\eta \right) \qquad (6)$$

where $g_{i,j}$ is defined as:

$$g_{i,j}(\eta) = f_{i,j}(\eta) - \lim_{\eta\to\infty} f_{i,j}(\eta) \qquad (7)$$

The extraction of singularity ensured that the Fourier transform of the function $g_{i,j}$ exists; however, the other apparent difficulty that we integrate in the case of no material damping through its singularities and in the case of some material damping, which is usually the realistic case, close to its singularities remains. From Eq. (7) it is clear that the singularities of the function $f_{i,j}$ are also present in the function $g_{i,j}$ since they differ by a constant only. In the case of zero material damping in at least one of the layers one should add to the Fourier integral the contributions coming from small semicircles around the poles of the integrand. In the case of small material damping, conducting the integration path close to the poles of the integrand can lead to numerical instabilities, as reported by Kobori et al. [4].

The first attempts known to us to avoid the described problems and to transform the integral in Eq. (6) to a new integration path are those of Kobayashi and Sassaki [15] and Kobayashi [16]. They limited their attention to a homogeneous half-space and succeeded in transforming the semi-infinite integrals to keyhole integrals along a suitably chosen branch cut, which they further reduced to the integral from zero to one. The latter one has to be evaluated numerically, however, without any numerical difficulties and instabilities. Štrukelj et al. [17] and Pliberšek et al. [18] and [19] extended Kobayashi's approach to the case of layered media. They reduced the semi-infinite inversion integrals to a number of keyhole integrals, where their number is equal to the number of layers in the case that internal damping within the layers is different.

Whichever of the above-described approaches we chose, the results obtained are in the form of discrete values of the Green's function components at chosen dimensionless distances from the source point. Such a presentation is suitable to be used e.g., in soil-structure interaction problems, although it requires more computational effort than the closed-form solution in the case that the latter could be obtained. The discretized data solution is, however, not suitable for a number of technically relevant tasks. It cannot be used for a direct identification of the Green's function from non-intrusive measurements; it also can not be used for the soil identification via the

Green's function, which would parallel the better-known SASW method. With all this in mind we present in this paper approximate, closed-form expressions for the Green's function components. The bounds for the error were set in such a way that the differences between the exact, discretized presentation and the presented approximate expressions are not larger than the tolerances during the intrusive measurements data. In this paper we limit our attention to the homogeneous half-spaces.

2 BASIC CONCEPT OF THE APPROXIMATION

The approximation to the Green's function for a semi-infinite medium can derived on the basis of Eq. (1) and (6), respectively. We decided to proceed from Eq. (6). This starting point has two advantages. The first one is that all the integrals appearing in this equation, regardless of the Green's function component considered, show the same basic behavior and are expressed in the same general form. This is, however, not the case with the integrals in equation (1), where some of them exhibit singular behavior at the source point and the others do not. Therefore, the method developed to approximate one of the integrals in Eq. (6) can be applied to the others. The only difference between the components that, are singular at the origin and those that are not, is that for the latter ones the constant is equal to zero and for the former ones it is a well-determined value. However, all the integrals:

$$\lim_{\eta \to \infty} f_{i,j}(\eta) \qquad (8)$$

Regardless of whether they belong to the components of the Green's function, which are singular or regular at the source point, behave in the same way. The second advantage of this approach is that the singular term in the Green's function, where it exists, is given exactly. In many important practical applications, e.g., soil-structure interaction problems, only the values of the Green's function over small distances from the source point are required and there the singular term is the dominant one. Therefore, extracting the singularity greatly improves the accuracy of the approximation.

From the literature, e.g., [20] and [21], several asymptotic expansions of the integrals are known. It can be, however, concluded that the integral in Eq. (6) and given by Eq. (8) cannot be transformed to any one of the standard examples. The Bessel function in the integrand prevents us from transforming it to a Laplace-type integral:

$$I_{i,j}(a) = \int_0^\infty g_{i,j}(\eta) J_n(a\eta) d\eta \qquad (9)$$

as given by Miklowitz [20], on which the method of steepest descent is based, nor to a Fourier-type integral:

$$I_L(x) = \int_a^b f(t) e^{x g(t)} dt \qquad (10)$$

which is the foundation for the stationary phase method. The third possibility, also presented by Miklowitz [20], would be the integration per-parts approach. It is from the structure of the integral, defined by Eq. (10), clear that this approach also does not lead to a desired asymptotic expansion of the Green's function. The first one or two steps show that we have to deal with the derivatives of the Bessel function, which make the expressions obtained too complicated and no clear convergence could be established.

After realizing that in wave mechanics standard approximations of integrals do not yield satisfactory results, we are left with two options. The first one would be to approximate the integrands in Eq. (6) by a suitably chosen family of functions in the sense of the L_2 norm and then conduct the integration. The second one is to approximate the integral in the same sense.

To decide on which of these two types of approximation of the integral in Eq. (6) is more appropriate, we first need to study the behavior of its integrand. It is clear that the integrand is the product of two functions, which behave extremely differently. The function $g_{i,j}(\eta)$ is a relatively slow varying function except in the vicinity of its poles and branch points, which lie in the case of zero material damping on the integration path and, in the case of realistically assumed material damping, close to it. The second function, the Bessel function, is a smooth but oscillating function. The characteristic behavior of these functions for zero and 0.03 material damping is presented in Fig. 1 and 3. The characteristic behavior of the integrand as a whole is given in Fig 2 and 4.

The combination of the oscillatory behavior of the Bessel function with the rapid changes of the function $g_{i,j}$, close to their singularities and their smooth behavior far from them, represent a considerable difficulty in approximating the integrand through one or a combination of the families of the functions most commonly used in numerical mathematics, i.e., polynomials and exponential functions of the real and imaginary argument, respectively [22]. Therefore, the integrand in Eq. (6) cannot be considered as an appropriate starting point to derive the approximation.

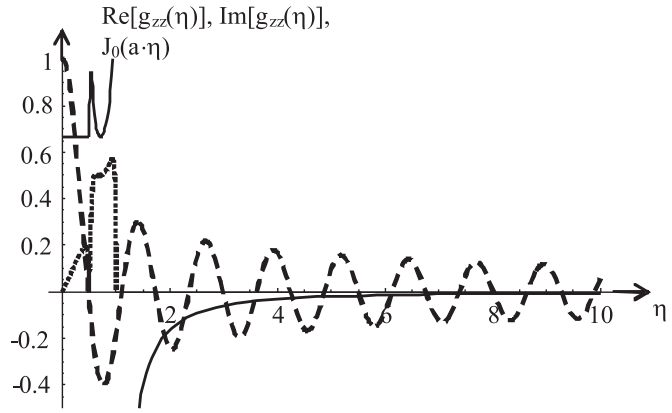

Figure 1. Parts of the integrand for the vertical displacements due to a unit vertical force: real part of the function $g_{zz}(\eta)$, the solid line; imaginary part of the function $g_{zz}(\eta)$, the dotted line; and the Bessel function $J_0(a\cdot\eta)$, the broken line. The following values for the material constants have been assumed: Poisson's ratio $\nu=\frac{1}{3}$, material damping h=0 and the dimensionless distance a=5.

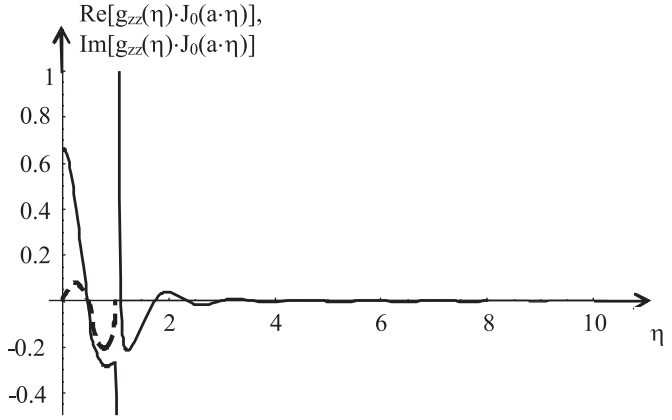

Figure 2. The integrand for the vertical displacements due to a unit vertical force: the real part is given by the solid and the imaginary part by the broken line. The following values for material have been assumed: Poisson's ratio $\nu=\frac{1}{3}$, material damping h=0 and the dimensionless distance a=5.

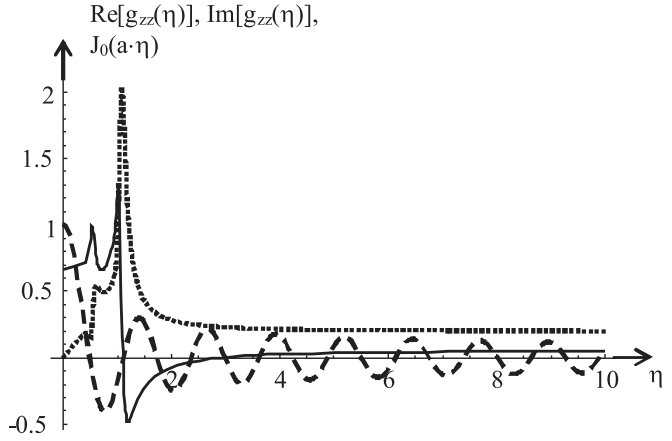

Figure 3. Parts of the integrand for the vertical displacements due to a unit vertical force: real part of the function $g_{zz}(\eta)$, the solid line; imaginary part of the function $g_{zz}(\eta)$, the dotted line; and the Bessel function $J_0(a\cdot\eta)$, the broken line. The following values for the material constants have been assumed: Poisson's ratio $\nu=\frac{1}{3}$, material damping h=0.03 and the dimensionless distance a=5.

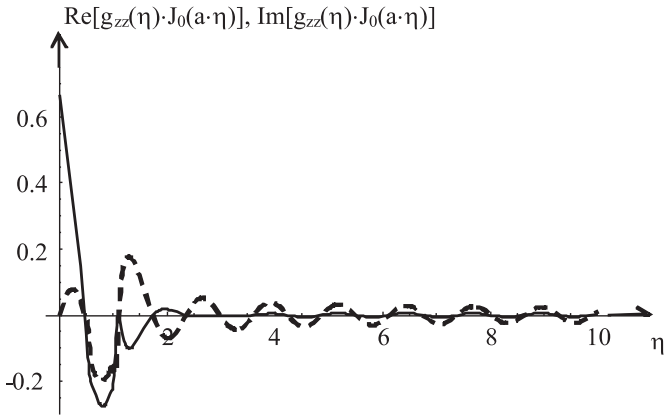

Figure 4. The integrand for the vertical displacements due to a unit vertical force: the real part is given by the solid and the imaginary part by the broken line. The following values for the material constants have been assumed: Poisson's ratio $\nu = \frac{1}{3}$, material damping h=0.03 and the dimensionless distance a=5.

We now turn our attention to the integral in Eq. (6), which is given by Eq. (8). In the example presented in Figure 5 we can see that the integration smoothes the rapid and irregular changes of the integrand. The result is a function that, is characterized by a fairly regular oscillation with a smooth and decreasing envelope, and these observations apply to the real as well as to the imaginary part of the integral. Therefore, the integrals $I_{i,j}(a)$ are chosen as a basis for the approximation. It is also clear that the polynomials are not the best family of functions to approximate curves, like those presented in Figure 5. Therefore, we chose as a basis for the approximation a combination of trigonometric and exponential functions of the real argument. Some promising combinations are examined in detail in the next paragraph.

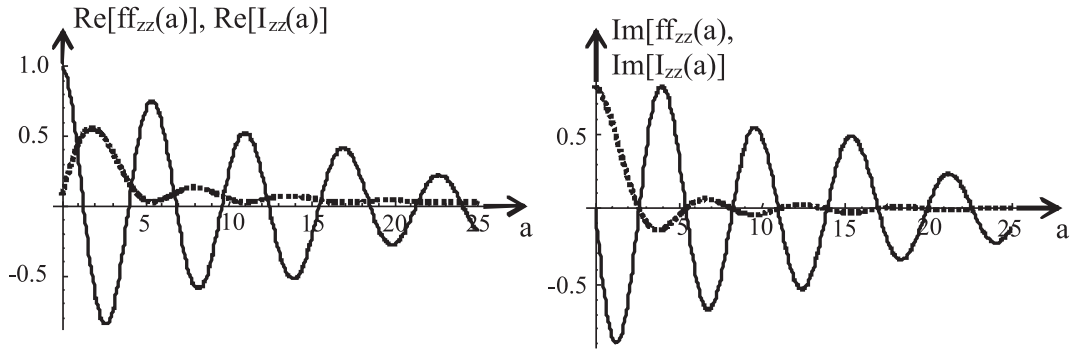

Figure 5. Comparison of the integral $I_{zz}(a)$ with the corresponding fundamental function.

From Figure 5 it can also be seen that the fundamental function, which is defined as:

$$ff_{i,j}(a) = 1 + \frac{a}{\lim\limits_{\eta\to\infty} f_{i,j}(\eta)} \int_0^\infty g_{i,j}(\eta) J_n(a\,\eta) d\eta \qquad (11)$$

is a more suitable choice for the approximation, once we have decided to use the trigonometric and exponential functions of the real argument as families of the approximating functions.

On the basis of Figures 5 and 6 (next page) and other components studied, the following approximation was investigated in detail:

$$\left.\begin{matrix}\mathrm{Re}\\ \mathrm{Im}\end{matrix}\right\}(ff_{i,j}(a)) \approx \left.\begin{matrix}\mathrm{Re}\\ \mathrm{Im}\end{matrix}\right\}(apff_{i,j}(a)) = \sum_{i=1}^{n} e^{-\gamma_i a} \cdot c_i \cdot \left.\begin{matrix}\sin\\ \cos\end{matrix}\right\}(b_i \cdot a) \qquad (12)$$

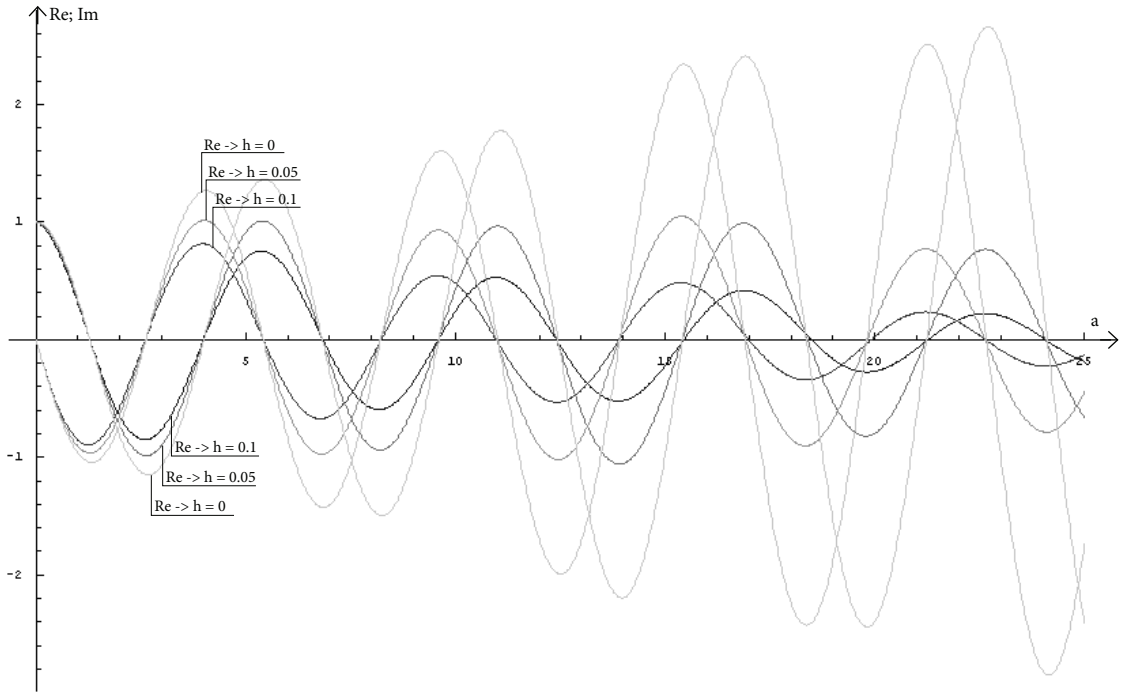

Figure 6. The fundamental function for the vertical displacement due to a unit vertical force for the chosen material damping values. The Poisson's ratio $\nu = \frac{1}{3}$ has been assumed.

The real and imaginary parts of the fundamental functions were approximated independently from each other, as indicated by the symbol $\left.\begin{matrix}\mathrm{Re}\\ \mathrm{Im}\end{matrix}\right\}$. In their approximations the sinuses or cosinuses were applied, indicated by the symbol $\left.\begin{matrix}\sin\\ \cos\end{matrix}\right\}$, the former ones in the case that the value of the fundamental function at a=0 is zero and the cosinuses otherwise. For the approximate fundamental function the symbol $ap_{ffi,j}(a)$ is used.

3 ILLUSTRATIVE EXAMPLE

For the illustrative example, the fundamental function for the vertical displacement due to the vertical unit, the harmonic force has been chosen and the range of the dimensionless distance a, given by Eq. (2), from 0 to 25 has been selected. It is believed that this range of dimensionless distance is sufficient for the problems of soil-structure interaction and Green's function identification. Two different material dampings were considered, h=0.10 and h=0.03. The first one stands for the soils with relatively high damping and the second for the soils with low damping. The number of terms in the approximation was chosen to be one, two and three, respectively. The best-fit approximations were performed using the program Matematica.

3.1 ONE-TERM APPROXIMATION

In the on-term approximation we use:

$$\mathrm{Re}(ff_{z,z}(a)) \approx \mathrm{Re}(apff_{z,z}(a)) = c_1 \cdot e^{-\gamma_1 \cdot a} \cdot \cos(b_1 \cdot a) \qquad (13)$$

and

$$\mathrm{Im}(ff_{z,z}(a)) \approx \mathrm{Im}(apff_{z,z}(a)) = c_2 \cdot e^{-\gamma_2 \cdot a} \cdot \sin(b_2 \cdot a) \qquad (14)$$

The least-squares approximation for the internal damping h=0.10 yields the following values for the coefficients in equations (13) and (14):

c_1=0.995985	γ_1=0.0596105	b_1=1.12597
c_2=-0.985963	γ_2=0.0581773	b_2=1.12614

The comparison between the exact results following Kobayshi's approach and the approximation derived above is shown in Fig. 7.

The error in the above-defined approximation is:

$$err_1 = \frac{1}{25.0} \cdot \int_0^{25.0} \left[\mathrm{Re}(ff_{z,z}(a)) - \mathrm{Re}(apff_{z,z}(a))\right]^2 da = 0.00669295 \qquad (15)$$

and

$$err_2 = \frac{1}{25.0} \cdot \int_0^{25.0} \left[\mathrm{Im}(ff_{z,z}(a)) - \mathrm{Im}(apff_{z,z}(a))\right]^2 da = 0.00667756 \qquad (16)$$

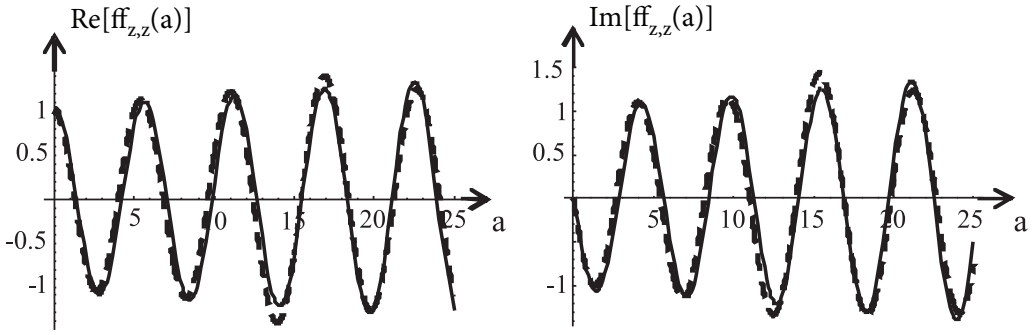

Figure 7. Comparison of the exact fundamental function $f_{zz}(a)$, given by the broken line; and its one-term approximation, given by the solid line. The material damping was assumed to be h=0.10.

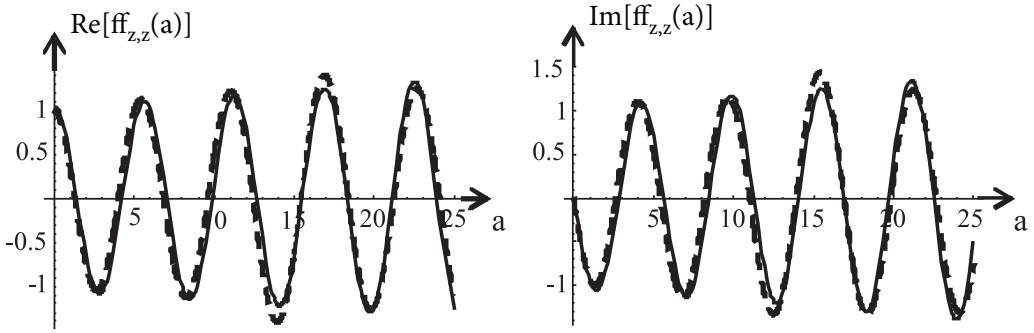

Figure 8. Comparison of the exact fundamental function $f_{zz}(a)$, given by the broken line; and its one-term approximation, given by the solid line. The material damping was assumed to be h=0.03.

For the material damping h=0.03 the least-squares approximation yields:

c_1=1.0507	γ_1=-0.0106777	b_1=1.11609
c_2=-1.03608	γ_2=-0.0122008	b_2=1.11682

The comparison between the exact and appreciative values of the fundamental function is shown in Figure 8. The material damping was assumed to be h=0.03. The error for this case is:

For the real part the approximation is:

$$err_3 = \frac{1}{25.0}\cdot\int_0^{25.0}\left[\mathrm{Re}(ff_{z,z}(a)) - \mathrm{Re}(apff_{z,z}(a))\right]^2 da = 0.0325395 \quad (17)$$

and for the imaginary part, respectively:

$$err_4 = \frac{1}{25.0}\cdot\int_0^{25.0}\left[\mathrm{Im}(ff_{z,z}(a)) - \mathrm{Im}(apff_{z,z}(a))\right]^2 da = 0.0312312 \quad (18)$$

3.2 TWO-TERMS APPROXIMATION

In the two-terms approximation we use:

$$\mathrm{Re}(ff_{z,z}(a)) \approx \mathrm{Re}(apff_{z,z}(a)) = \sum_{i=1}^{2} c_i \cdot e^{-\gamma_i \cdot a} \cdot \cos(b_i \cdot a) \quad (19)$$

and

$$\mathrm{Im}(ff_{z,z}(a)) \approx \mathrm{Im}(apff_{z,z}(a)) = \sum_{i=1}^{2} c_{i+2} \cdot e^{-\gamma_{i+2} \cdot a} \cdot \sin(b_{i+2} \cdot a) \quad (20)$$

Following the same procedure as in the one-term approximation the coefficients in equations (19) and (20) for the material damping h=0.10 are determined. They are as follows:

c_1=-1.5	γ_1=0.120606	b_1=1.01333
c_2=2.50383	γ_2=0.109332	b_2=1.08702
c_3=-0.259736	γ_3=-0.0143126	b_3=1.08191
c_4=-0.692457	γ_4=0.0637071	b_4=1.18805

On the basis of the above-listed coefficients, the errors were computed. They are, for the real part:

$$err_1 = \frac{1}{25.0} \cdot \int_0^{25.0} \left[\mathrm{Re}(ff_{z,z}(a)) - \mathrm{Re}(apff_{z,z}(a)) \right]^2 da = 0.00123647 \quad (21)$$

and for the imaginary part:

$$err_2 = \frac{1}{25.0} \cdot \int_0^{25.0} \left[\mathrm{Im}(ff_{z,z}(a)) - \mathrm{Im}(apff_{z,z}(a)) \right]^2 da = 0.00238762 \quad (22)$$

respectively. For the material damping h=0.03 the following values were obtained:

c_1=-0.552778	γ_1=0.0307106	b_1=0.968259
c_2=1.54378	γ_2=0.0197715	b_2=1.10899
c_3=-1.85541	γ_3=0.0272306	b_3=1.10019
c_4=0.849891	γ_4=0.0394818	b_4=0.99098

The corresponding errors are:

$$err_3 = \frac{1}{25.0} \cdot \int_0^{25.0} \left[\mathrm{Re}(ff_{z,z}(a)) - \mathrm{Re}(apff_{z,z}(a)) \right]^2 da = 0.00347543 \quad (23)$$

and

$$err_4 = \frac{1}{25.0} \cdot \int_0^{25.0} \left[\mathrm{Im}(ff_{z,z}(a)) - \mathrm{Im}(apff_{z,z}(a)) \right]^2 da = 0.00348752 \quad (24)$$

3.3 THREE-TERMS APPROXIMATION

In the three-terms approximation we use:

$$\mathrm{Re}(ff_{z,z}(a)) \approx \mathrm{Re}(apff_{z,z}(a)) = \sum_{i=1}^{3} c_i \cdot e^{-\gamma_i \cdot a} \cdot \cos(b_i \cdot a) \quad (25)$$

and

$$\mathrm{Im}(ff_{z,z}(a)) \approx \mathrm{Im}(apff_{z,z}(a)) = \sum_{i=1}^{3} c_{i+3} \cdot e^{-\gamma_{i+3} \cdot a} \cdot \sin(b_{i+3} \cdot a) \quad (26)$$

The coefficients in equations (25) and (26) for the half-space with material damping h=0.10 are:

c_1=0.640348	γ_1=0.0259827	b_1=1.11881
c_2=0.37689	γ_2=0.111726	b_2=1.25876
c_3=-0.0230052	γ_3=-0.0752526	b_3=0.861735
c_4=-1.53327	γ_4=0.100735	b_4=1.10478
c_5=0.476431	γ_5=0.076713	b_5=0.954981
c_6=0.0601061	γ_6=0.013543	b_6=0.493489

The corresponding errors are:

$$err_1 = \frac{1}{25.0} \cdot \int_0^{25.0} \left[\mathrm{Re}(ff_{z,z}(a)) - \mathrm{Re}(apff_{z,z}(a)) \right]^2 da = 0.000894818 \quad (27)$$

for the real and

$$err_2 = \frac{1}{25.0} \cdot \int_0^{25.0} \left[\mathrm{Im}(ff_{z,z}(a)) - \mathrm{Im}(apff_{z,z}(a)) \right]^2 da = 0.0000275089 \quad (28)$$

for the imaginary part, respectively. We now turn our attention to the three-terms approximation for the case when the material damping is 0.03. The following coefficients were computed for this case:

c_1=0.726239	γ_1=0.0269564	b_1=1.18327
c_2=0.336632	γ_2=-0.068329	b_2=1.10594
c_3=-0.0492427	γ_3=-0.0950448	b_3=0.868245
c_4=-0.530666	γ_4=-0.0570736	b_4=1.10957
c_5=-0.455507	γ_5=0.0101311	b_5=1.22544
c_6=0.0352293	γ_6=-0.106017	b_6=0.856865

The errors for this case are:

$$err_3 = \frac{1}{25.0} \cdot \int_0^{25.0} \left[\mathrm{Re}(ff_{z,z}(a)) - \mathrm{Re}(apff_{z,z}(a)) \right]^2 da = 0.00202942 \quad (29)$$

and

$$err_4 = \frac{1}{25.0} \cdot \int_0^{25.0} \left[\mathrm{Im}(ff_{z,z}(a)) - \mathrm{Im}(apff_{z,z}(a)) \right]^2 da = 0.00249281 \quad (30)$$

4 DISCUSSION OF THE RESULTS AND CONCLUSIONS

The error analysis for all three cases the one-, two- and three-term approximations of the fundamental function and for both representative material dampings clearly show that the components of the Green's function for the homogeneous half space can be, in the framework of engineering accuracy, approximated by a simple, closed-form analytical expression. These closed-form analytical expressions can be used, on the one hand, to significantly reduce the numerical effort in soil-structure interaction problems and, on the other hand, to identify the mechanical properties of the soil through non-intrusive methods by measuring the induced vibration of the half space and identifying the coefficients in equation (12).

From the error estimates presented in the preceding paragraph it can be concluded that the one-term approximation is accurate enough for most engineering purposes. Adding additional terms to the one-term expression leads to the two- and three-term formulas and reduces the errors. The significant reduction of the

error is limited to the transition from the one- to two-term formulas. The subsequent error reduction are less pronounced, and therefore we stopped our analysis after three terms. On the other hand, the numerical effort in deriving three- and more-term formulas increases significantly and also leads to the formulas of higher complexity with no, from the engineering view point, significant gains in accuracy. It is believed that one- and two-term formulas are the most useful. The choice of the former or the latter depends on the problem they will be used.

It is clear that higher material damping permits a better approximation than with the lower one. This is due to the fact that the exponential envelope we used in our work, which can be seen from equation (12), is more suitable for higher material damping. Despite the fact that relevant engineering approximations of the Green's function components were obtained, we believe that in the definition of the most suitable mathematical formulation of the envelope there is still some room for improvements.

REFERENCES

[1] A[1] Lamb, H. (1904). On the Propagation of Tremors over the Surface of an Elastic Solid. Phil. Trans. A 203, 1 – 42.

[2] Ewing, M.W., Jardetzky, W.S., Press, F. (1957). Elastic waves in layered media. McGraw-Hill Book Company, New York.

[3] Wolf, J.P., 1985. Dynamic Soil – Structure Interaction. Prentice – Hall, Inc., Englewood Cliffs, New Jersey.

[4] Kobori, T., Miura, K., Moroi, T. (1987). Fast Fourier Bessel Transform for Calculating the Green's Function for Semi-Infinite Soil Media. 3rd Int. Conf. Soil Dyn. Earthq. Eng. Vol. 3, 365-374.

[5] Stade, E., Layton, E.G. (1995). Generalized discrete Fourier transforms: the discrete Fourier-Riccati-Bessel transform. Computer Physics Communications 85, 336-370.

[6] Zhielkin, Ya.M., Kukarkin, A.B. (1995). On an algorithm for the fast Fourier-Bessel transform (in Russian). Zh. Vychisl. Mat. i Mat. Fiz. 35 (7), 1128-1133.

[7] Lemoin, D. (1997). Optimal cylindrical and spherical Bessel transforms satisfying bound state boundary conditions. Computer Physics Communications 99, 297-306.

[8] Secada, J.D. (1999). Numerical evaluation of the Hankel transform. Computer Physics Communications 116, 278-294.

[9] Lucas, S.K., Stone, H.A. (1995). Evaluating infinite integrals involving Bessel functions of arbitrary order. Journal of Computational and Applied Mathematics 64, 217-231.

[10] Wang, C.D., Tzeng, C.S., Pan, E., Liao, J.J. (2003). Displacements and Stresses due to a vertical point load in an inhomogeneous transversely isotropic half-space. International Journal of Rock Mechanics and Mining Sciences 40, 667-685.

[11] Martinez-Castro, A.E., Gallego, R. (2007). Three-dimensional Green's function for time-harmonic dynamics in a viscoelastic layer. International Journal of Solids and Structures (IJSS) 44, 4541-4558.

[12] Sneddon, I.H. (1972), The use of integral transforms, McGraw-Hill, New York.

[13] Pliberšek, T., Umek, A. On the evaluation of the Green's function of semi-infinite, layered elastic medium. International Journal of Solids and Structures (IJSS), under review.

[14] Vostroukhov, A.V., Verichev, S.N., Kok, A.W.M. and Esveld, C. (2004). Steady-state response of stratified half-space subjected to a horizontal arbitrary buried uniform load applied at a circular area. Soil Dynamics and Earthquake Engineering 24, 449-459.

[15] Kobayashi, T., Sasaki, F. (1991). Evaluation of Green's function on semi-infinite elastic medium. KICT Report No.86, Kajima Technical Research Institute, Kajima Corporation.

[16] Kobayashi, T. (1981). Evaluation of response to point load excitation on semi-infinite elastic medium (in Japanese). Tran. Archi. Institute., Japan 302, 29-35.

[17] Štrukelj, A., Pliberšek, T., Umek, A. (2006). Evaluation of Green's function for vertical point load excitation applied to the surface of a layered semi-infinite elastic medium. Arch. Appl. Mech. (AAM) 76, 465-479.

[18] Pliberšek, T., Štrukelj, A., Umek, A. (2005). Green's function for an elastic layer loaded harmonically on its surface. Acta Geotechnica Slovenica (AGS) 2 (1), 4-21.

[19] Pliberšek T., Umek A. (2008). Green's function for tangentially loaded layered half-space. Acta Geotechnica Slovenica (AGS), 5 (1), 50-69.

[20] Miklowitz, J. (1978). The Theory of Elastic Waves and Waveguides, North-Holland. Amsterdam, pp. 250 – 297.

[21] Erdelyi, A. (1956). Asymptotic expansions. Dover, New York.

[22] Hamming, R.W.(1973). Numerical methods for scientist and Engineers. McGraw-Hill, New York.

NAVODILA AVTORJEM

Članki so objavljeni v angleškem jeziku s prevodom izvlečka v slovenski jezik.

VSEBINA ČLANKA

Članek naj bo napisan v naslednji obliki:

- Naslov, ki primerno opisuje vsebino članka in ne presega 80 znakov.
- Izvleček, ki naj bo skrajšana oblika članka in naj ne presega 250 besed. Izvleček mora vsebovati osnove, jedro in cilje raziskave, uporabljeno metodologijo dela, povzetek izidov in osnovne sklepe.
- Uvod, v katerem naj bo pregled novejšega stanja in zadostne informacije za razumevanje ter pregled izidov dela, predstavljenih v članku.
- Teorija.
- Eksperimentalni del, ki naj vsebuje podatke o postavitvi preiskusa in metode, uporabljene pri pridobitvi izidov.
- Izidi, ki naj bodo jasno prikazani, po potrebi v obliki slik in preglednic.
- Razprava, v kateri naj bodo prikazane povezave in posplošitve, uporabljene za pridobitev izidov. Prikazana naj bo tudi pomembnost izidov in primerjava s poprej objavljenimi deli.
- Sklepi, v katerih naj bo prikazan en ali več sklepov, ki izhajajo iz izidov in razprave.
- Literatura, ki mora biti v besedilu oštevilčena zaporedno in označena z oglatimi oklepaji [1] ter na koncu članka zbrana v seznamu literature.

OBLIKA ČLANKA

Besedilo naj bo pisano na listih formata A4, z dvojnim presledkom med vrstami in s 3.0 cm širokim robom, da je dovolj prostora za popravke lektorjev. Najbolje je, da pripravite besedilo v urejevalniku Microsoft Word. Hkrati dostavite odtis članka na papirju, vključno z vsemi slikami in preglednicami ter identično kopijo v elektronski obliki.

Enačbe naj bodo v besedilu postavljene v ločene vrstice in na desnem robu označene s tekočo številko v okroglih oklepajih.

ENOTE IN OKRAJŠAVE

V besedilu, preglednicah in slikah uporabljajte le standardne označbe in okrajšave SI. Simbole fizikalnih veličin v besedilu pišite poševno (npr. v, T itn.). Simbole enot, ki sestojijo iz črk, pa pokončno (npr. Pa, m itn.).

Vse okrajšave naj bodo, ko se prvič pojavijo, izpisane v celoti.

SLIKE

Slike morajo biti zaporedno oštevilčene in označene, v besedilu in podnaslovu, kot sl. 1, sl. 2 itn. Posnete naj bodo v kateremkoli od razširjenih formatov, npr. BMP, JPG, GIF. Za pripravo diagramov in risb priporočamo CDR format (CorelDraw), saj so slike v njem vektorske in jih lahko pri končni obdelavi preprosto povečujemo ali pomanjšujemo.

Pri označevanju osi v diagramih, kadar je le mogoče, uporabite označbe veličin (npr. v, T). V diagramih z več krivuljami mora biti vsaka krivulja označena. Pomen oznake mora biti razložen v podnapisu slike.

Za vse slike po fotografskih posnetkih je treba priložiti izvirne fotografije ali kakovostno narejen posnetek.

PREGLEDNICE

Preglednice morajo biti zaporedno oštevilčene in označene, v besedilu in podnaslovu, kot preglednica 1, preglednica 2 itn. V preglednicah ne uporabljajte izpisanih imen veličin, ampak samo ustrezne simbole. K fizikalnim količinam, npr. t (pisano poševno), pripišite enote (pisano pokončno) v novo vrsto brez oklepajev.

Vse opombe naj bodo označene z uporabo dvignjene številke[1].

SEZNAM LITERATURE

Vsa literatura mora biti navedena v seznamu na koncu članka v prikazani obliki po vrsti za revije, zbornike in knjige:

[1] Feng, T. W. (2000). Fall-cone penetration and water content ralationship of clays. Geotechnique 50, No. 2, 181-187.
[2] Ortolan, Ž. and Mihalinec, Z. (1998). Plasticity index-Indicator of shear strength and a major axis of geotechnical modelling. Proceedings of the

Eleventh Danube-European conference on soil mechanics and geotechnical engineering, Poreč, 25 –29 May 1998.
[3] Toporišič, J. (1994). Slovenski pravopis. 2nd.ed., DZS, Ljubljana.

PODATKI O AVTORJIH

Članku priložite tudi podatke o avtorjih: imena, nazive, popolne poštne naslove, številke telefona in faksa, naslove elektronske pošte. Navedite kontaktno osebo.

SPREJEM ČLANKOV IN AVTORSKE PRAVICE

Uredništvo si pridržuje pravico do odločanja o sprejemu članka za objavo, strokovno oceno mednarodnih recenzentov in morebitnem predlogu za krajšanje ali izpopolnitev ter terminološke in jezikovne korekture.

Avtor mora predložiti pisno izjavo, da je besedilo njegovo izvirno delo in ni bilo v dani obliki še nikjer objavljeno. Z objavo preidejo avtorske pravice na revijo ACTA GEOTECHNICA SLOVENICA. Pri morebitnih kasnejših objavah mora biti AGS navedena kot vir.

Rokopisi člankov ostanejo v arhivu AGS.

Vsa nadaljnja pojasnila daje:

Uredništvo
ACTA GEOTECHNICA SLOVENICA
Univerza v Mariboru
Fakulteta za gradbeništvo
Smetanova ulica 17
2000 Maribor
Slovenija
E-pošta: ags@uni-mb.si

INSTRUCTIONS FOR AUTHORS

The papers are published in English with a translation of the abstract into Slovene.

FORMAT OF THE PAPER

The paper should have the following structure:

- A Title that adequately describes the content of the paper and should not exceed 80 characters;
- An Abstract, which should be viewed as a mini version of the paper and should not exceed 250 words. The Abstract should state the principal objectives and the scope of the investigation and the methodology employed, it should also summarise the results and state the principal conclusions;
- An Introduction, which should provide a review of recent literature and sufficient background information to allow the results of the paper to be understood and evaluated;
- A Theoretical section;
- An Experimental section, which should provide details of the experimental set-up and the methods used for obtaining the results;
- A Results section, which should clearly and concisely present the data using figures and tables where appropriate;
- A Discussion section, which should describe the relationships shown and the generalisations made possible by the results and discuss the significance of the results, making comparisons with previously published work;
- Conclusions, which should present one or more conclusions that have been drawn from the results and subsequent discussion;
- References, which must be numbered consecutively in the text using square brackets [1] and collected together in a reference list at the end of the paper.

LAYOUT OF THE TEXT

The text should be written in A4 format, with double spacing and margins of 3 cm, to provide editors with space to write in their corrections. Microsoft Word for Windows is the preferred format for submission. One hard copy, including all figures, tables and illustrations and an identical electronic version of the manuscript must be submitted simultaneously.

Equations should be on a separate line in the main body of the text and marked on the right-hand side of the page with numbers in round brackets.

UNITS AND ABBREVIATIONS

Only standard SI symbols and abbreviations should be used in the text, tables and figures. Symbols for physical

quantities in the text should be written in Italics (e.g. v, T, etc.). Symbols for units that consist of letters should be in plain text (e.g. Pa, m, etc.).

All abbreviations should be spelt out in full on first appearance.

FIGURES

Figures must be cited in consecutive numerical order in the text and referred to in both the text and the caption as Fig. 1, Fig. 2, etc. Figures may be saved in any common format, e.g. BMP, JPG, GIF. However, the use of CDR format (CorelDraw) is recommended for graphs and line drawings, since vector images can be easily reduced or enlarged during final processing of the paper.

When labelling axes, physical quantities (e.g. v, T) should be used whenever possible. Multi-curve graphs should have individual curves marked with a symbol; the meaning of the symbol should be explained in the figure caption.

Good quality black-and-white photographs or scanned images should be supplied for illustrations.

TABLES

Tables must be cited in consecutive numerical order in the text and referred to in both the text and the caption as Table 1, Table 2, etc. The use of names for quantities in tables should be avoided if possible: corresponding symbols are preferred. In addition to the physical quantity, e.g. t (in Italics), units (normal text), should be added on a new line without brackets.

Any footnotes should be indicated by the use of the superscript[1].

LIST OF REFERENCES

References should be collected at the end of the paper in the following styles for journals, proceedings and books, respectively:

[1] Feng, T. W. (2000). Fall-cone penetration and water content ralationship of clays. Geotechnique 50, No. 2, 181-187.

[2] Ortolan, Ž. and Mihalinec, Z. (1998). Plasticity index-Indicator of shear strength and a major axis of geotechnical modelling. Proceedings of the Eleventh Danube-European conference on soil mechanics and geotechnical engineering, Poreč, 25 –29 May 1998.

[3] Toporišič, J. (1994). Slovenski pravopis. 2nd.ed., DZS, Ljubljana.

AUTHOR INFORMATION

The following information about the authors should be enclosed with the paper: names, complete postal addresses, telephone and fax numbers and E-mail addresses. Indicate the corresponding person.

ACCEPTANCE OF PAPERS AND COPYRIGHT

The Editorial Committee of the Slovenian Geotechnical Review reserves the right to decide whether a paper is acceptable for publication, to obtain peer reviews for submitted papers, and if necessary, to require changes in the content, length or language.

Authors must also enclose a written statement that the paper is original unpublished work, and not under consideration for publication elsewhere. On publication, copyright for the paper shall pass to the ACTA GEOTECHNICA SLOVENICA. The AGS must be stated as a source in all later publication.

Papers will be kept in the archives of the AGS.

For further information contact:

Editorial Board
ACTA GEOTECHNICA SLOVENICA
University of Maribor
Faculty of Civil Engineering
Smetanova ulica 17
2000 Maribor
Slovenia
E-mail: ags@uni-mb.si

NAMEN REVIJE

Namen revije ACTA GEOTECHNICA SLOVENICA je objavljanje kakovostnih teoretičnih člankov z novih pomembnih področij geomehanike in geotehnike, ki bodo dolgoročno vplivali na temeljne in praktične vidike teh področij.

ACTA GEOTECHNICA SLOVENICA objavlja članke s področij: mehanika zemljin in kamnin, inženirska geologija, okoljska geotehnika, geosintetika, geotehnične konstrukcije, numerične in analitične metode, računalniško modeliranje, optimizacija geotehničnih konstrukcij, terenske in laboratorijske preiskave.

Revija redno izhaja dvakrat letno.

AVTORSKE PRAVICE

Ko uredništvo prejme članek v objavo, prosi avtorja(je), da prenese(jo) avtorske pravice za članek na izdajatelja, da bi zagotovili kar se da obsežno razširjanje informacij. Naša revija in posamezni prispevki so zaščiteni z avtorskimi pravicami izdajatelja in zanje veljajo naslednji pogoji:

Fotokopiranje

V skladu z našimi zakoni o zaščiti avtorskih pravic je dovoljeno narediti eno kopijo posameznega članka za osebno uporabo. Za naslednje fotokopije, vključno z večkratnim fotokopiranjem, sistematičnim fotokopiranjem, kopiranjem za reklamne ali predstavitvene namene, nadaljnjo prodajo in vsemi oblikami nedobičkonosne uporabe je treba pridobiti dovoljenje izdajatelja in plačati določen znesek.

Naročniki revije smejo kopirati kazalo z vsebino revije ali pripraviti seznam člankov z izvlečki za rabo v svojih ustanovah.

Elektronsko shranjevanje

Za elektronsko shranjevanje vsakršnega gradiva iz revije, vključno z vsemi članki ali deli članka, je potrebno dovoljenje izdajatelja.

ODGOVORNOST

Revija ne prevzame nobene odgovornosti za poškodbe in/ali škodo na osebah in na lastnini na podlagi odgovornosti za izdelke, zaradi malomarnosti ali drugače, ali zaradi uporabe kakršnekoli metode, izdelka, navodil ali zamisli, ki so opisani v njej.

AIMS AND SCOPE

ACTA GEOTECHNICA SLOVENICA aims to play an important role in publishing high-quality, theoretical papers from important and emerging areas that will have a lasting impact on fundamental and practical aspects of geomechanics and geotechnical engineering.

ACTA GEOTECHNICA SLOVENICA publishes papers from the following areas: soil and rock mechanics, engineering geology, environmental geotechnics, geosynthetic, geotechnical structures, numerical and analytical methods, computer modelling, optimization of geotechnical structures, field and laboratory testing.

The journal is published twice a year.

COPYRIGHT

Upon acceptance of an article by the Editorial Board, the author(s) will be asked to transfer copyright for the article to the publisher. This transfer will ensure the widest possible dissemination of information. This review and the individual contributions contained in it are protected by publisher's copyright, and the following terms and conditions apply to their use:

Photocopying

Single photocopies of single articles may be made for personal use, as allowed by national copyright laws. Permission of the publisher and payment of a fee are required for all other photocopying, including multiple or systematic copying, copying for advertising or promotional purposes, resale, and all forms of document delivery.

Subscribers may reproduce tables of contents or prepare lists of papers, including abstracts for internal circulation, within their institutions.

Electronic storage

Permission of the publisher is required to store electronically any material contained in this review, including any paper or part of the paper.

RESPONSIBILITY

No responsibility is assumed by the publisher for any injury and/or damage to persons or property as a matter of product liability, negligence or otherwise, or from any use or operation of any methods, products, instructions or ideas contained in the material herein.